DOMINANT SINGULARITY AND FINITE ELEMENT ANALYSES OF PLANE-STRAIN STRESS FIELDS IN CREEPING ALLOYS WITH SLIDING GRAIN BOUNARIES

by

CHUN WOON LAU

S.B. Massachusetts Institute of Technology
(1972)

S.M. Massachusetts Institute of Technology
(1974)

SUBMITTED IN PARTIAL FULFILLMENT
OF THE REQUIREMENTS FOR THE
DEGREE OF
DOCTOR OF PHILOSOPHY

at the

MASSACHUSETTS INSTITUTE OF TECHNOLOGY

October 2, 1981
(i.e. Feb. '82)

Signature of Author _____
Department of Mechanical Engineering
October 2, 1981

Certified by _____
Ali S. Argon
Thesis Supervisor

Accepted by _____
Warren M. Rohsenow
Chairman, Departmental Graduate Committee

DOMINANT SINGULARITY AND FINITE ELEMENT ANALYSES OF PLANE-STRAIN STRESS FIELDS IN CREEPING ALLOYS WITH SLIDING GRAIN BOUNDARIES

by

CHUN WOON LAU

Submitted to the Department of Mechanical Engineering on October 2, 1981 in partial fulfillment of the requirements for the Degree of Doctor of Philosophy in Mechanical Engineering

ABSTRACT

The most dominant singular stress distributions, caused by grain boundary sliding accommodated by power-law creep, have been determined locally at hard grain boundary particles and at triple grain junctions where cavitations and eventual creep cracking are frequently observed. Finite element computations with specially developed features have been used to connect these local stresses to the far field stresses. These finite element analyses incorporate a specially formulated power-type singularity element, a new method of simulating periodicity and symmetry boundary conditions, a scheme for automatic variable step selection for stable time integration and a method to bypass the influence of incompressibility. The finite element results show very good agreement with results of the local field analyes, and provide accurate estimations of the generalized stress intensity factors.

Thesis Supervisor: Dr. Ali S. Argon
Title: Professor of Mechanical Engineering

ACKNOWLEDGEMENTS

I wish to express my deepest gratitude to my thesis advisor, Professor Ali S. Argon, for introducing me to the challenge of this research topic, for his guidance, and for his continuous generous encouragement. My apprenticeship with him has resulted in many valuable educational experiences of growth which I treasure.

During the course of this research, several advisors and friends have also offered useful discussions and help that contribute to crystallize my approach. They are Professors F. A. McClintock, J. L. Bassani, K. J. Bathe, M. P. Cleary, D. M. Parks, I. W. Chen, C. F. Shih and J. W. Hutchinson, and Dr. M. D. Snyder. To them, I am grateful.

My brother Alfred Y. C. Lau has volunteered to draw the illustrations of this thesis. I am thankful for his quick and timely assistance.

I appreciate the kindness of those of my friends who help me in various ways to produce the physical copy of this thesis.

This research has been funded in part by the Army Research Office under contract no. DAAG29-74-C-0008 and in part by the United States Department of Energy under contract no. DE-AC02-77ER04461. These supports are gratefully acknowledged.

TABLE OF CONTENTS

TABLE OF CONTENTS (CONTINUED)

LIST OF FIGURES

LIST OF FIGURES (CONTINUED)

LIST OF FIGURES (CONTINUED)

LIST OF FIGURES (CONTINUED)

LIST OF FIGURES (CONTINUED)

LIST OF TABLES

CHAPTER ONE

INTRODUCTION

At elevated temperatures*, deformation mechanisms such as grain boundary sliding, diffusion, and dislocation creep, which are usually inactive at low temperatures, can contribute significantly to the flow of structural alloys (McClintock and Argon 1966). These additional deformation mechanisms can give rise to fracture processes that are different from those of the more frequently studied and better understood low temperature brittle and ductile fractures (Argon and Im 1975; Knott 1973; McClintock 1971). Fracture processes in crystalline alloys under service loading at elevated temperature usually involve the nucleation of intergranular cavities, their growth and linking to form macro-cracks, and the eventual propagation of these macro-cracks to final fracture. Experiments have shown that creep cavities form on particles and at triple grain junctions on sliding grain boundaries (Chen and Argon 1981; Perry 1974 ; Grant 1971). It is now clear that such cavities are nucleated by locally accentuated stresses caused by grain boundary sliding accommodated principally by power-law creep within the grains and by diffusional flow over shorter ranges (Argon, Chen and

*Above 0.4 T_m, where T_m is the melting point of the alloy in degrees Kelvin.

Lau 1981, 1980; Lau and Argon 1977). Although many creep fracture mechanisms have been proposed and reviewed (Morris 1978; Raj 1978; Perry 1974; Grant 1971; Heald and Williams 1970), quantitative description of concentrated stress fields which are essential for rigorous mechanistic analysis of intergranular creep crack nucleation have been scarce.

In this thesis, we present computational methods for determining in detail these singular stress distributions. More specifically, the dominant stress singularity together with the generalized creep stress intensity factor will be solved for (A) the apexes of hard particles embedded in sliding grain boundaries and (B) the triple grain junction, in a creeping continuum where boundaries have little resistance to sheer deformation -- conditions widely encountered in structural alloys under usual operating conditions above 0.4 T_m (Fig. 1.1). The results of this study make it possible to estimate, in a mechanically consistent manner, the rate of cavity nucleation in a creeping alloy (Argon, Chen and Lau, 1980, 1981).

The stress analysis of each of these two problems is in three parts. In part one, the dominant singular nature of the stresses together with their angular distribution are determined for a linearly creeping alloy by solving the appropriate local boundary value problems using

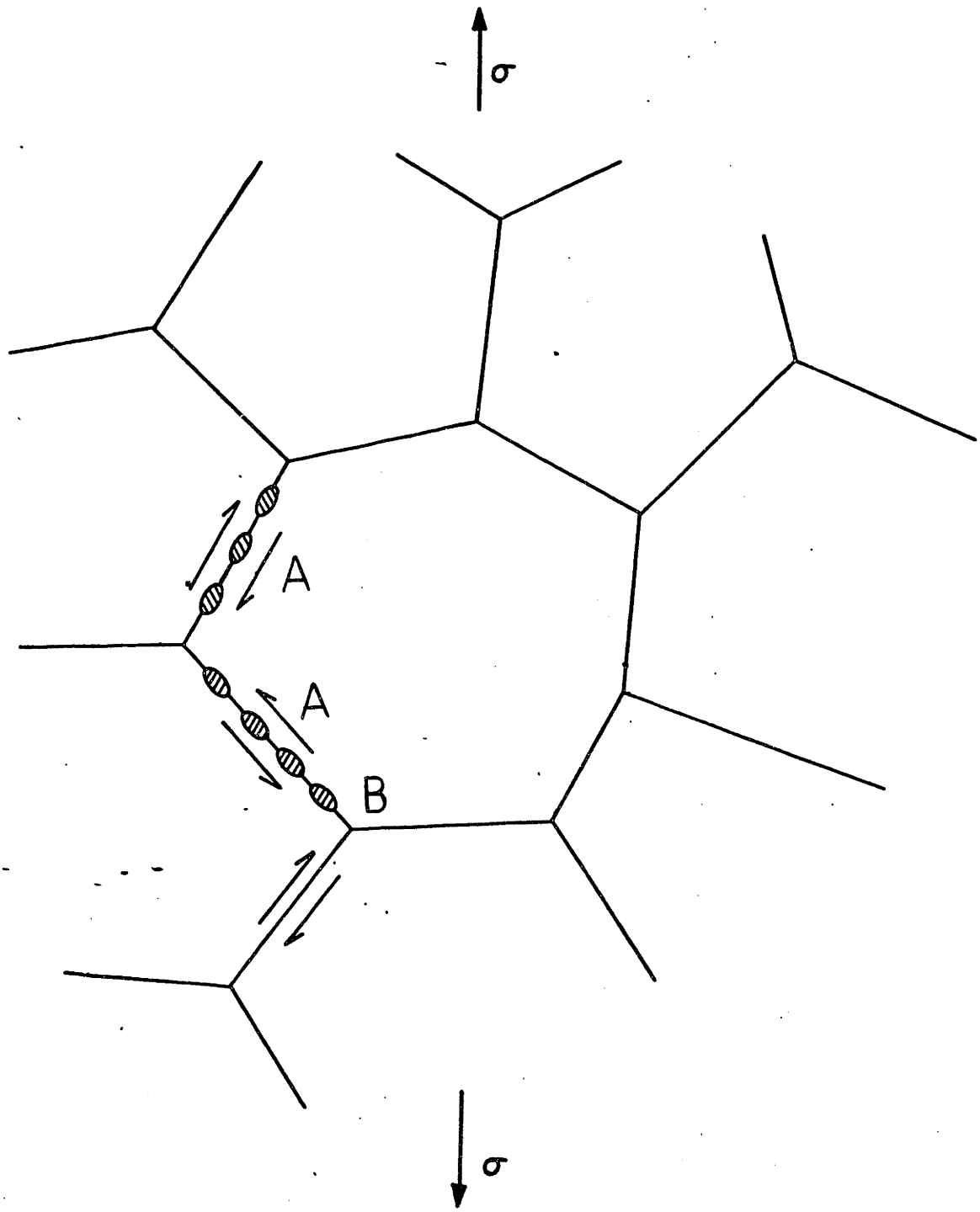

Figure 1.1 Two Boundary Value Problems Important in Intergranular Cavitation: A. Stress Concentrations Around Grain-Boundary Particles; B. Stress Concentrations at Triple Grain Junctions.

methods from isotropic, incompressible, plane strain elasticity. In part two, these linear solutions are extended to the power-law creep regime by numerically solving the governing fourth order nonlinear differential equations for these boundary value problems using the shooting method (Roberts and Shipman 1972; Keller 1968) and the parameter tracking technique (Shih 1973, 1974) to obtain local dominant singular fields analogous to the well known HRR fields of stationery cracks (Hutchinson 1968; Rice and Rosengren 1968). In part three, a special finite element program is developed, and coded into a version of ADINA (Bathe 1976) to solve for the global stress distribution to provide a connection between the far field stresses and the local singular stresses. This finite element computation incorporates specially formulated power-type singularity elements, a novel method of kinematically simulating boundary conditions due to periodicity and symmetry, and a scheme for automatic variable time step selection for stable explicit time integration.

These three parts of the stress analysis for both the hard particle and the triple grain junction problems, are presented in Chapters 2, 3 and 4, respectively. The principal features of these results which are germane to the understanding of experimental observations will be

summarized and discussed in Chapter 5. The relevance of these results to creep cavity nucleation will be pointed out, and applications of these methods to other problems of interest in nonlinear fracture mechanics will also be discussed.

CHAPTER TWO

DOMINANT STRESS SINGULARITY IN LINEAR CREEPING ALLOY

2.1 Introduction

The goal of this thesis is to determine the most dominant singular stress distribution at both (A) the apex of a hard inclusion embedded in a sliding grain boundary and (B) the triple point grain junction, in an alloy creeping above $0.4\ T_m$ where T_m is its melting point in degrees Kelvin.

At such elevated temperatures and under very high strain rates and stresses ($>10^{-2}\ \mu$, where μ is the shear modulus), the grain boundaries cast negligible influence on the deformation and stress distribution in the grains (Crossman and Ashby 1975; Chen and Argon 1979; Ghahremani 1980). On the other hand, under moderate stresses ($10^{-4}\ \mu$ - $10^{-3}\ \mu$), such as in most elevated temperature engineering service conditions, grain boundaries are much less resistant to shear flow than the material in the grains. These soft grain boundaries and interface boundaries tend to slide to relieve any shear stress acting across them. At elevated temperatures, the bulk of the geometric incompatibility resulting from such sliding is ultimately accommodated by creep and diffusional flows in the grains, producing stress

concentrations at locations having sharp intensified velocity gradient. The intensity of these stress singularities varies directly with the ease of the boundaries to slide.

In this chapter we determine the most severe stress singularity, which corresponds to free sliding boundaries that can support no shear stress. There is a discontinuity in tangential velocity across the sliding boundaries, but normal stress and normal velocity are continous across boundaries. At elevated temperatures, this condition is achieved after only very short periods of time (Argon, Chen and Lau 1980, 1981).

Only plane strain, which is the more critical mode in planar fracture mechanics, is considered. The accommodating flow in the grains is modelled by a linear creep law. The equations of this linear creep law, equilibrium, strain-displacement, and compatibility are obtained from incompressible plane strain Hookean elasticity by replacing displacements and strains with their respective time rates. Hence equilibrium is satisfied by a biharmonic stress function Φ,

$$\nabla^4 \Phi = 0 \tag{2.1}$$

where Φ must satisfy the stress and velocity boundary conditions. The stresses are then defined in terms of Φ

by (Coker and Filon 1931):

$$\sigma_r = \frac{1}{r^2}\frac{\partial^2 \Phi}{\partial \theta^2} + \frac{1}{r}\frac{\partial \Phi}{\partial r} \tag{2.2a}$$

$$\sigma_\theta = \frac{\partial^2 \Phi}{\partial r^2} \tag{2.2b}$$

$$\sigma_{r\theta} = -\frac{1}{r}\frac{\partial^2 \Phi}{\partial r \partial \theta} + \frac{1}{r^2}\frac{\partial \Phi}{\partial \theta} \tag{2.2c}$$

A harmonic function ψ is related to Φ by

$$\nabla^2 \Phi = \frac{\partial}{\partial r}\left(r \frac{\partial \psi}{\partial \theta}\right) \tag{2.3a}$$

so that the r and θ velocities are defined as

$$\dot{u}_r = \frac{1}{2\eta}\left[-\frac{\partial \Phi}{\partial r} + 0.5\, r \frac{\partial \psi}{\partial \theta}\right] \tag{2.3b}$$

$$\dot{u}_\theta = \frac{1}{2\eta}\left[-\frac{1}{r}\frac{\partial \Phi}{\partial \theta} + 0.5\, r^2 \frac{\partial \psi}{\partial r}\right] \tag{2.3c}$$

where η is the creep viscosity which replaces the shear modulus of Hook's law.

The boundary conditions of both the hard particle problem and triple grain junction problem (Sections 2.2 and 2.3) allow the asymptotic expansion of Φ about the singular point to take a separable, power series form in terms of r and θ, which are the coordinates of the

cylindrical system centered at the singular point. We shall consider only its dominant term which gives the most intensified local stress and strain rate fields as $r \to 0$:

$$\Phi(r,\theta) = K r^{\lambda+2} \hat{\phi}(\theta) \tag{2.4}$$

where K and λ are constants and $\hat{\phi}$ is a nondimensional function of θ, all yet to be determined .

Hence the stresses are separable into r and θ dependent parts:

$$\sigma_r = K r^{\lambda} \hat{\sigma}_r = K r^{\lambda} [\hat{\phi}'' + (\lambda+2)\hat{\phi}] \tag{2.5a}$$

$$\sigma_\theta = K r^{\lambda} \hat{\sigma}_\theta = K r^{\lambda} [(\lambda+1)(\lambda+2)\hat{\phi}] \tag{2.5b}$$

$$\sigma_{r\theta} = K r^{\lambda} \hat{\sigma}_{r\theta} = K r^{\lambda} [-(\lambda+1)\hat{\phi}'] \tag{2.5c}$$

The effective stress σ_e, the out of plane stress σ_z, and the hydrostatic stress σ_{kk} are given by

$$\sigma_e = K r^{\lambda} \hat{\sigma}_e = K r^{\lambda} [\tfrac{3}{4}(\hat{\sigma}_r - \hat{\sigma}_\theta)^2 - 3\hat{\sigma}_{r\theta}^2]^{\frac{1}{2}} \tag{2.6}$$

$$\sigma_z = K r^{\lambda} \hat{\sigma}_z = K r^{\lambda} [\tfrac{1}{2}(\hat{\sigma}_r + \hat{\sigma}_\theta)] \tag{2.7}$$

$$\sigma_{kk} = K r^{\lambda} \hat{\sigma}_{kk} = K r^{\lambda} [\tfrac{1}{2}(\hat{\sigma}_r + \hat{\sigma}_\theta)] = \sigma_z \tag{2.8}$$

Thus, the deviatoric stresses, S_{ij}, are also separable into r and θ dependent parts:

$$\begin{aligned} S_{ij} &= \sigma_{ij} - \frac{1}{3}\sigma_{kk}\delta_{ij} \\ &= K r^{\lambda} \hat{S}_{ij} \\ &= K r^{\lambda}\left[\hat{\sigma}_{ij} - \frac{1}{3}\hat{\sigma}_{kk}\delta_{ij}\right] \end{aligned} \tag{2.9}$$

2.2 The Hard Particle

Figure 2.1 shows the geometry, co-ordinate system and appropriate boundary conditions at the apex of a rigid particle of half angle ω pinning a sliding grain boundary under a far field shear stress.

Let $\hat{\phi}$ and $\hat{\psi}$ have the form (Williams 1952, 1957):

$$\begin{aligned} \hat{\phi} = a_1 \sin(\lambda+2)\theta &+ a_2 \cos(\lambda+2)\theta \\ &+ a_3 \sin\lambda\theta + a_4 \cos\lambda\theta \end{aligned} \tag{2.10}$$

$$\hat{\psi} = \frac{4}{\lambda}\left[-a_3 \cos\lambda\theta + a_4 \sin\lambda\theta\right] \tag{2.11}$$

The boundary conditions of Fig. 2.1 require a_1, a_2, a_3, a_4, to satisfy four homogeneous equations. For a non-trivial solution, the determinant of the coefficients of these four equations must vanish. Thus λ is governed by

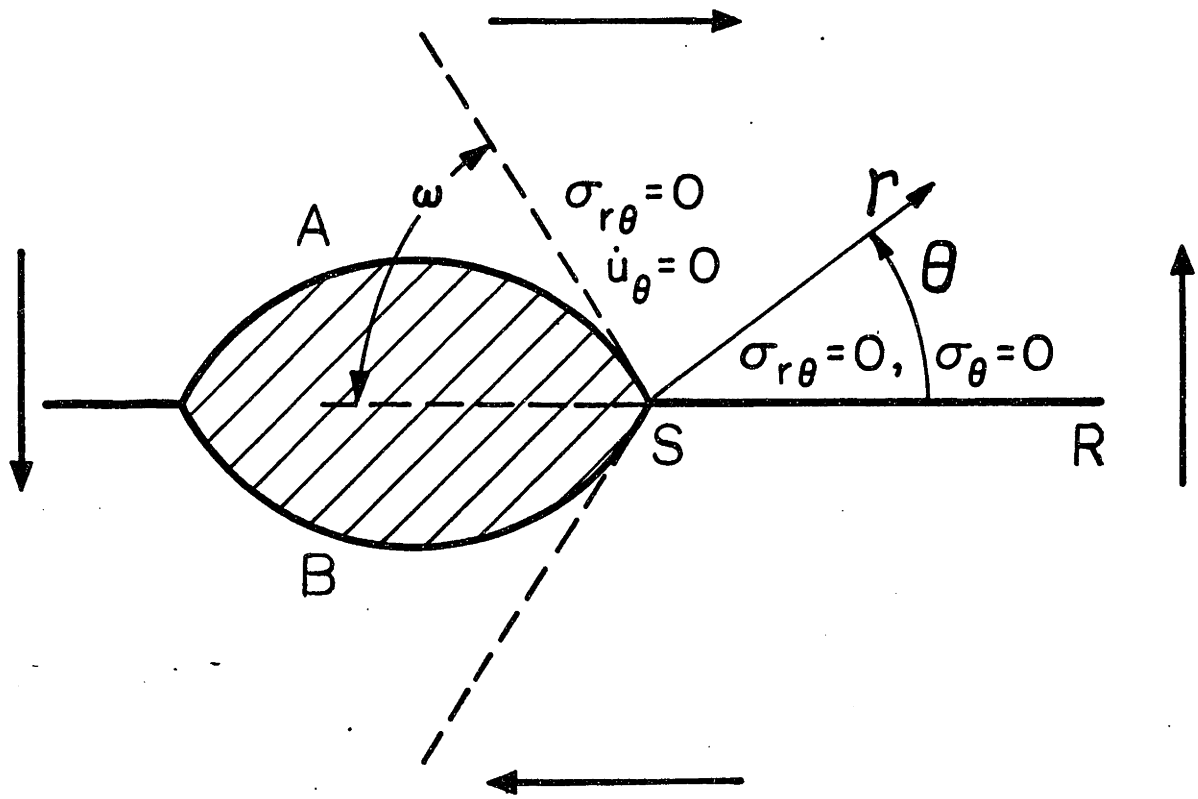

Figure 2.1 Boundary Conditions at the Apex of Hard Particle of Half Angle ω Embedded in a Sliding Grain Boundary Subject to Far Field Shearing.

the eigenvalue equation (in terms of $\gamma \equiv \pi-\omega$):

$$\lambda \sin \lambda\gamma \cos(\lambda+2)\gamma - (\lambda+2)\sin(\lambda+2)\gamma \cos \lambda\gamma = 0 \quad (2.12)$$

The transcendental equation yields multiple roots for λ, not all of which are of interest. If by physical arguments a stress singularity is expected, values of λ less than zero are of interest. However, λ must always be larger than -1 so that the strain rates within a finite region about the apex is finite. Hence, the dominant singularity is given by the solution to the eigen-equation in the range of $-1<\lambda<0$.

The solution of λ for rigid particles of half angle ω varying from 0 to $\pi/2$ is shown by the solid line in Fig. 2.2. This line demonstrates that stresses are nonsingular for $\omega = \pi/2$, singular for acute ω, and becomes more singular as the apex half angle ω decreases. This is physically reasonable. At the limit when ω is so large that the particle-grain interface is perpendicular to the horizontal sliding grain boundary and the loading axis, not only do the particle-grain interface boundaries not slide, but they also prevent any relative motion perpendicular to them ($U_n=0$). Hence, the vertical interface boundaries of the rigid particle disallow the horizontal grain boundary to cause any shearing motion at the apex.

The horizontal grain boundary serves no purpose in this case and the stresses are nonsingular. When ω is acute, the component of the driving shear stress acting across the particle-grain interface is nonzero. The interfaces AS and BS (Fig. 2.1) slide in opposite directions. Near the apex S, material is pressing against the particle in the lower grain and tearing away from the particle in the upper grain. Hence, S is an anchor point in the continuum where the tensile normal strain rate of the upper interface boundary, AS, and the compressive normal strain rate of the lower interface boundary, BS, abruptly switches sign; thus generating the strain rate (and stress) singularity at S. For a more acute particle, AS and BS are more in alignment with the direction of the far field shear loading. The slidings are then more severe, so the singularity at the pinning point, S, is more severe. The solid line in Fig. 2.2 shows that this singularity tends to $1/\sqrt{r}$ as ω tends to zero. This reasoning is valid for any real particle ($\omega>0$) which can physically obstruct the sliding of the upper and lower grains. However, for the fictitious case of an imaginary particle of $\omega = 0$, the interface boundaries AS and BS are collinear with the grain boundary SR. This composite horizontal boundary ABSR then slides freely as a whole, without any physical obstruction at S. Hence, physically no singularity

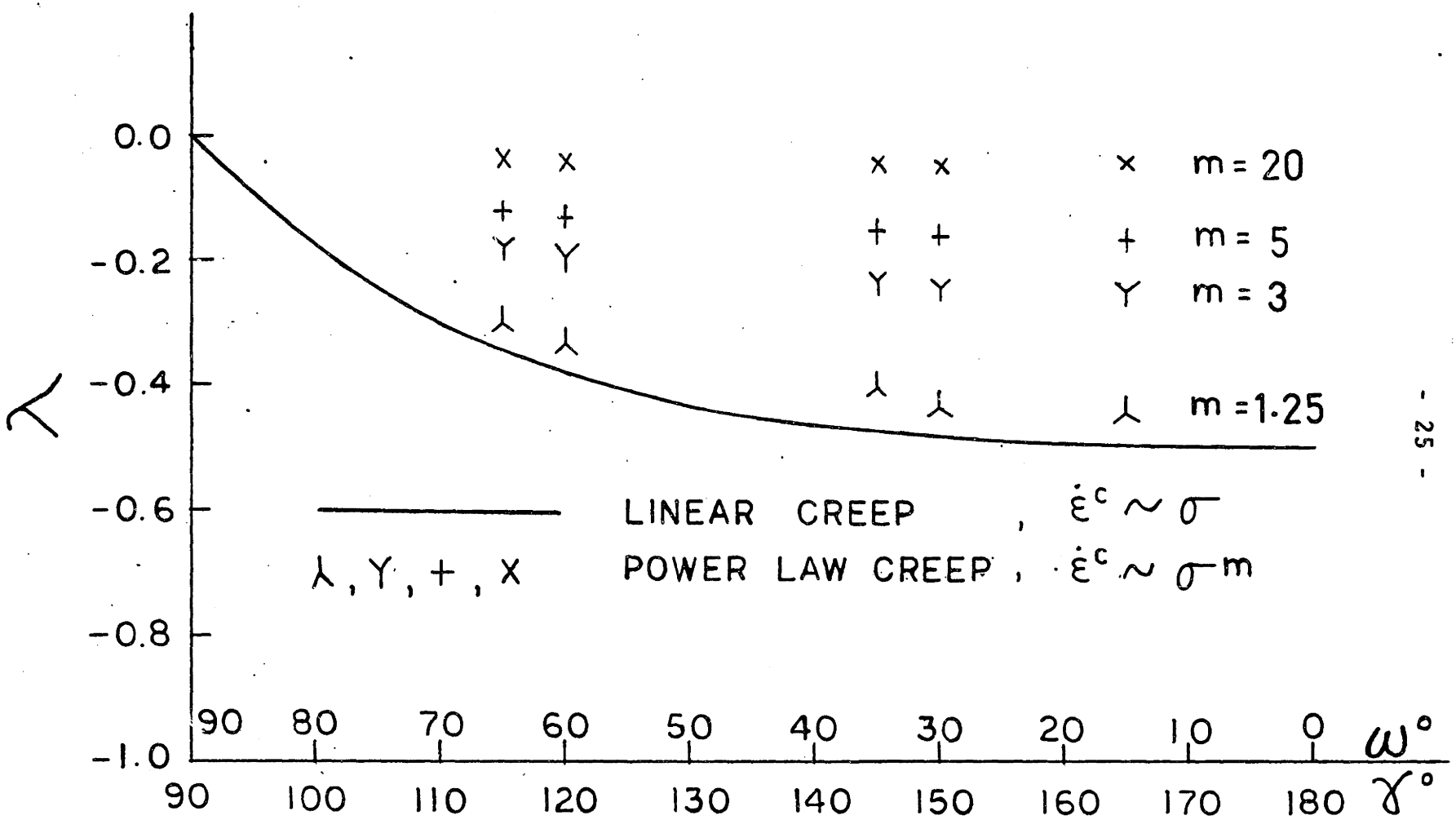

Figure 2.2 Variation of λ with ω (and γ) for various m.

is expected at S. The trivial stresses at S then correspond to a solution of selecting the root λ from a range other than $-1<\lambda<0$ (which presumes a singularity at S). In this case, the overall equilibrium of the upper and lower grains must then be maintained by obstacles elsewhere on the grain boundary, such as at triple points or at other realistic particles with $\omega>0$.

To compute the angular distribution of the stresses, we determine the $a_i (i=1,2,3,4)$ corresponding to the eigenvalue λ from the four boundary conditions. These conditions yield equations homogeneous in a_i, so that if a_i is a solution, any arbitrary constant times a_i is also a solution. This means that the stresses, strain rates and velocities are all determined to an arbitrary multiplicative constant. The circumferential component of the stresses $\hat{\sigma}_{ij}$ are normalized with the maximum circumferential equivalent stress, $\hat{\sigma}_e$. This normalization defines K (Eq. 2.5) uniquely.

The angular distribution of stresses, $\hat{\sigma}_{ij}$ reveals that, for every apex half-angle ω, the maximum opening stress $\hat{\sigma}_\theta$ is always at the particle-grain interface. A typical angular stress distribution ($\hat{\sigma}_{ij}$ versus θ) for a hard particle of $\omega=\pi/4$ is shown in Fig. 2.3. It shows additionally that $\hat{\sigma}_e$ attains its maximum value

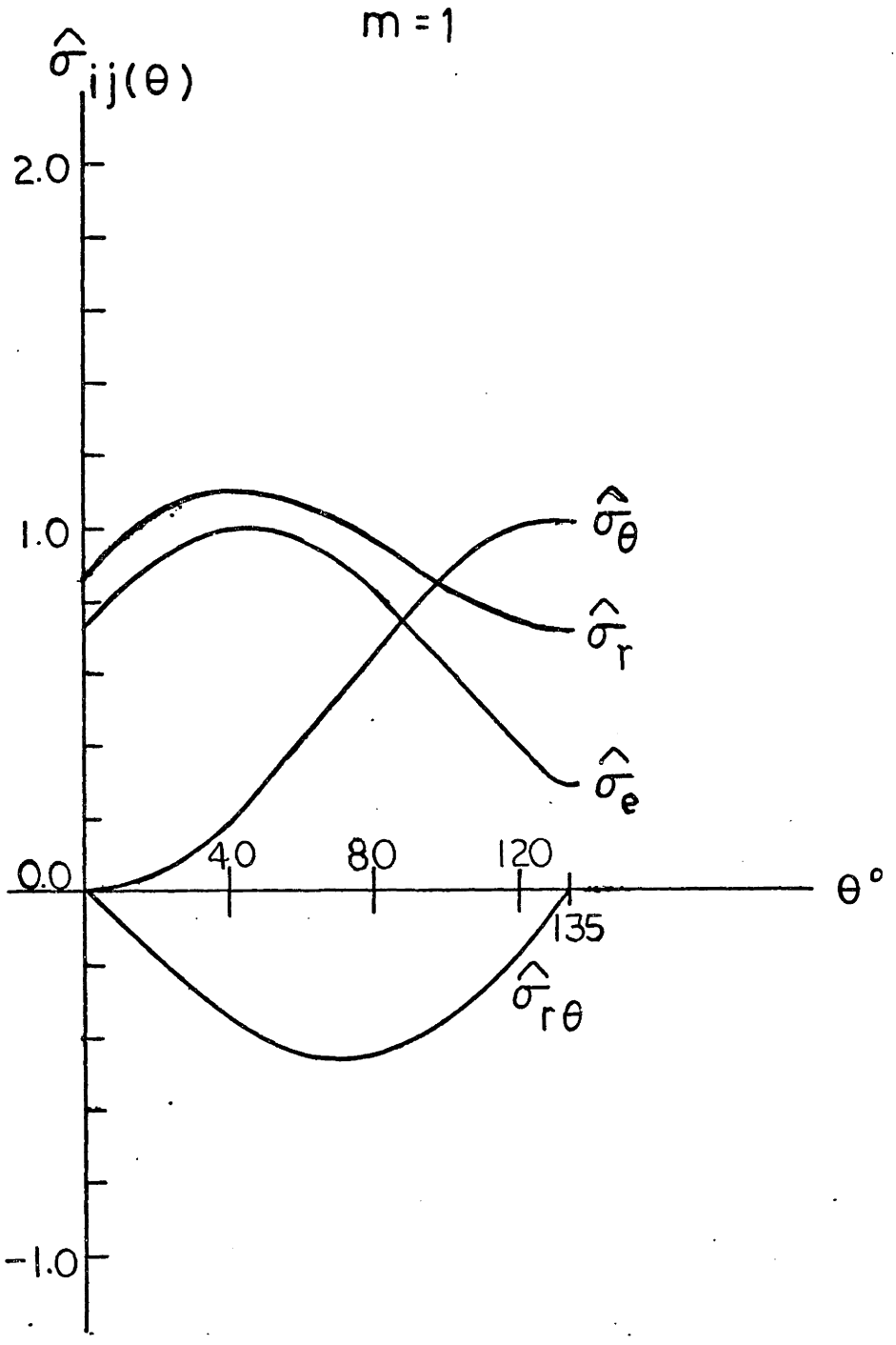

Figure 2.3 Variation of $\hat{\sigma}_{ij}$ with θ at the Apex of a Hard Particle in Linear Creep, $\omega = \pi/4$.

at the extension of the sliding particle-grain interface as might be expected.

2.3 The Triple Grain Junction

Fig. 2.4 shows the boundary conditions at a triple grain junction of regular hexagonal grains under a far field tensile loading. Two Airy stress functions, Φ_I in grain I and Φ_{II} in grain II are used. The boundary conditions restrict that K and λ of Φ_I and Φ_{II} must be identical. However, $\hat{\phi}_I$ (of Φ_I) must differ from $\hat{\phi}_{II}$ so as to model the discontinuity in $\hat{\sigma}_r$ and $\hat{u}_r$ across the slanted sliding grain boundary. Let $\hat{\phi}_I$ and $\hat{\phi}_{II}$ be of the following forms which are symmetric about $\theta = 0$:

$$\hat{\phi}_I = b_1 \cos(\lambda+2)\theta + b_2 \cos\lambda\theta \qquad (2.13a)$$

$$\hat{\phi}_{II} = b_3 \cos(\lambda+2)\varphi + b_4 \cos\lambda\varphi \qquad (2.13b)$$

where φ is measured from the dotted line of Fig. 2.4 in anticlockwise direction and the velocities, strain rates and stresses of grain II are consistently defined. The boundary conditions of Fig. 2.4 give four homogeneous equations governing b_i which have nontrivial solutions only if the determinant of the coefficients vanishes. Hence, λ obeys the characteristic equation,

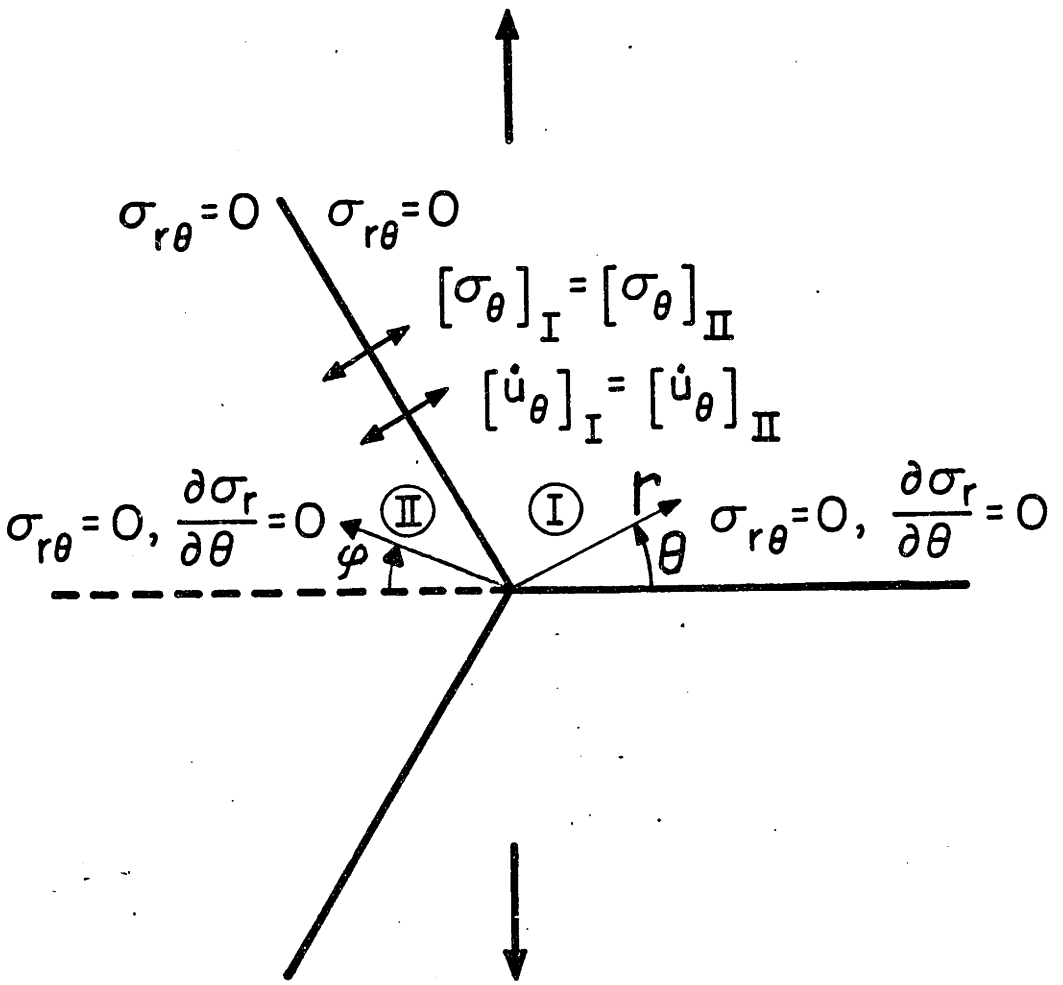

Figure 2.4 Boundary Conditions at Triple Grain Junction Subject to Far Field Tensile Loading.

$$\sqrt{3}(\lambda+1)\tan\frac{(\lambda+1)\pi}{3} + 8\sin^2\frac{(\lambda+1)\pi}{3} - 3 = 0 \qquad (2.14)$$

The only root of this equation within $-1<\lambda<0$ is $\lambda=-0.449$ which gives the angular stress distribution shown in Fig. 2.5. The opening stress, $\hat{\sigma}_\theta$, is compressive at the slanting grain boundary and is tensile and maximum at the horizontal grain boundary. Indeed, creep fracture literature gives many examples of observations of cracks forming predominantly on the grain boundaries which are perpendicular to the distant tensile stress (Grant 1971; Perry 1974; Chen and Argon 1981).

2.4 Discussion

The solution for the stress singularity at a hard particle, due to grain boundary sliding accommodated by linear creep indicates the radial dependence of stresses varies from no singularity for $\omega=\pi/2$ to $\sim 1/\sqrt{r}$ singularity for ω close to 0. The corresponding angular variation of the stresses points out that the the sliding of the interface boundary is always propagated into the adjoining opposite grain in the form of maxima in localized shear stress and strain. The opening stress σ_θ is always maximum and tensile across one of the sliding interface boundaries (and compressive across the other).

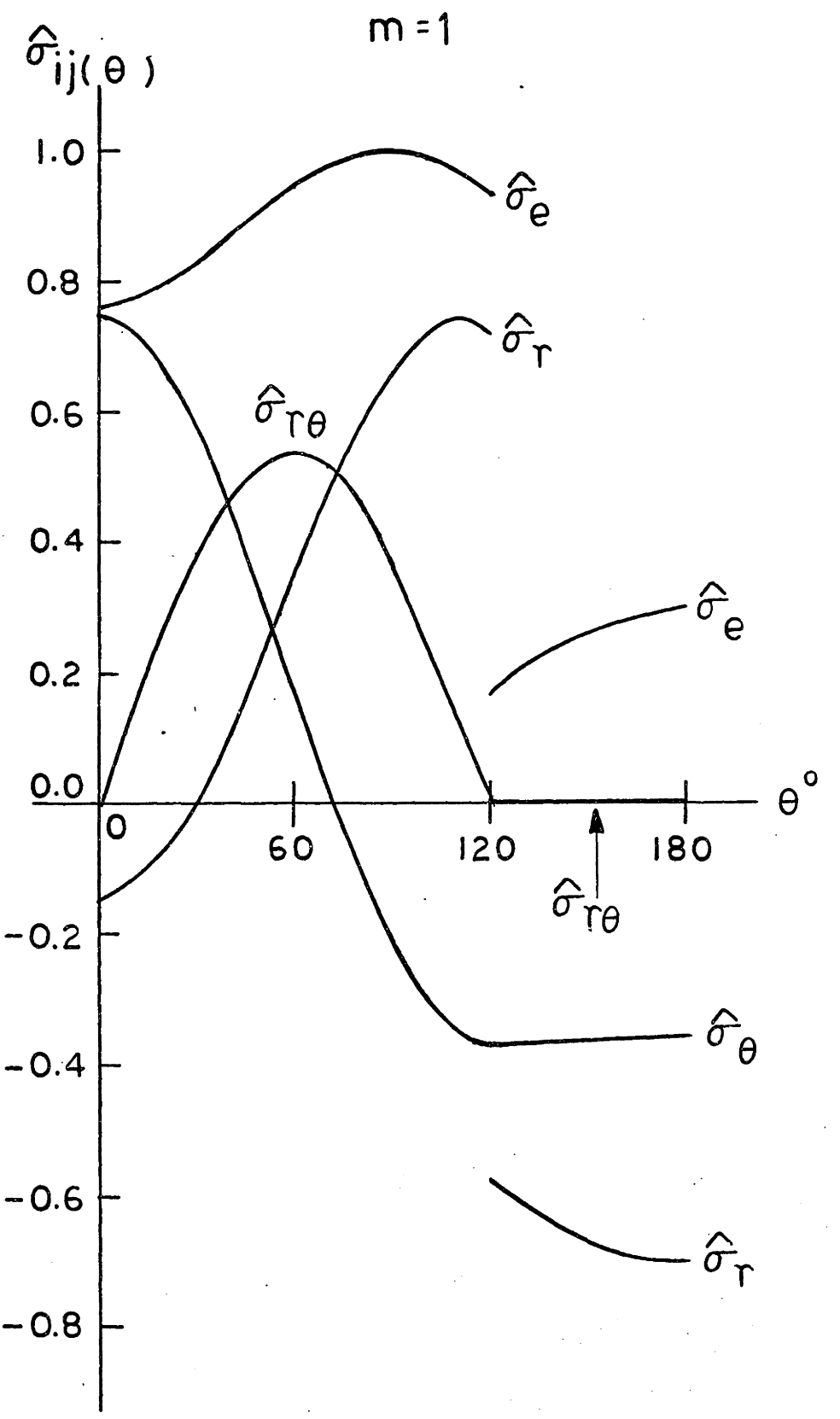

Figure 2.5 Variation of $\hat{\sigma}_{ij}$ with θ at Triple Grain Junction in Linear Creep.

For the triple grain junction, there is always a stress singularity of $r^{-0.449}$ for stable regular hexagonal grains. The sliding is propagated into the adjoining and opposite grain as locally accentuated shear stress and strain. The opening stress σ_θ is maximum and tensile across the horizontal nonsliding grain boundary, but compressive across the slanting, sliding grain boundaries. These distributions of stresses correlate with the microscopic observations of creep fracture.

The stress singularity exponent, λ, determined in this chapter is the most severe one that can exist for the same creep law and the same geometry. In cases where grain boundaries transmit some shear traction while sliding, the stress singularity would be milder. This can occur at lower temperature, at much higher strain rates and stresses where boundaries can be expected to transmit a proportionally larger fraction of the shear traction applied across them. At the limit when boundaries are too viscous to produce any significant sliding, the stress singularity will vanish. However, the most severe singularity, corresponding to free sliding, is the limiting condition which is of interest in micromechanical modelling of creep fracture processes where the worst possibility is considered.

The linear creep solutions in this chapter can serve as a launching point in the numerical solution using the parameter tracking scheme to determine stress singularities due to sliding interfaces in power-law creep under monotonic loading. Also, they serve as limits to check the non-linear solutions in which the strains are likely to be similar, but more concentrated.

CHAPTER THREE

DOMINANT STRESS SINGULARITY IN POWER-LAW CREEPING ALLOY

3.1 Introduction

At intermediate stresses ($0.5 \times 10^{-4}\mu$ - $0.8\times10^{-3}\mu$) and in the elevated temperature range of 0.4 - 0.6 T_m, conditions under which most high temperature alloys are used, creep flow results from the slide and climb motion of lattice dislocations. In this regime of dislocation creep, the steady state creep rate obeys a power-law stress relationship (Norton 1929; Garofalo 1965; Bird, Mukherjee and Dorn 1969; Ashby 1972; Gittus 1974) of the form

$$\dot{\varepsilon}_s = A\sigma^m \tag{3.1a}$$

where

$$A = c\frac{D_v \mu b}{kT}\frac{1}{\mu^m} \tag{3.1b}$$

where c and m are material constants, D_v is the volume self-diffusion coefficient, μ the shear modulus, b the Burgers' vector, k Boltzmann's constant and T the absolute temperature. Typical values for m are: 3 for class I alloy; and 5 for class II alloys and for pure metals (Sherby and Burke 1967; Takeuchi and Argon 1976).

In this chapter, we determine the stress singularities in such power-law creeping alloys caused by grain boundary sliding.

For completeness, we present results for m up to 10 -- thus covering not only metals and alloys that undergo steady state creep (at $m \sim 5$) but also non-steady state behavior of many engineering alloys which show an effective $m>5$ at the minimum creep rates. Solutions for higher values of m that might be useful to model "near-plastic behavior" can be routinely generated by the methods presented in this thesis.

Grain boundaries and interface boundaries are modelled as free of shear tractions by virtue of free sliding. The constitutive relationship within the grain is the generalized power-law creep, implied by Eq. 3.1a, for an isotropic incompressible continuum,

$$\dot{\varepsilon}^c_{ij} = \frac{3}{2} A \sigma_e^{m-1} S_{ij} \tag{3.2a}$$

where

$$S_{ij} = \sigma_{ij} - \frac{1}{3} \sigma_{kk} \delta_{ij} \tag{3.2b}$$

and

$$\sigma_e = \left[\frac{3}{2} S_{ij} S_{ij}\right]^{\frac{1}{2}} \tag{3.2c}$$

Equation 3.2a reduces to Eq. 3.1a in simple tension.

We restrict our study to plane strain deformation which is the more critical mode in plane fracture mechanics. The only nonlinearity introduced in this analysis is through the power-law constitutive relationship, Eq. 3.2. Considering only proportional loading in the creep history and by Hoff's (1954) analogy, we can extend the methods of Hutchinson's (1968) pioneering work on stress singularity at a crack tip in power-law hardening plasticity to solve for stress singularities caused by grain boundary sliding accommodated by power-law creep.

The stress quantities are defined by Eqs. 2.2, 2.4, 2.5 and the creep strain rates consistent with Eq. 3.2 are

$$\dot{\varepsilon}_{ij}^{c} = A K^{m} r^{m\lambda} \hat{\varepsilon}_{ij}^{c} \tag{3.3a}$$

where

$$\hat{\varepsilon}_{r}^{c} = \frac{3}{4} \hat{\sigma}_{e}^{m-1} (\hat{\sigma}_{r} - \hat{\sigma}_{\theta}) \tag{3.3b}$$

$$= - \hat{\varepsilon}_{\theta}^{c}$$

$$\hat{\varepsilon}_{r\theta}^{c} = \frac{3}{2} \hat{\sigma}_{e}^{m-1} \hat{\sigma}_{r\theta} \tag{3.3c}$$

and

$$\dot{\varepsilon}_z^c = 0 \tag{3.3d}$$

The velocities resulting from Eqs. 3.3 are

$$\dot{u}_i = A\, K^m\, r^{m\lambda+1}\, \hat{u}_i \qquad (i = r, \theta) \tag{3.4a}$$

where

$$\hat{u}_r = \frac{1}{m\lambda+1}\left[\frac{3}{4}\,\hat{\sigma}_e^{m-1}\,(\hat{\sigma}_r - \hat{\sigma}_\theta)\right] \tag{3.4b}$$

and

$$\hat{u}_\theta = \frac{2-m\lambda}{m\lambda+1}\cdot\frac{3}{4}\cdot\int_0^\theta \hat{\sigma}_e^{m-1}(\hat{\sigma}_r - \hat{\sigma}_\theta)\,d\theta \tag{3.4c}$$

The analog of the biharmonic equation of the previous linear creep analysis (Eq. 2.1) is now a highly nonlinear fourth order partial differential equation

$$\left[\frac{1}{r^2}\frac{\partial^2}{\partial\theta^2} - \frac{1}{r}\frac{\partial}{\partial r} - \frac{1}{r}\frac{\partial^2(r)}{\partial r^2}\right]\cdot\left[\sigma_e^{m-1}\left(\frac{1}{r}\Phi' + \frac{1}{r^2}\Phi^{\cdot\cdot} - \Phi''\right)\right] + 4\,\frac{1}{r^2}\left[r\,\sigma_e^{m-1}\left(\frac{1}{r}\Phi^{\cdot}\right)\right]^{\cdot} = 0 \tag{3.5}$$

where $(\,)' = \partial/\partial r$, $(\,)^{\cdot} = \partial/\partial\theta$ and σ_e is defined in Eq. 3.2. Readers may refer to Hutchinson (1968) for further details. When the dominant term of the asymptotic expansion (Eq. 2.4) is substituted into this equation, a separated form is obtained which reduces this partial differential equation into a parametric eigenvalue ordinary differential

equation of fourth order:

$$\left[\frac{d^2}{d\theta^2} - m\lambda(m\lambda+2)\right]\cdot\left[\hat{\sigma}_e^{m-1}\{\lambda(\lambda+2)\hat{\phi} + \hat{\phi}^{\cdot\cdot}\}\right] + 4(\lambda+1)(m\lambda+1)(\hat{\sigma}_e^{m-1}\hat{\phi}^{\cdot})^{\cdot} = 0 \qquad (3.6)$$

where $\hat{\sigma}_e$ is defined in Eq. 2.5 and $(\ )^{\cdot} = d/d\theta$. We can manipulate Eq. 3.6 into a more explicit but much longer form (see Appendix A).

$$\hat{\phi}^{\cdot\cdot\cdot\cdot} = \hat{\phi}^{\cdot\cdot\cdot\cdot}(\hat{\phi}, \hat{\phi}^{\cdot}, \hat{\phi}^{\cdot\cdot}, \hat{\phi}^{\cdot\cdot\cdot}, \lambda, m) \qquad (3.7)$$

Equation 3.7 can then be solved to conform to particular boundary conditions to furnish the eigenvalue λ and the associated eigenfunctions $\hat{\phi}$, $\hat{\phi}^{\cdot}$, $\hat{\phi}^{\cdot\cdot}$, $\hat{\phi}^{\cdot\cdot\cdot}$. The stresses, strain rates and velocities are then obtained from Eqs. 2.5, 3.3 and 3.4.

Analogous to the eigenvalue equations of Chapter 2, Eq. 3.7 is also homogenous. When $\{\hat{\phi}, \hat{\phi}^{\cdot}, \hat{\phi}^{\cdot\cdot}, \hat{\phi}^{\cdot\cdot\cdot}\}$ are a set of solutions corresponding to a λ, then any scalar multiple of $\{\hat{\phi}, \hat{\phi}^{\cdot}, \hat{\phi}^{\cdot\cdot}, \hat{\phi}^{\cdot\cdot\cdot}\}$ is also a solution. Again, we normalize these eigenfunctions such that $\hat{\sigma}_e$ has a maximum of unity. This imparts a definite value to K of Eq. 2.5.

3.2 The Hard Particle

Figure 3.1 shows the boundary conditions of a hard particle embedded in a sliding grain boundary under a

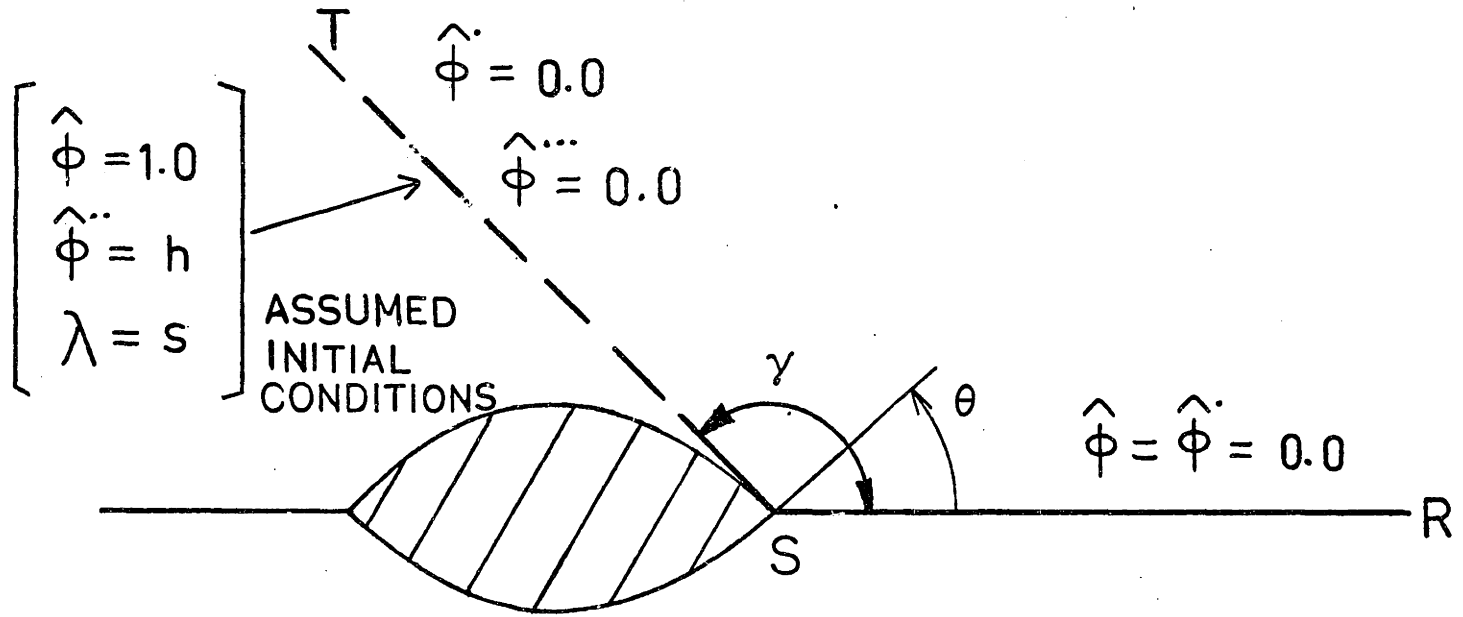

Figure 3.1 Operational Boundary Conditions for a Hard Particle Embedded in a Sliding Grain Boundary Under Far Field Shearing.

constant far field shear stress, in terms of $\hat{\phi}$ and its derivatives. This two point boundary value problem is solved by the shooting method (Keller 1968; Roberts and Shipman 1972). The boundary value problem is treated as if it were an initial value problem, where the missing initial conditions on the starting boundary and the eigenvalue λ take up guessed values. Equation 3.7 is then solved by shooting from the particle-grain interface boundary ST($\theta=\gamma$) to the horizontal grain boundary SR($\theta=0$) where $\hat{\phi}$ and $\hat{\phi}\cdot$ of the computed solution are checked against $\hat{\phi}$ and $\hat{\phi}\cdot$ prescribed there by the boundary condition. If the guessed λ and the guessed missing boundary conditions along the starting line ST happen to be the correct values, the computed $\hat{\phi}$ and $\hat{\phi}\cdot$ along the destination line SR should equal to those prescribed there. This is achieved by systematic trials.

To start, $\hat{\phi}$, $\hat{\phi}^{\cdot}$, $\hat{\phi}^{\cdot\cdot}$ and $\hat{\phi}^{\cdot\cdot\cdot}$ need to be specified along ST together with a value for λ. Of these quantities only $\hat{\phi}^{\cdot}$ and $\hat{\phi}^{\cdot\cdot\cdot}$ are known. Since Eq. 3.7 is homogeneous in $\hat{\phi}$, we can fix $\hat{\phi}(\gamma)=1.0$ and later normalize the solution such that $\hat{\sigma}_e$ has a maximum of 1. We assign to $\hat{\phi}^{\cdot\cdot}(\gamma)$ a parametric value of h and assume λ has a value of s. Any mismatch of the computed versus the prescribed $\hat{\phi}$ and $\hat{\phi}^{\cdot}$ at $\theta=0$ is then due to s and h deviating from their correct values. The correct s and h can then be

systematically attained by the recurrence formula

$$\begin{bmatrix} h \\ s \end{bmatrix}^{i+1} = \begin{bmatrix} h \\ s \end{bmatrix}^{i} - \frac{1}{D}\begin{bmatrix} \frac{\partial M_2}{\partial s} & -\frac{\partial M_1}{\partial s} \\ -\frac{\partial M_2}{\partial h} & \frac{\partial M_1}{\partial h} \end{bmatrix}^{i} \cdot \begin{bmatrix} M_1 \\ M_2 \end{bmatrix}^{i} \tag{3.8}$$

where $D \equiv \frac{\partial M_1^i}{\partial h} \cdot \frac{\partial M_2^i}{\partial s} - \frac{\partial M_1^i}{\partial s} \cdot \frac{\partial M_2^i}{\partial h}$, in which i stands for the ith iteration, and M_1 and M_2 are mismatches defined on the destination boundary SR,

$$M_1(s,h) \equiv \hat{\Phi}(s,h)_{computed} - \hat{\Phi}_{prescribed} \tag{3.9}$$

$$M_2(s,h) \equiv \hat{\Phi}'(s,h)_{computed} - \hat{\Phi}'_{prescribed}$$

The finite difference form of the partial derivatives of M_1 and M_2 are evalued numerically for each iteration i. Had the functional form of M_1 and M_2 been known to allow their partial derivatives to be evaluated exactly, Eq. 3.8 would have been the Newton-Raphson iteration with a fast (quadratic) convergence (Hildebrand 1974).

The radius of convergence for this fast method is smaller than those of most slower (linear) convergent methods such as iterative substitution. Hence, a reasonable initial estimation of the roots of Eq. 3.9 is necessary to ensure convergence. To obtain the solution

for a particular m value, the procedure is started off by selecting $\hat{\phi}''(\gamma)$ and λ from the known solution of linear creep (m=1) from Chapter 2 to be used as initial values of h and s for a m value slightly larger than 1. Once a new solution is obtained, its $\hat{\phi}''(\gamma)$ and λ is in turn used as initial values of h and s for the solution of a yet higher m; thus "tracking" the parameters $\hat{\phi}''(\gamma)$ and λ as a function of m until the solution for the particular m value is obtained.

Since $\hat{\phi}$ and its derivatives are expected to have zones of rapid variation, a numerical scheme capable of easily varying step size is necessary. For this purpose Eq. 3.7 has been converted into a system of four first order ordinary differential equations which were solved using an algorithm based on the Runge-Kutta method (Ralson and Wilf 1960). This algorithm is a stable, self-starting, fourth order integrating procedure capable of automatically adjusting each step size to minimize the local truncation error. An initial step size of 2.5 degrees was used for most computations.

The dependence of the eigenvalue λ (the radial exponent of the stresses) on m for different particle half angle $\omega(\gamma=\pi-\omega)$ is shown in Fig. 3.2. Actual values of λ for integer values of m for these three different

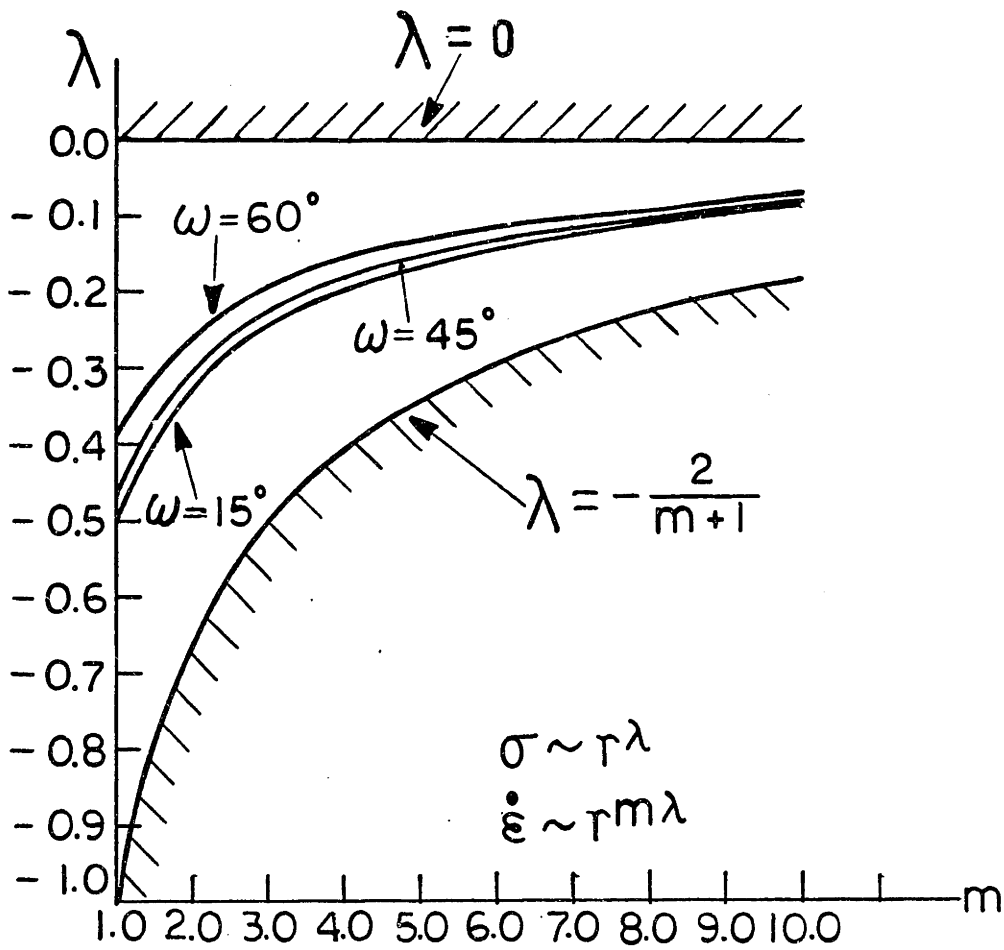

Figure 3.2 Variation of λ with m for various ω.

half angles are given in Table 3.1. A cross plotting of λ versus ω for various m is portrayed in Fig. 2.2. These figures indicate that for the same creep exponent m, particles of smaller half angle ω produce a stronger singularity, i.e., larger stresses near the origin. This dependence on ω is strongest when $m=1$ and becomes less pronounced as m increases. Also, the rate of this dependence $(\Delta\lambda)/(\Delta\omega)$ decreases with ω. All points on the curve for $\omega=15°$ agree with corresponding points for the HRR crack ($\sigma\sim r^{-1/(m+1)}$) to within 1 per cent. This is a generalization to higher m of a conclusion already reached in Chapter 2 that as ω becomes smaller and smaller, the radial dependence of the stresses approaches that of a mode II crack. However, as has been pointed out in Chapter 2, the limiting case of an imaginary particle of $\omega=0$ should be treated differently since in that case, one should select λ from a different range -- one that does not give a singularity.

The eigenvalues for all ω fall within a domain bounded by $\lambda=0$ and $\lambda=-2/(m+1)$. The upper limit corresponds to no stress singularity. The lower limit corresponds to a physically unrealistic unbounded strain energy rate at the origin of the singularity. The trend of λ in Fig. 3.2 indicates that for the same particle (same ω), the stresses tend to be less and less singular

TABLE 3.1

λ FOR INTEGER VALUES OF m FOR VARIOUS ω

m	λ (ω=60°)	λ (ω=45°)	λ (ω=15°)	H_{RR} crack (λ=-1/(m+1))
1	-.384	-.456	-.499	-0.50
2	-.253	-.299	-.331	-0.333
3	-.192	-.225	-.248	-0.250
4	-.156	-.181	-.198	-0.200
5	-.132	-.152	-.165	-0.167
6	-.115	-.131	-.142	-0.143
7	-.101	-.115	-.124	-0.125
8	-.091	-.103	-.110	-0.111
9	-.083	-.093	-.099	-0.100
10	-.076	-.085	-.090	-.091

as m increases. This trend is sensible as at the limit of $m \to \infty$, which corresponds to a rigid-perfectly plastic material, the stresses should indeed be finite and therefore $\hat{\lambda}$ cannot be negative. It needs to be pointed out that as $m \to \infty$, $\hat{\sigma}_{ij}$ as defined in Eq. 2.5 should approach the correct stress solution, but $\dot{\varepsilon}^c_{ij}$ as defined in Eq. 3.3 can at most approach one of the many strain rate solutions. When $m \to \infty$, the strain rates (strains) can have multiple values while stresses are single valued, i.e., the strain rates become non-unique as is well known in the theory of plasticity. The original governing equation (Eq. 3.5) is in fact elliptic when m=1, but ultimately tends to become hyperbolic as m tends to infinity and the behavior reverts to ideal plasticity. Although it is not apparent how the relative strengths of ellipticity and hyperbolicity of this governing equation changes as a function of m, Hutchinson (1968), Rice and Rosengren (1968) and Shih (1974 , 1973) have demonstrated that solutions of the form given in Eq. 2.4 that lead to Eq. 2.5 and Eq. 3.3 are capable of producing correct and physically meaningful results for the entire intermediate ranges of m. Shih (1974, 1973) has obtained good results with m as high as 99.

The angular distribution of total stresses for m=3, 5, 7 and 10 are presented in Figs. 3.3-3.6 for a typical hard particle with half angle $\omega=\pi/4$. Figures 3.7 to 3.10 show the corresponding angular distribution of deviatoric stress $\hat{S}_{ij}$ where

$$S_{ij} = K r^{\lambda} \hat{S}_{ij} = K r^{\lambda} [\hat{\sigma}_{ij} - \frac{1}{3} \hat{\sigma}_{kk} \delta_{ij}] \tag{3.10}$$

and S_{ij} is defined in Eq. 3.2.

Figure 3.11 portrays the angular stress distribution for hard particles of $\omega=65°$ (curves terminating at $\theta=\gamma=115°$) and $\omega=15°$ (curves terminating at $\theta=\gamma=165°$) at m=5. This figure is an extension to Fig. 3.4 in which $\omega=45°$.

From these figures, the following trends about the angular distribution of the stresses become apparent: $\hat{\sigma}_e$ always attains its maximum at $\theta=\gamma/2, (\gamma=\pi-\omega)$, and so is the absolute value of $\hat{\sigma}_{r\theta}$. This orientation in general does not coincide with the extension of a sliding interface boundary. Hence contrary to the case for m=1, the extension of a sliding interface is not necessarily where the maximum shear activity occurs. For m>1, the shear

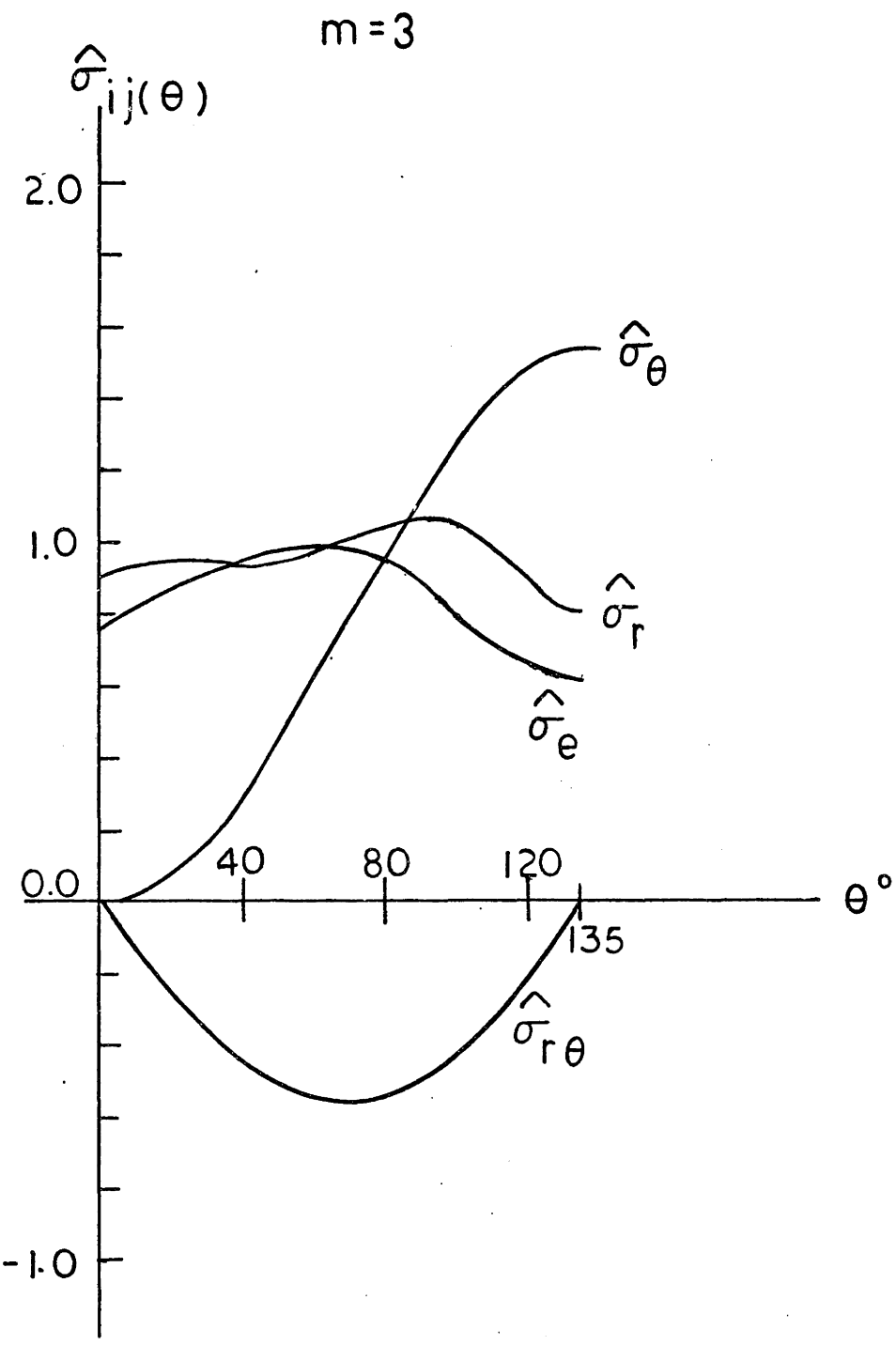

Figure 3.3 Variation of $\hat{\sigma}_{ij}$ with θ at the Apex of a Hard Particle of $\omega = \pi/4$, $m = 3$.

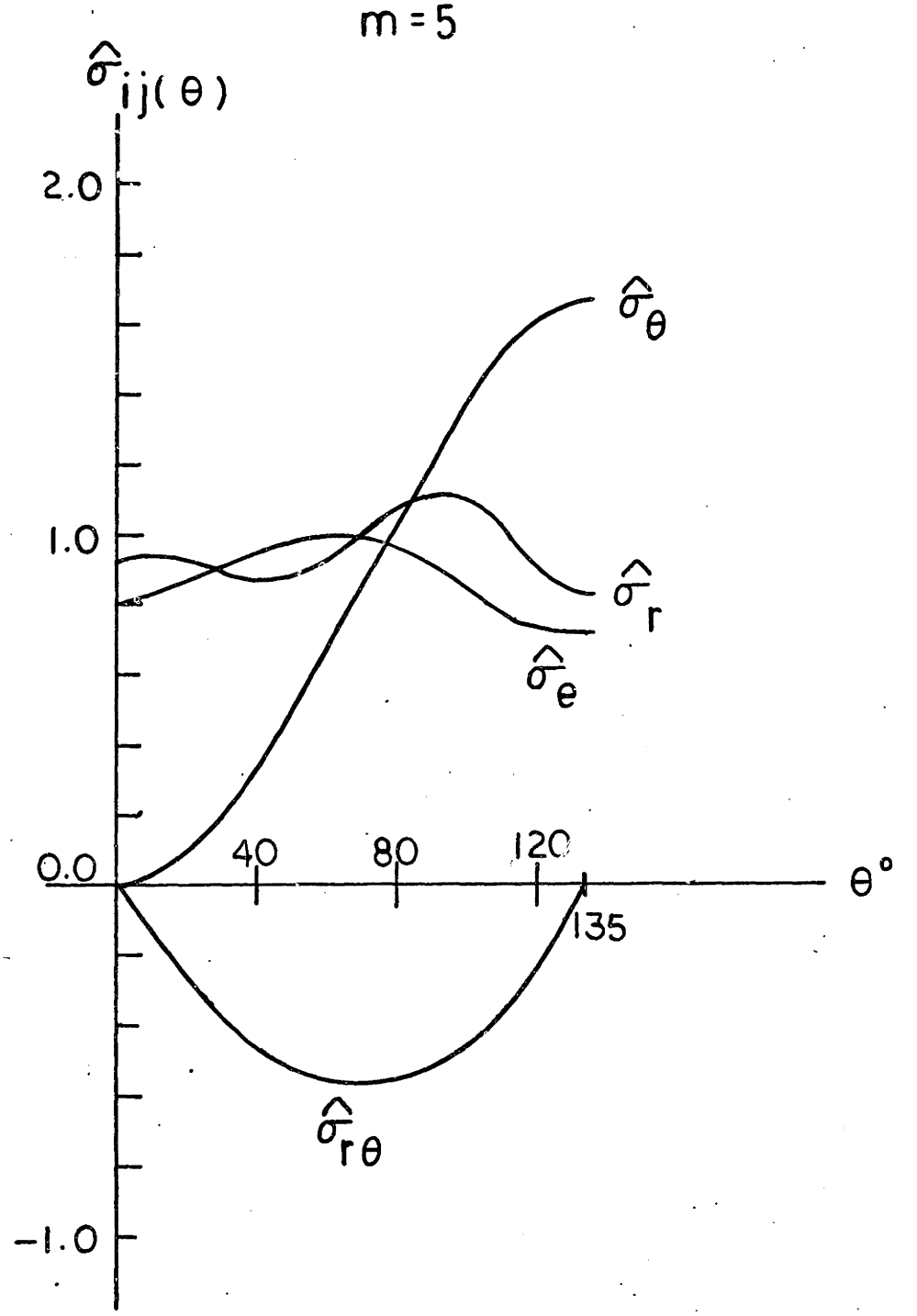

Figure 3.4 Variation of $\hat{\sigma}_{ij}$ with θ at the Apex of a Hard Particle of $\omega = \pi/4$, $m = 5$.

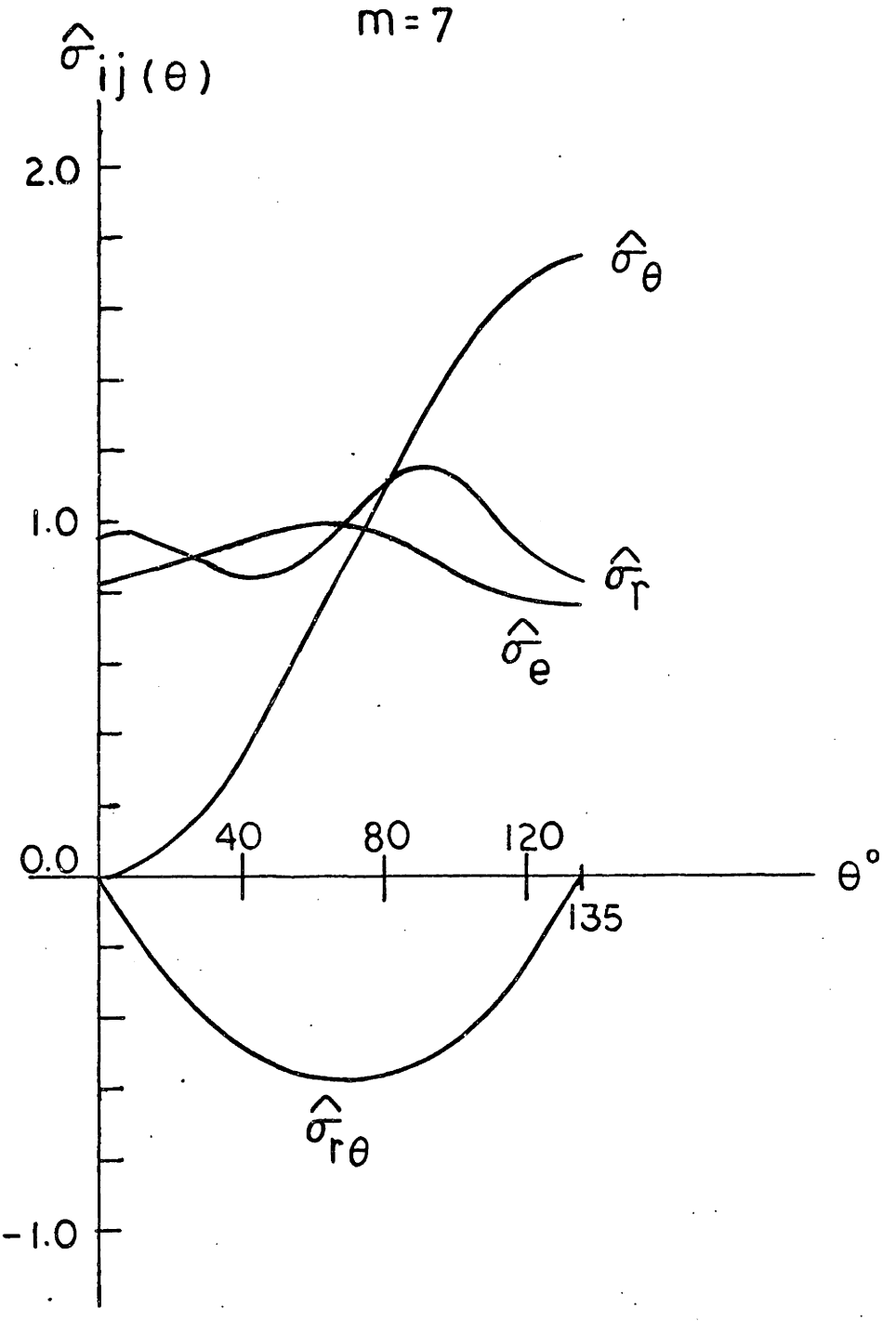

Figure 3.5 Variation of $\hat{\sigma}_{ij}$ with θ at the Apex of a Hard Particle of $\omega = \pi/4$, $m = 7$.

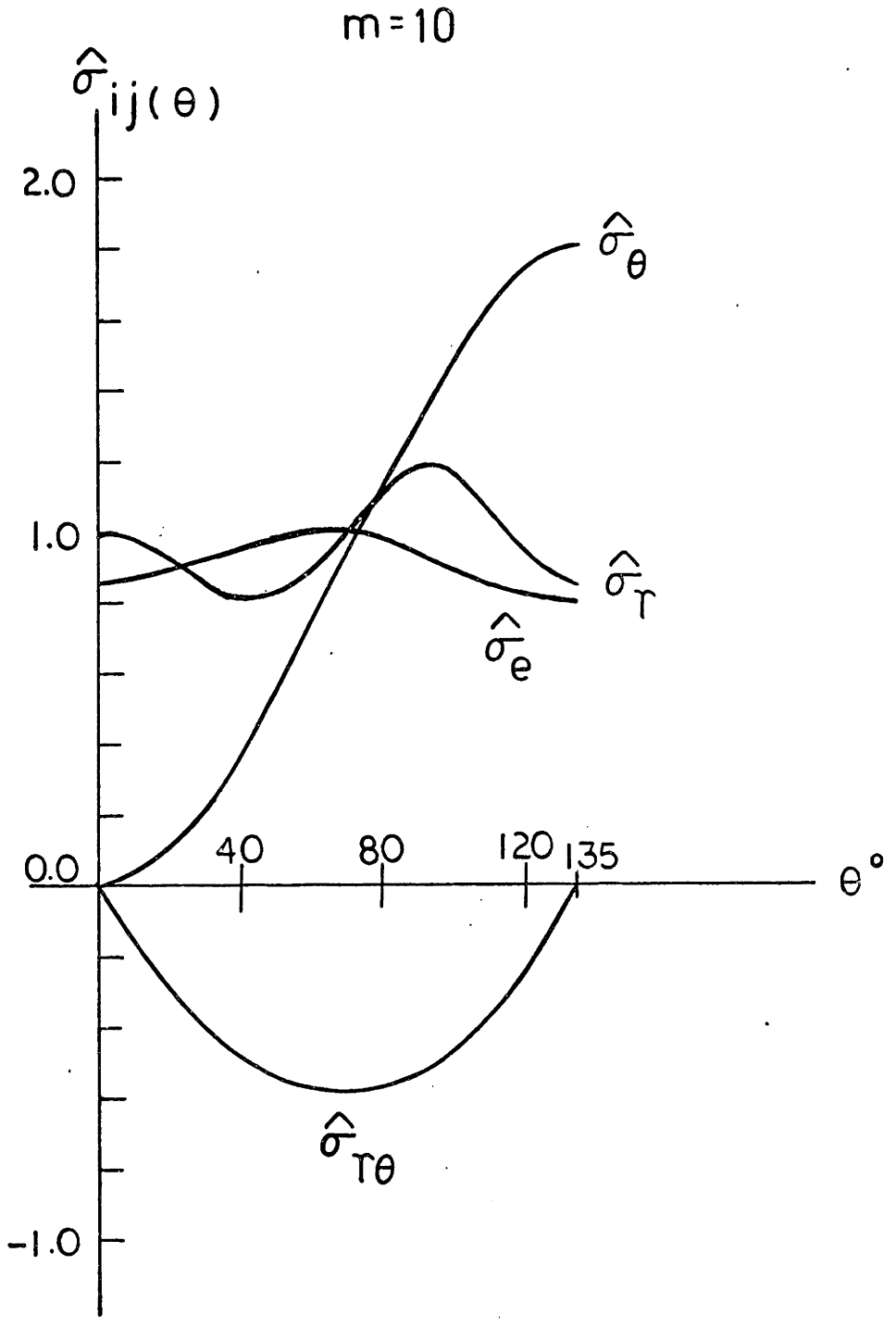

Figure 3.6 Variation of $\hat{\sigma}_{ij}$ with θ at the Apex of a Hard Particle of $\omega = \pi/4$, $m = 10$.

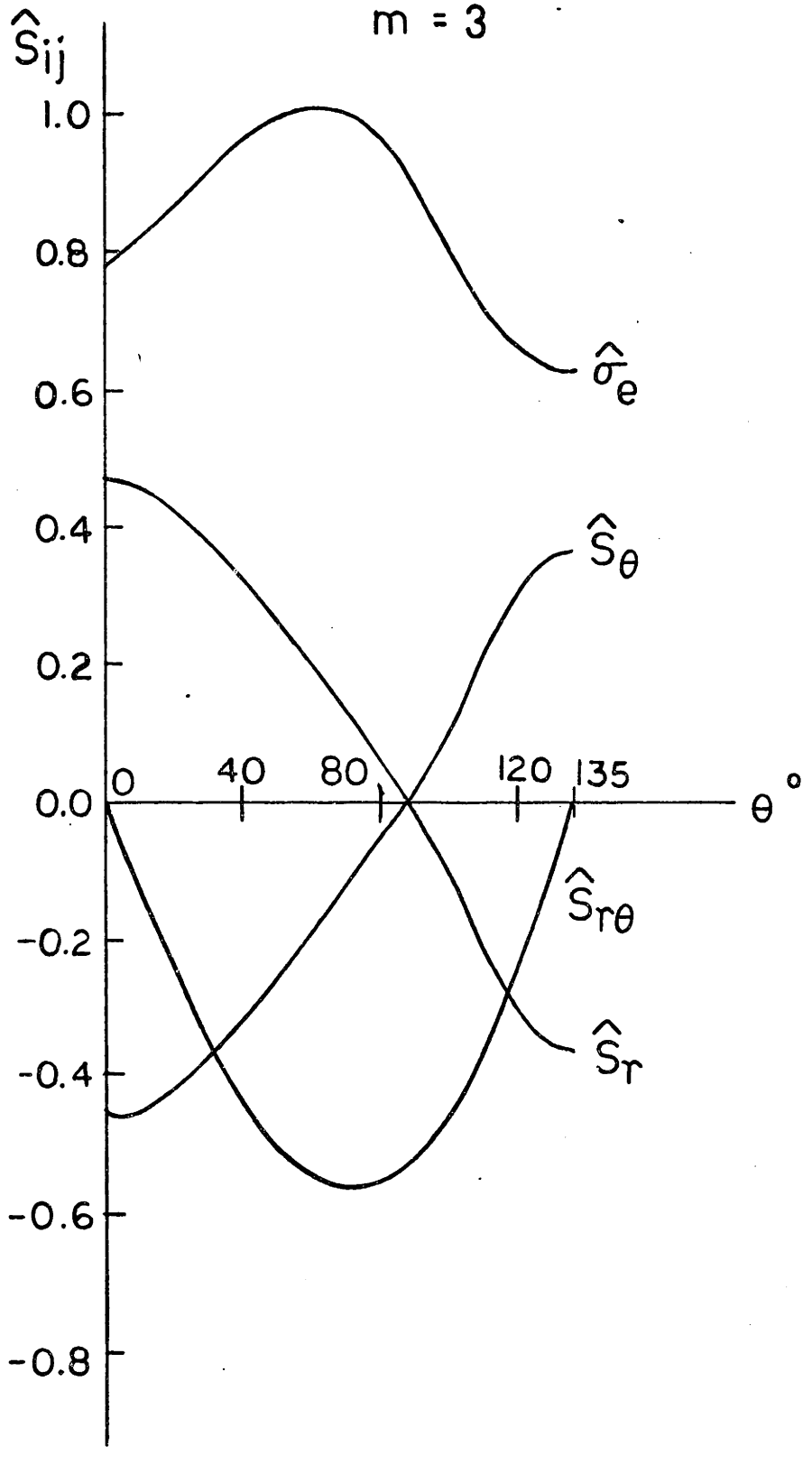

Figure 3.7 Variation of $\hat{S}_{ij}$ with θ at the Apex of a Hard Particle of $\omega = \pi/4$, $m = 3$.

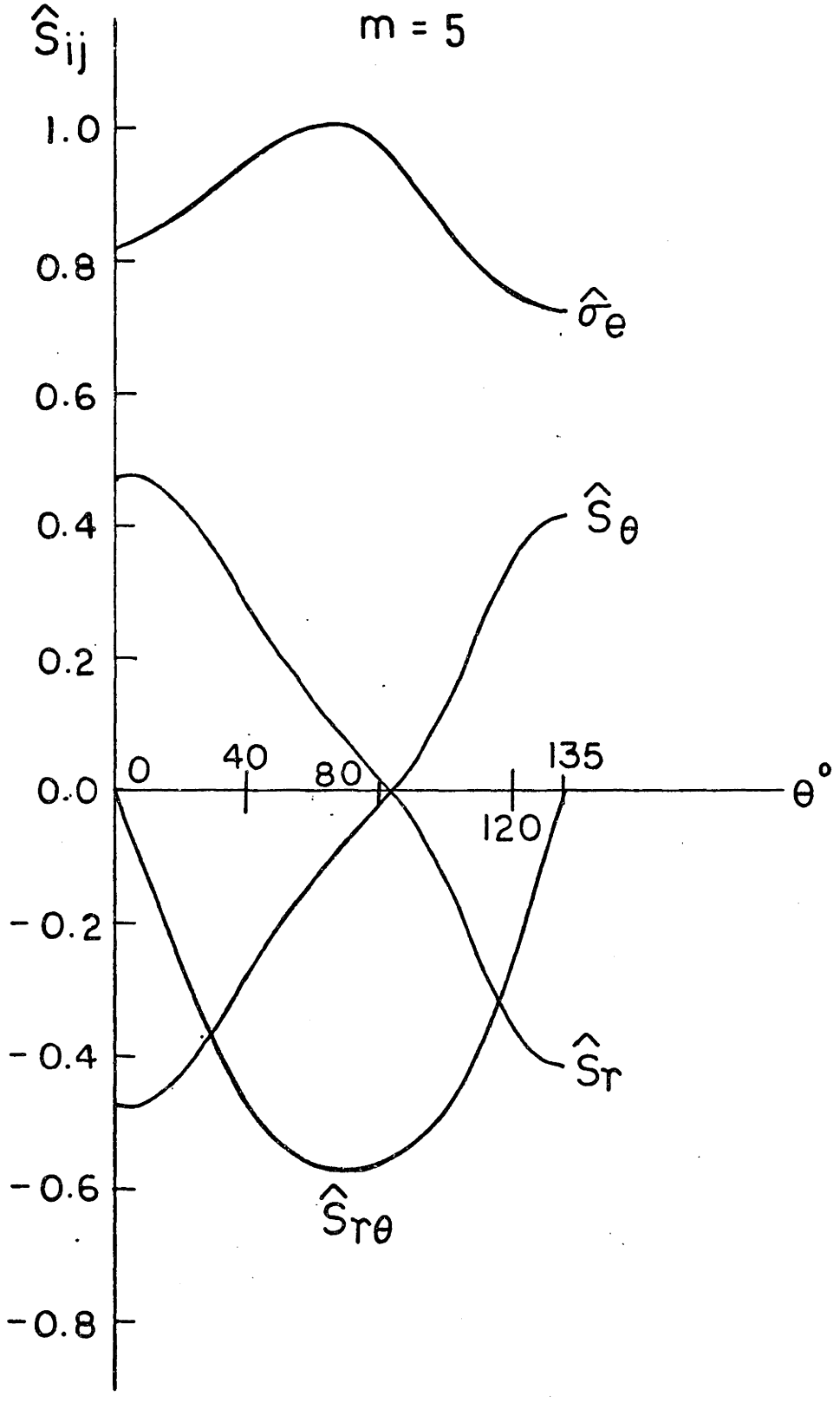

Figure 3.8 Variation of $\hat{S}_{ij}$ with θ at the Apex of a Hard Particle of $\omega = \pi/4$, $m = 5$.

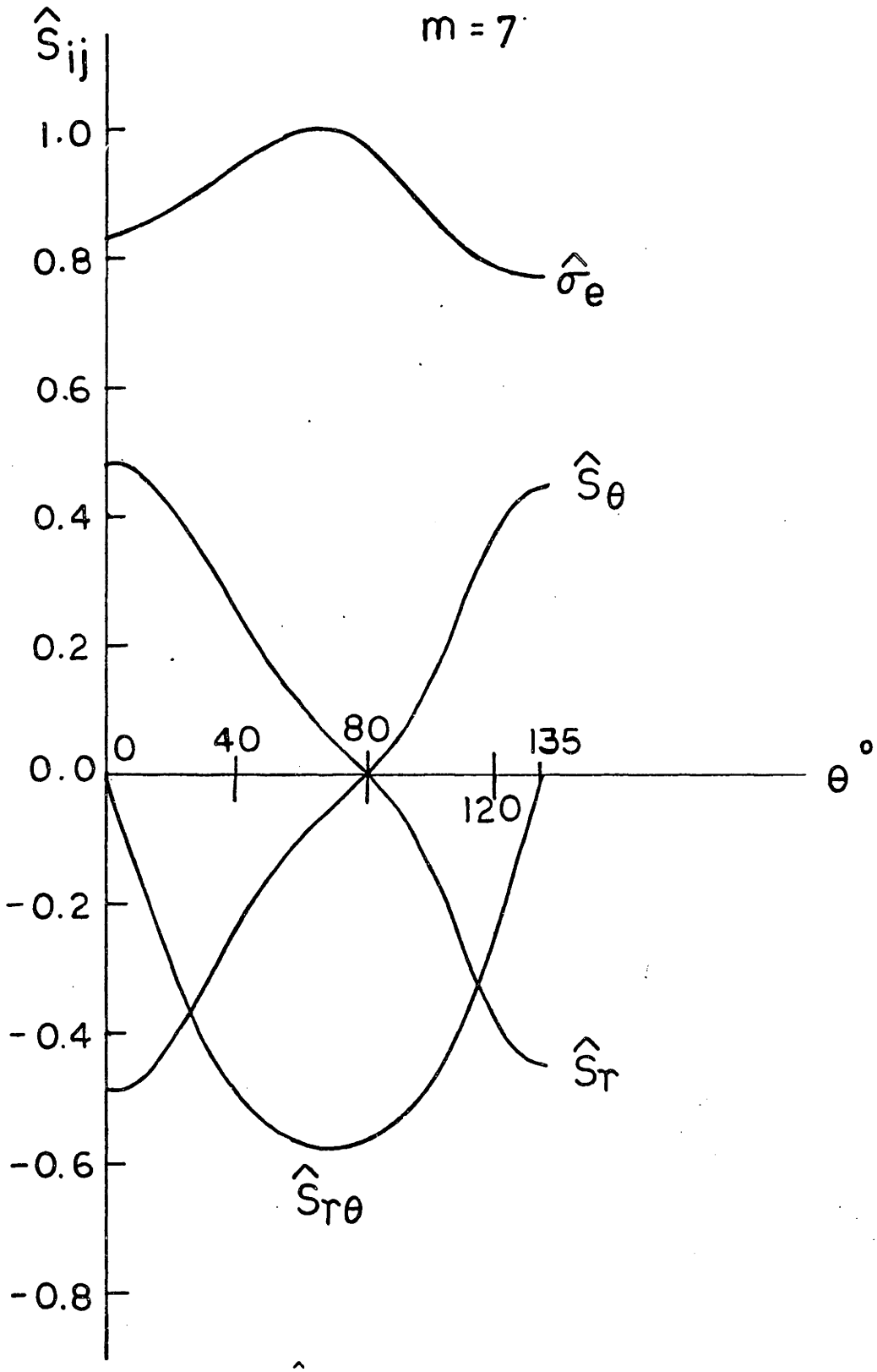

Figure 3.9 Variation of $\hat{S}_{ij}$ with θ at the Apex of a Hard Particle of $\omega = \pi/4$, $m = 7$.

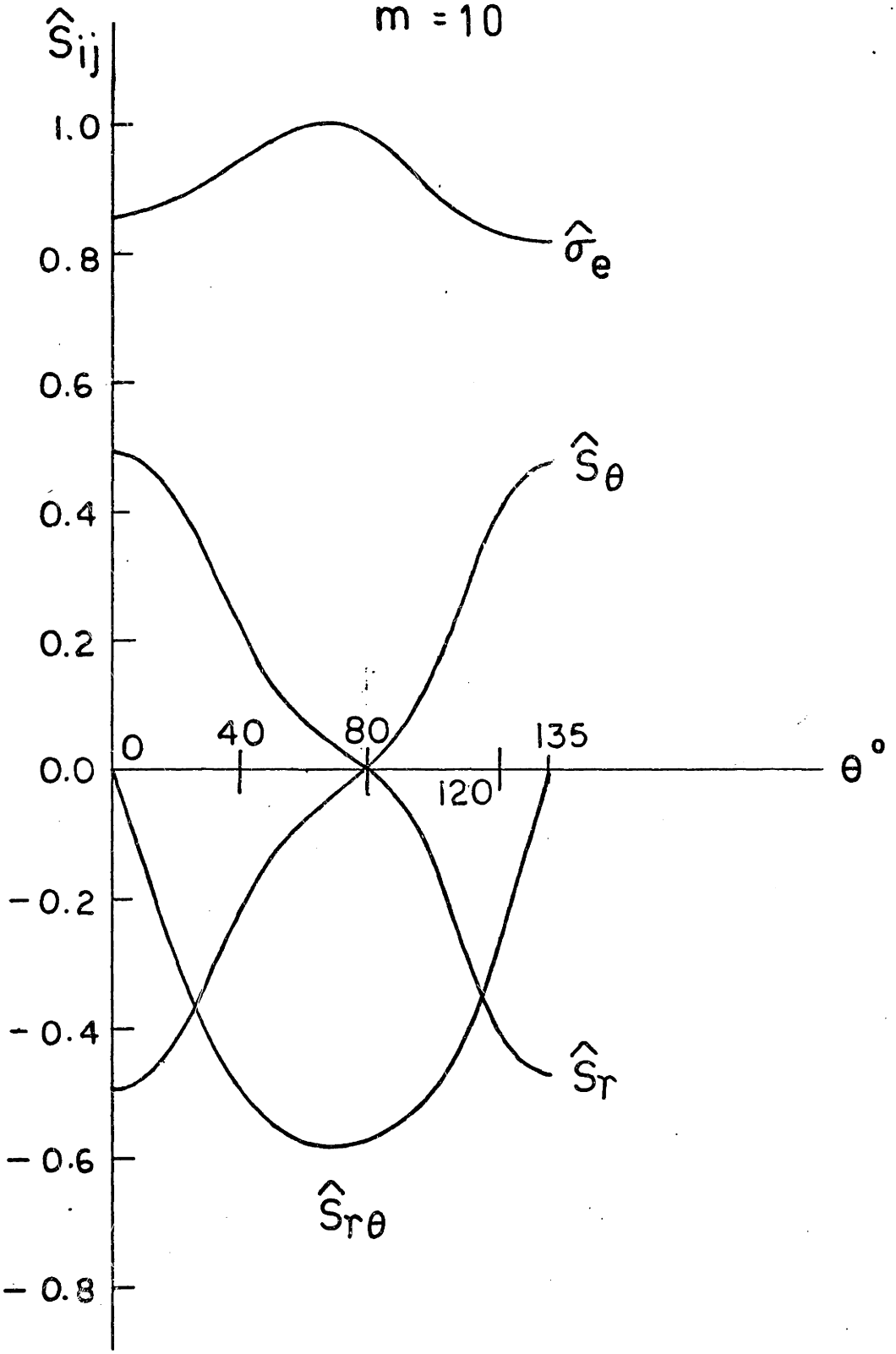

Figure 3.10 Variation of $\hat{S}_{ij}$ with θ at the Apex of a Hard Particle of $\omega = \pi/4$, $m = 10$.

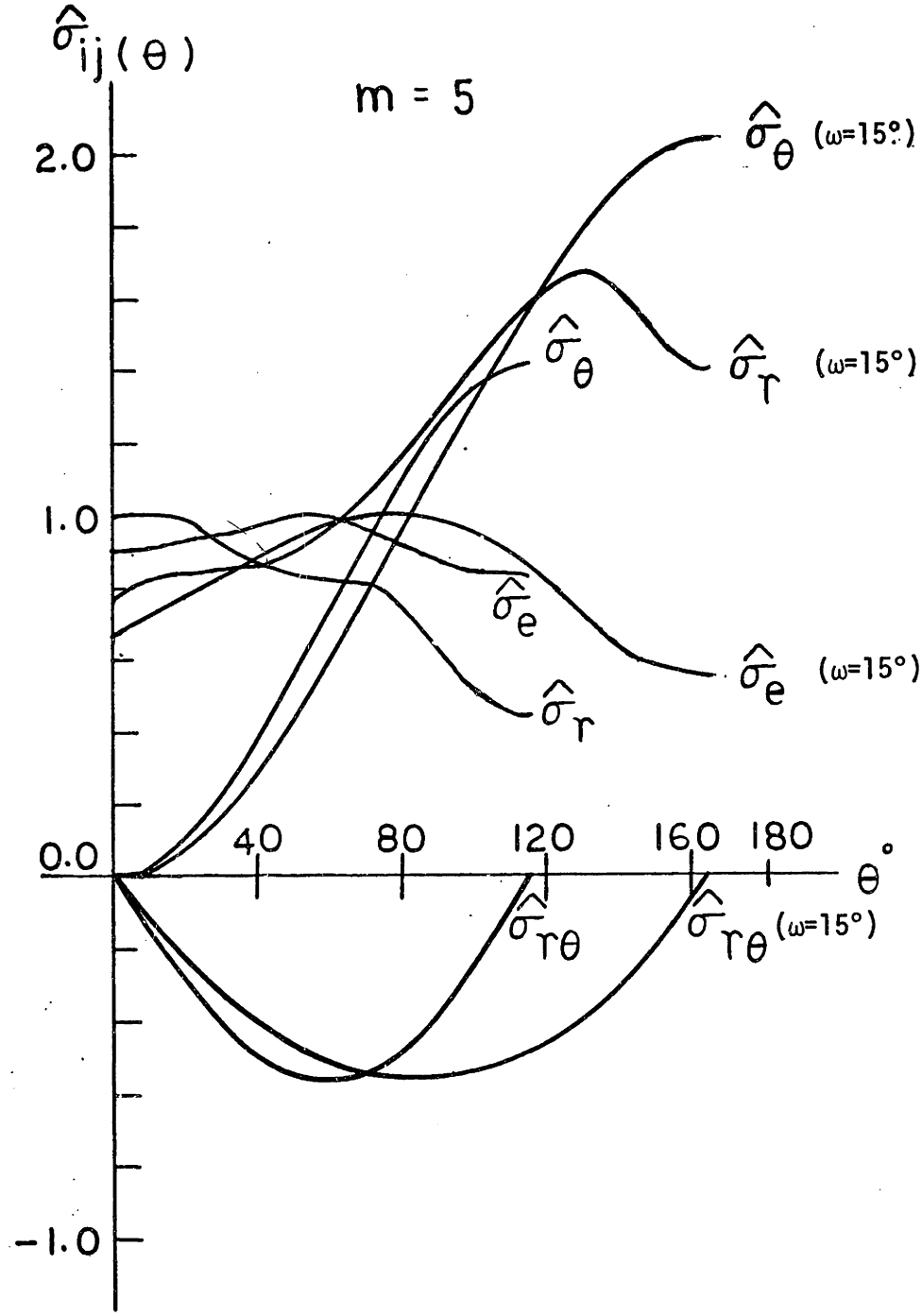

Figure 3.11 Variation of $\hat{\sigma}_{ij}$ with θ at Apexes of Hard Particles of $\omega = 15°$, $m = 5$.

incompatibility caused by the sliding interface boundary is diffused such that maximum shear activities always tend to be midway between the horizontal grain boundary and the slanted interface boundary.

Analogous to the m=1 results, however, the opening stress $\hat{\sigma}_\theta$ is always tensile at the particle-grain interface and zero at the horizontal grain boundary. This is the driving force for particle debonding and void nucleation.

In addition to λ becoming more negative, $\hat{\sigma}_\theta$ at the slanted interface boundary rises as ω decreases (γ increases). For the same ω, $\hat{\sigma}_\theta$ at the interface increases with m although λ grows to be less negative as m increases.

Figure 3.12 shows the slip line field for the limiting case of $m \to \infty$. This perfect plasticity solution confirms preceeding numerical results that σ_θ is always maximum and tensile across one of the sliding interfaces and compressive across the other.

3.3 The Triple Grain Junction

The boundary conditions at the triple grain junction (where three grain boundaries come together with 120° angles) in terms of $\hat{\phi}$ and its derivatives are shown

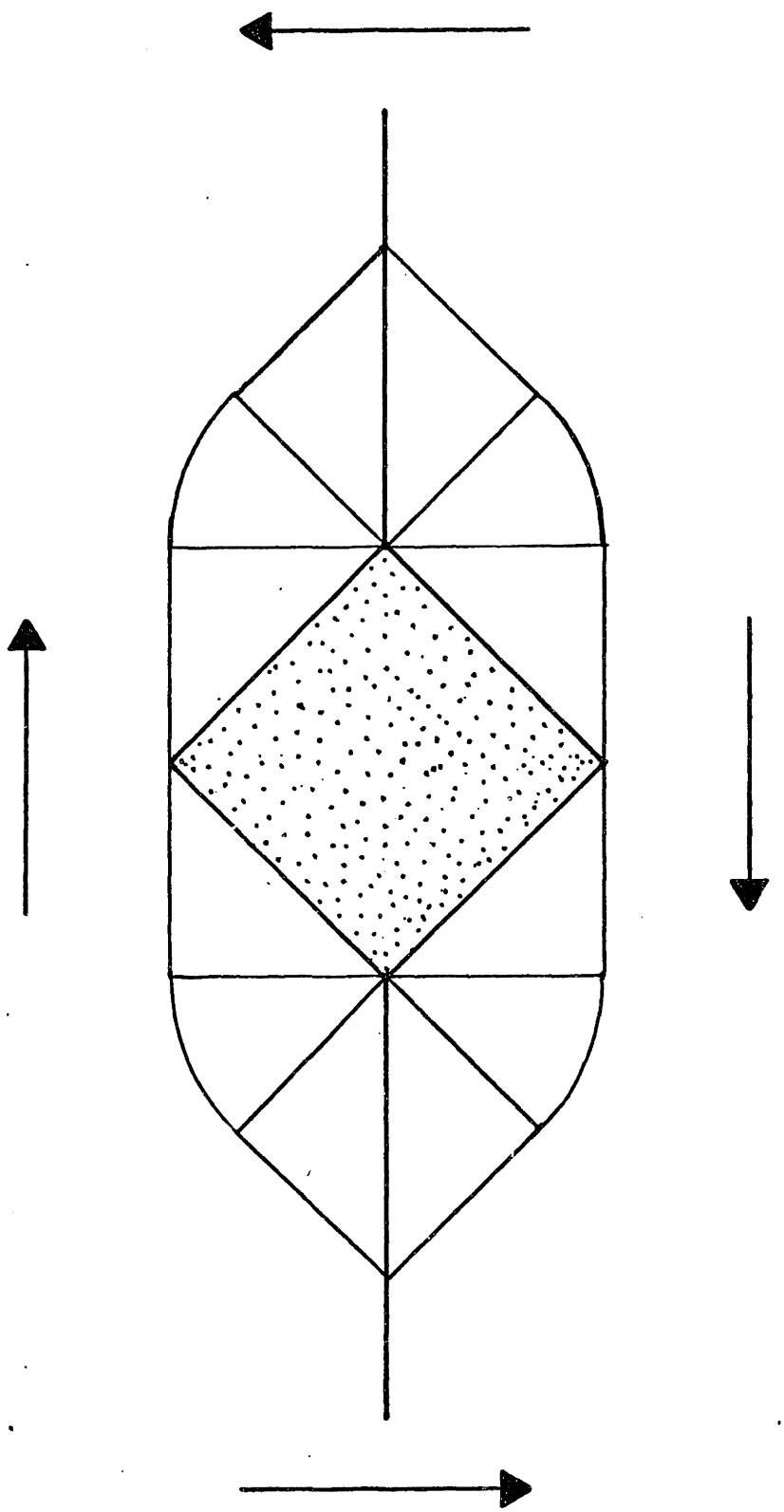

Figure 3.12 Slipline Solution for a Hard Particle of $\omega = \pi/4$.

in Fig. 3.13 in which $F(\hat{\phi}'', \hat{\phi}', \hat{\phi})$ stands for

$$\left\{\frac{3}{4}\left[(\hat{\phi}'')^2 + 2\lambda(\lambda+2)\hat{\phi}\hat{\phi}'' + \lambda^2(\lambda+2)^2\hat{\phi}^2\right] + 3(\lambda+1)^2\hat{\phi}'^2\right\}^{\frac{m-1}{2}} \times\left[\hat{\phi}'' + \lambda(\lambda+2)\hat{\phi}\right] \tag{3.11}$$

Equation 3.7 is solved in both grains I and II by shooting from LS and SR simultaneously towards TS where the solutions in the two grains are matched and compared with prescribed boundary conditions. Again, the fourth order Runga-Kutta algorithm is used to integrate Eq. 3.7. A Simpson's rule is employed to integrate F in Eq. 3.11 and the quasi Newton-Raphson method is used to solve for roots of the mismatches to arrive at the correct initial values of g, h, k, and s defined in Fig. 3.13.

Figure 3.14 pictures the variation of λ with m (actual values are given in Table 3.2) Analogous to the solution of the rigid particle problem, λ becomes less negative as m increases. Thus following a similarly sensible trend as the one described in Section 3.2.

Figures 3.15 to 3.18 display $\hat{\sigma}_{ij}$ versus θ for m=3, 5, 7, 10 respectively and Figs. 3.19 to 3.22 show the corresponding deviatoric stresses $\hat{S}_{ij}$ versus θ. It is at once clear that the maximum shear activities are always at $\pi/3$ which is the midway between the horizontal and the slanted boundaries as well as the extension

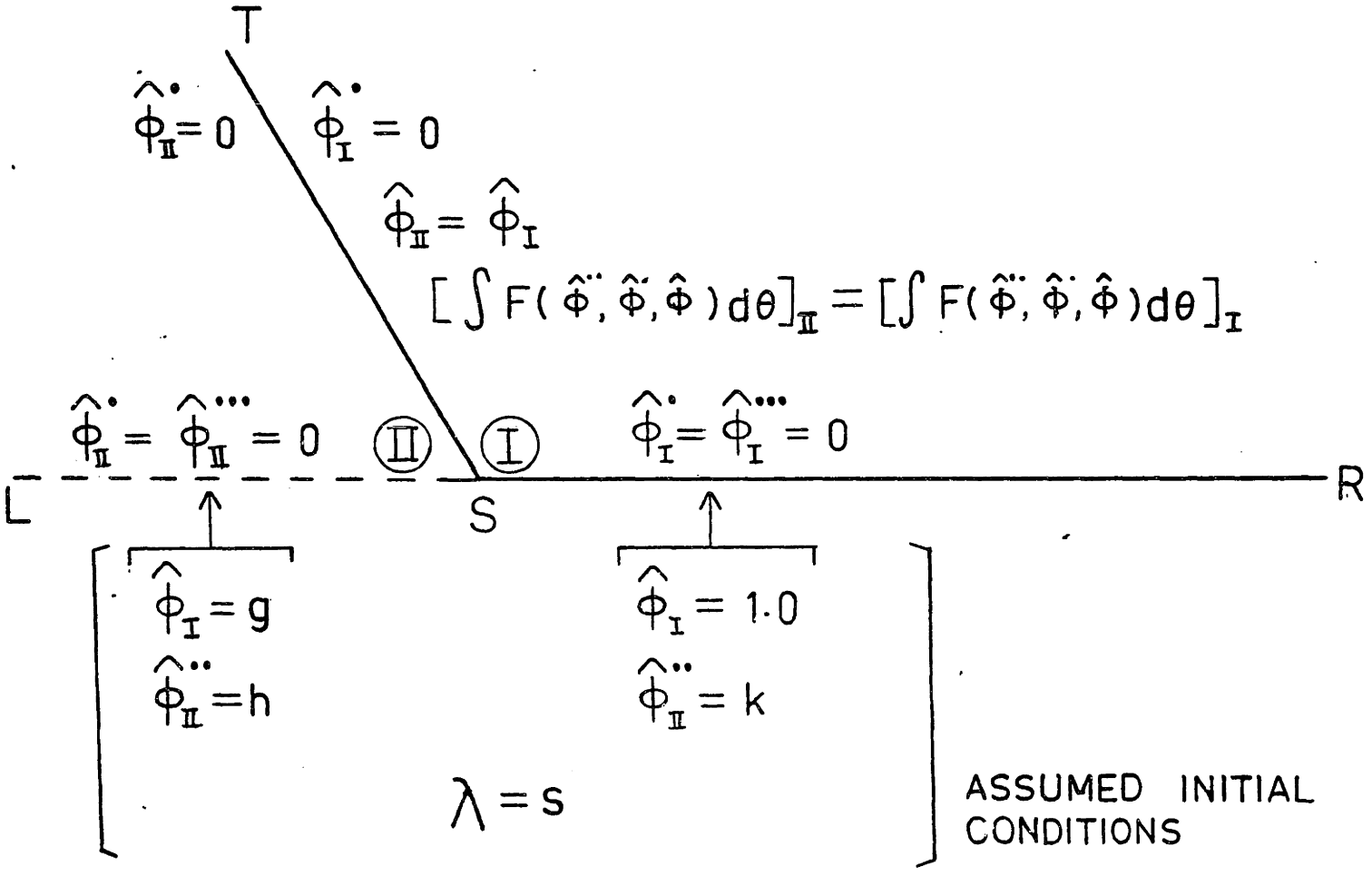

Figure 3.13 Operational Boundary Conditions at Triple Grain Junction Subject to Far Field Tensile Loading.

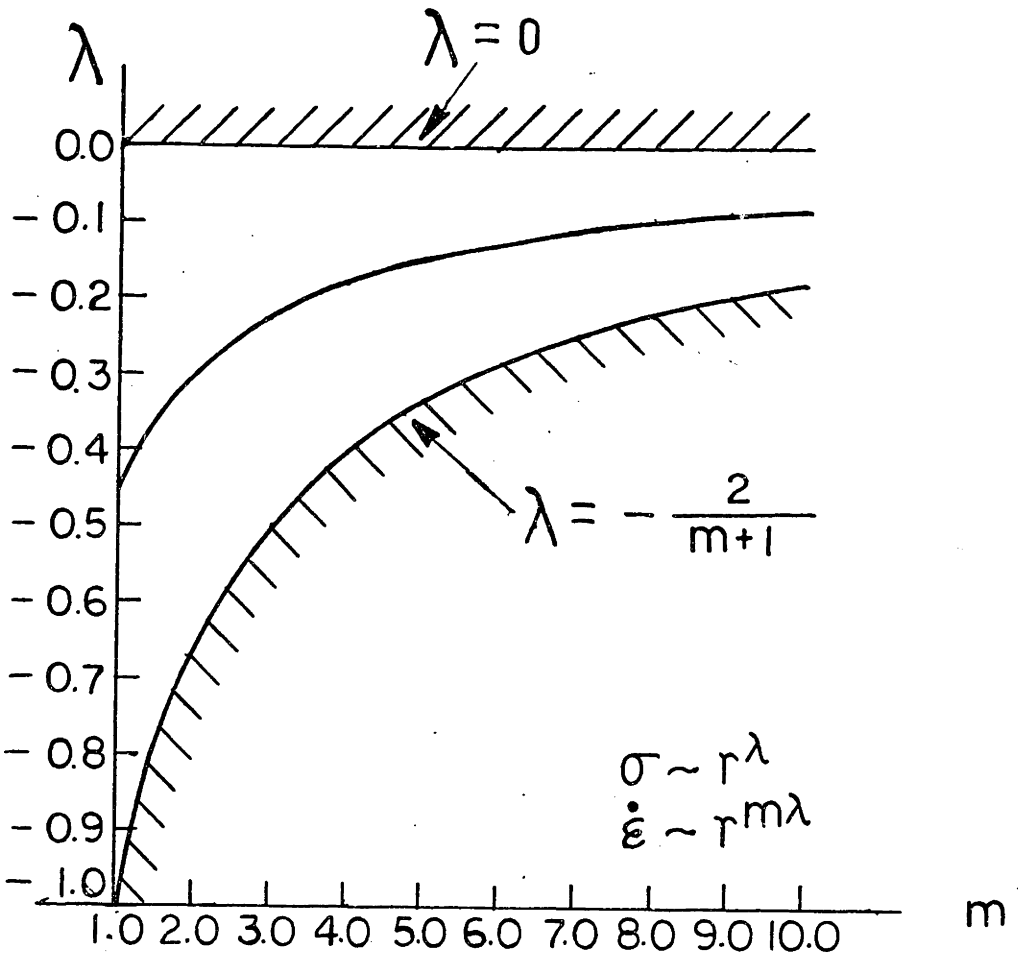

Figure 3.14 Variation of λ with m at the Triple Grain Junction.

TABLE 3.2

λ AND $m\lambda$ FOR INTEGER VALUES OF m FOR THE TRIPLE GRAIN JUNCTION

m	λ ($\sigma \sim r^{\lambda}$)	$m\lambda$ ($\dot{\varepsilon} \sim r^{m\lambda}$)
1	-0.449	-0.449
2	-0.312	-0.624
3	-0.231	-0.693
4	-0.182	-0.728
5	-0.150	-0.750
6	-0.128	-0.768
7	-0.112	-0.784
8	-0.099	-0.792
9	-0.089	-0.801
10	-0.081	-0.810

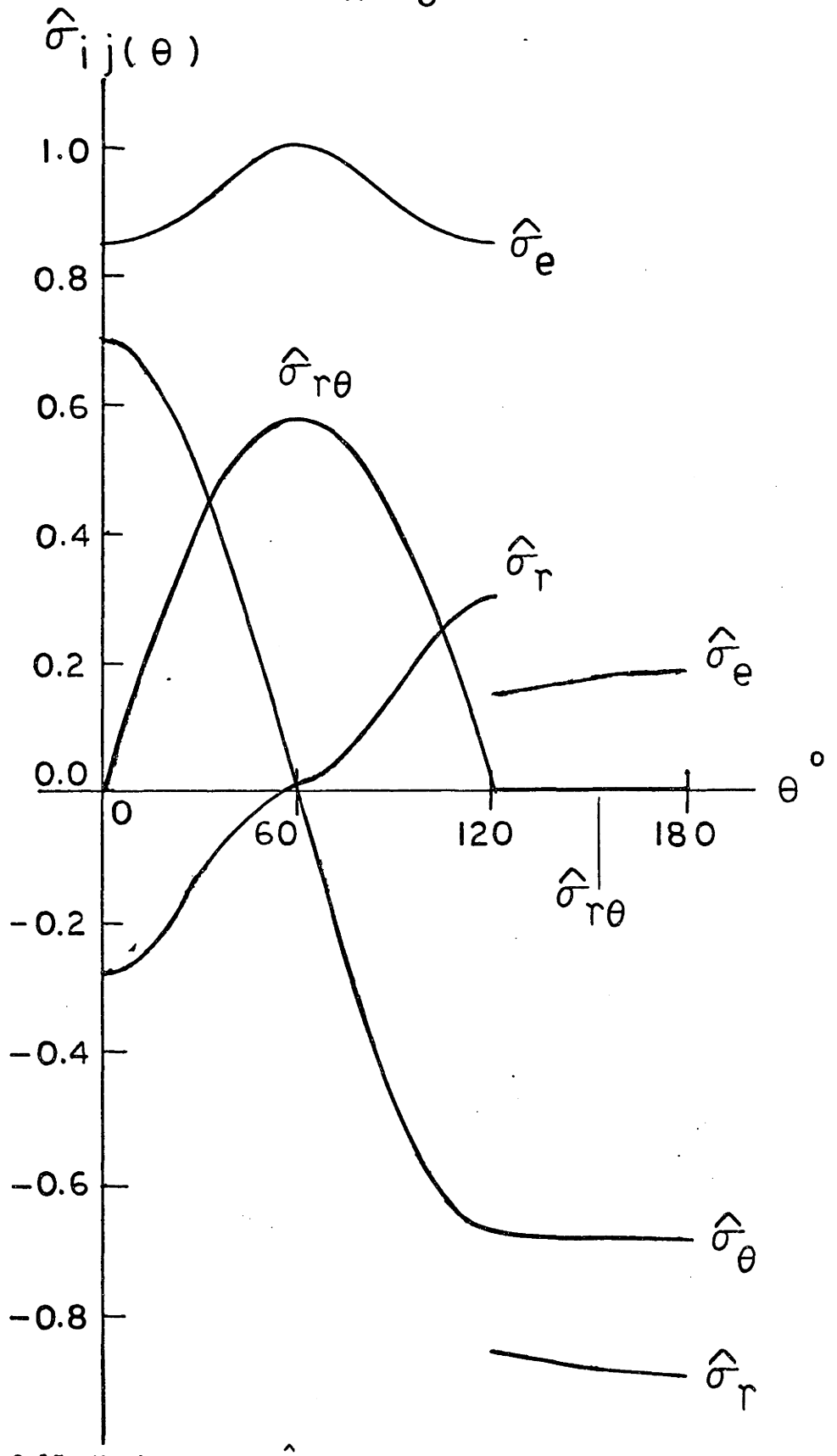

Figure 3.15 Variation of $\hat{\sigma}_{ij}$ with θ at Triple Grain Junction, m = 3.

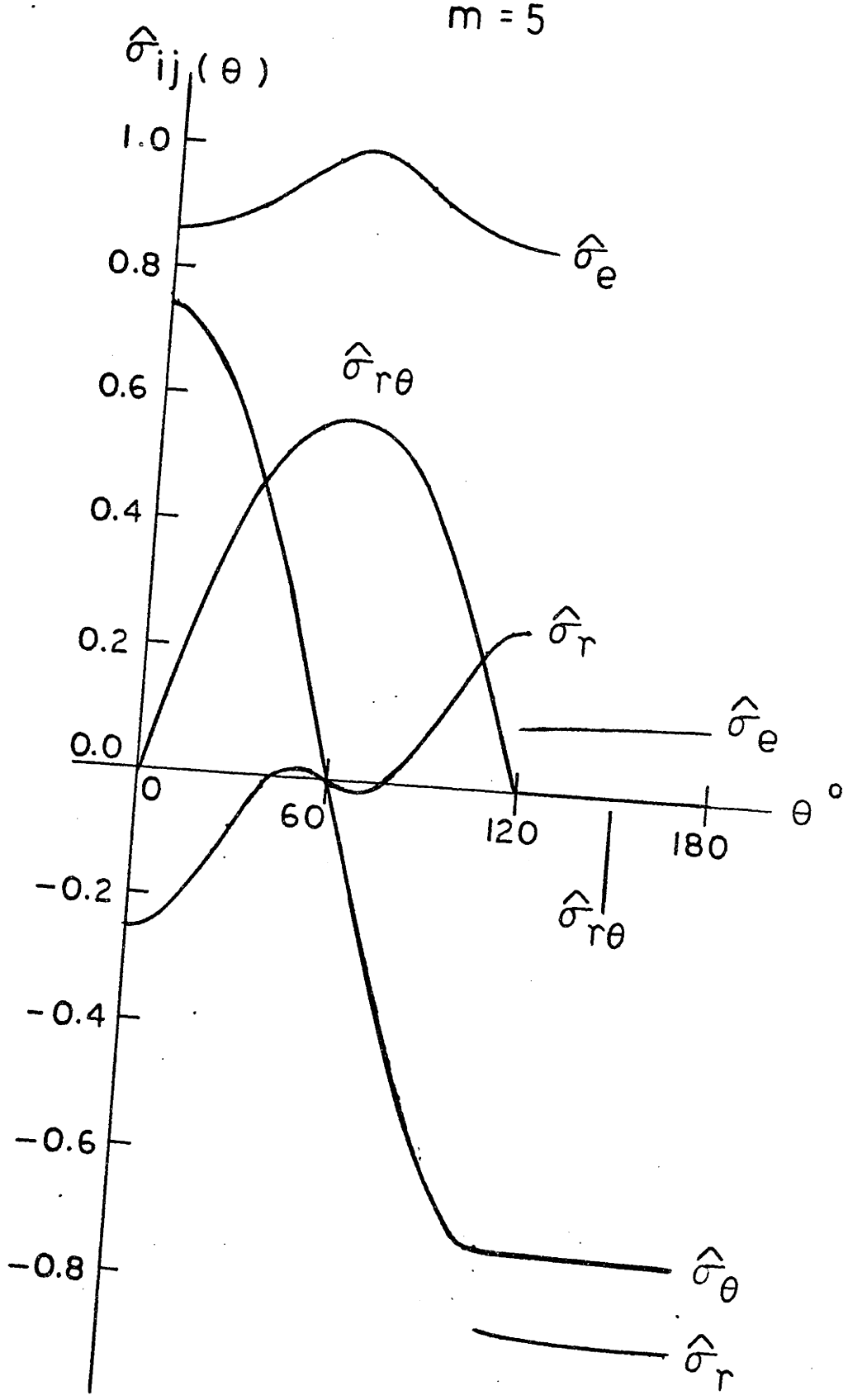

Figure 3.16 Variation of $\hat{\sigma}_{ij}$ with θ at Triple Grain Junction, m = 5.

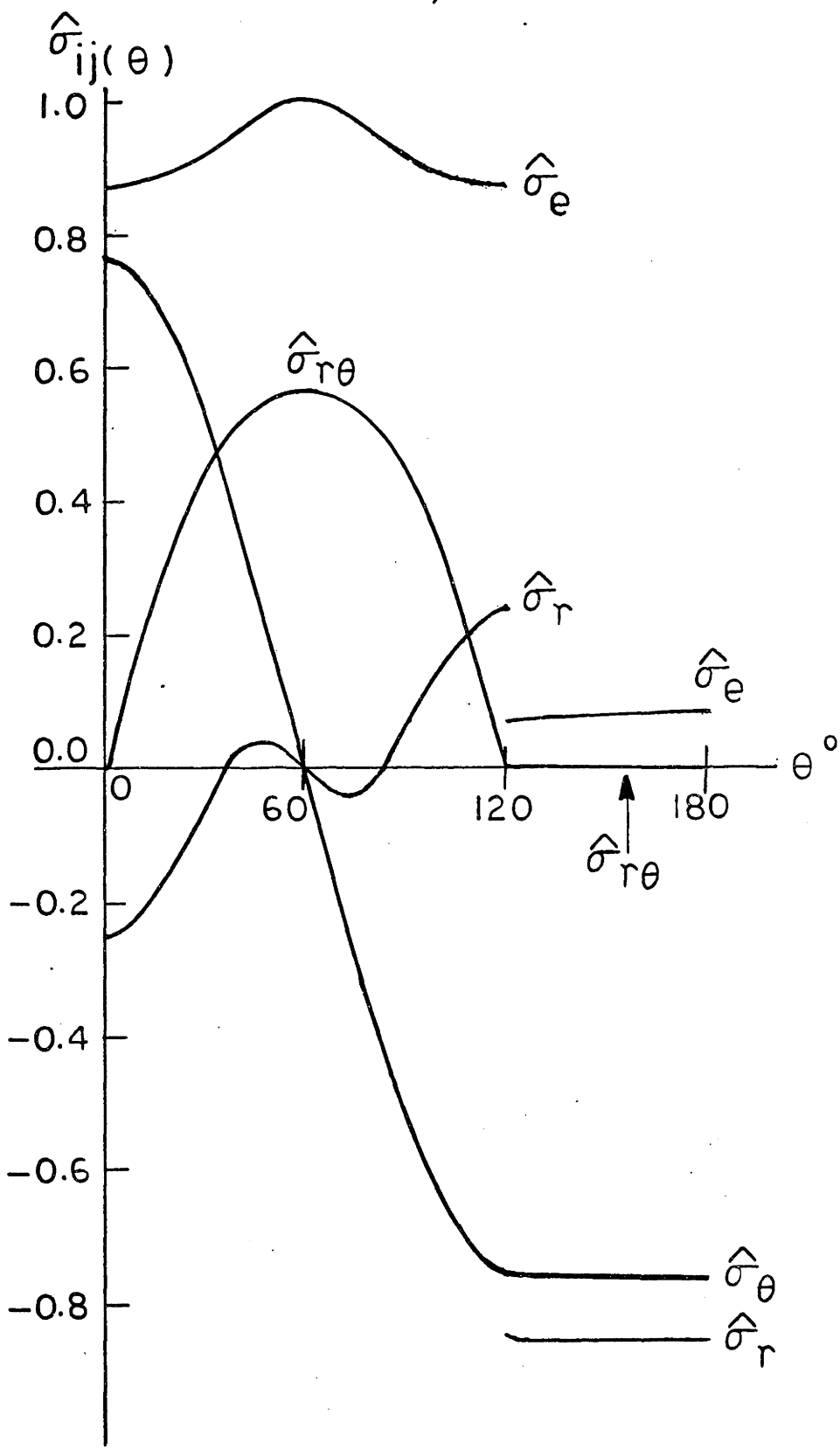

Figure 3.17 Variation of $\hat{\sigma}_{ij}$ with θ at Triple Grain Junction, m = 7.

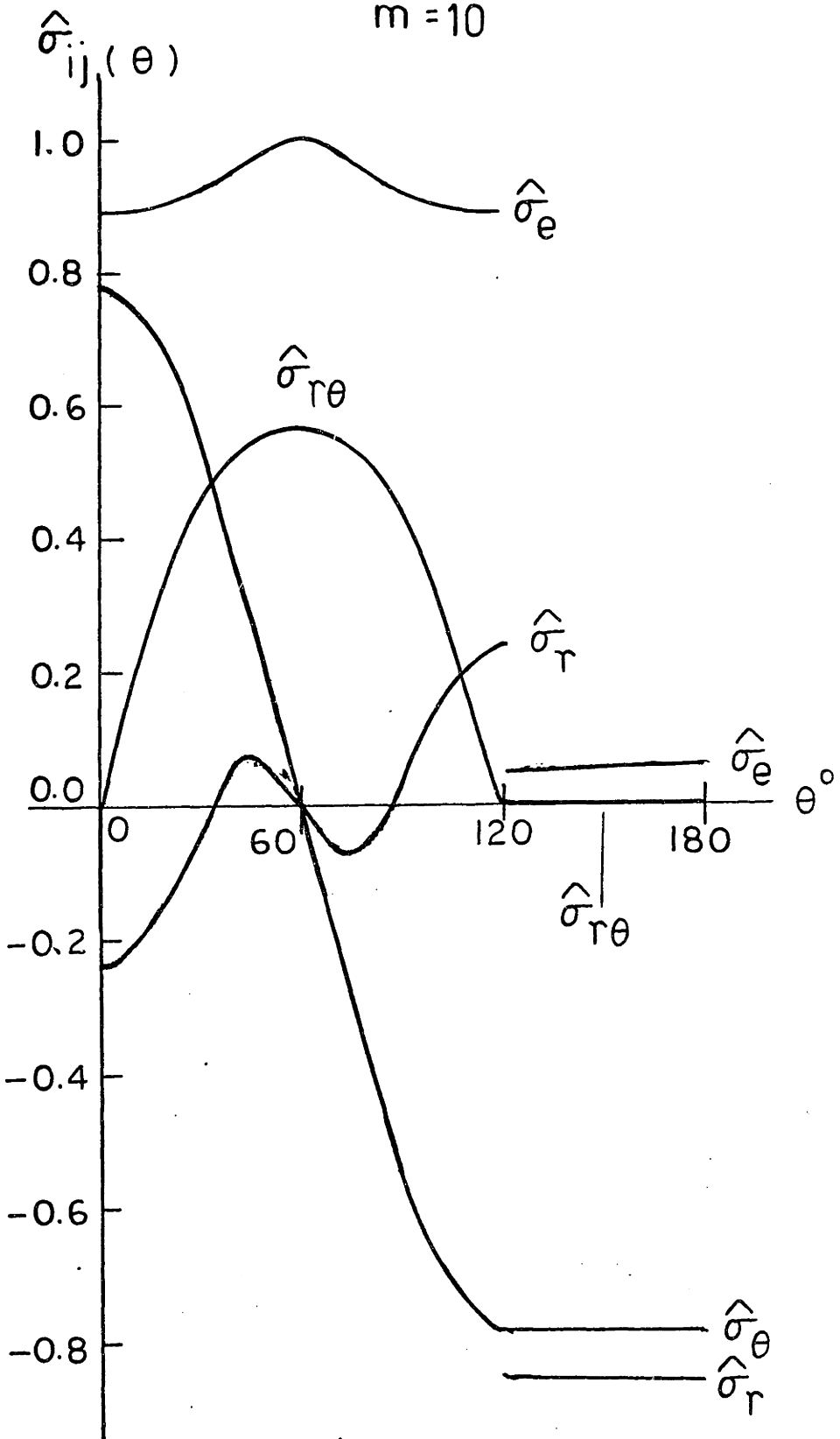

Figure 3.18 Variation of $\hat{\sigma}_{ij}$ with θ at Triple Grain Junction, m = 10.

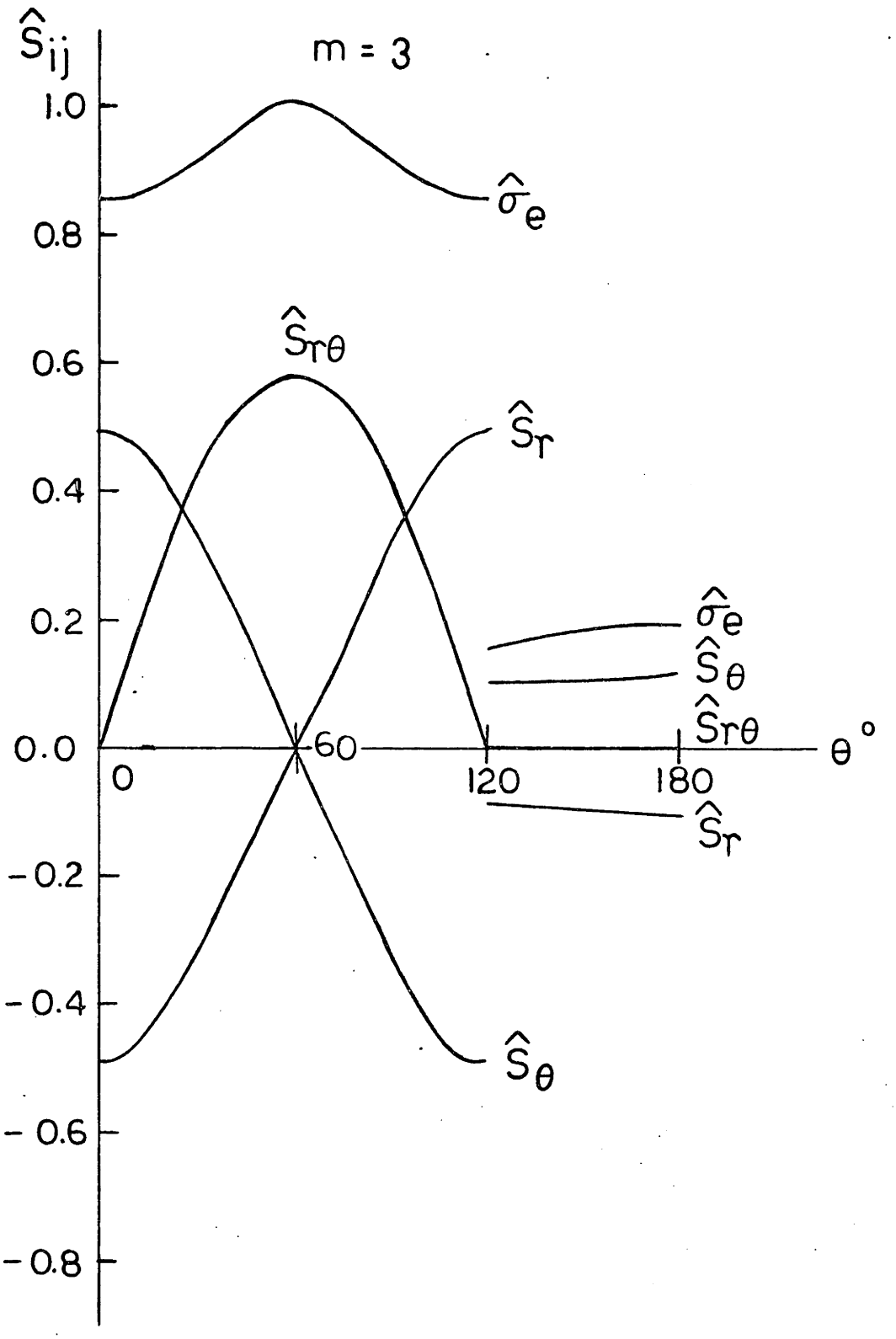

Figure 3.19 Variation of $\hat{S}_{ij}$ with θ at Triple Grain Junction, m = 3.

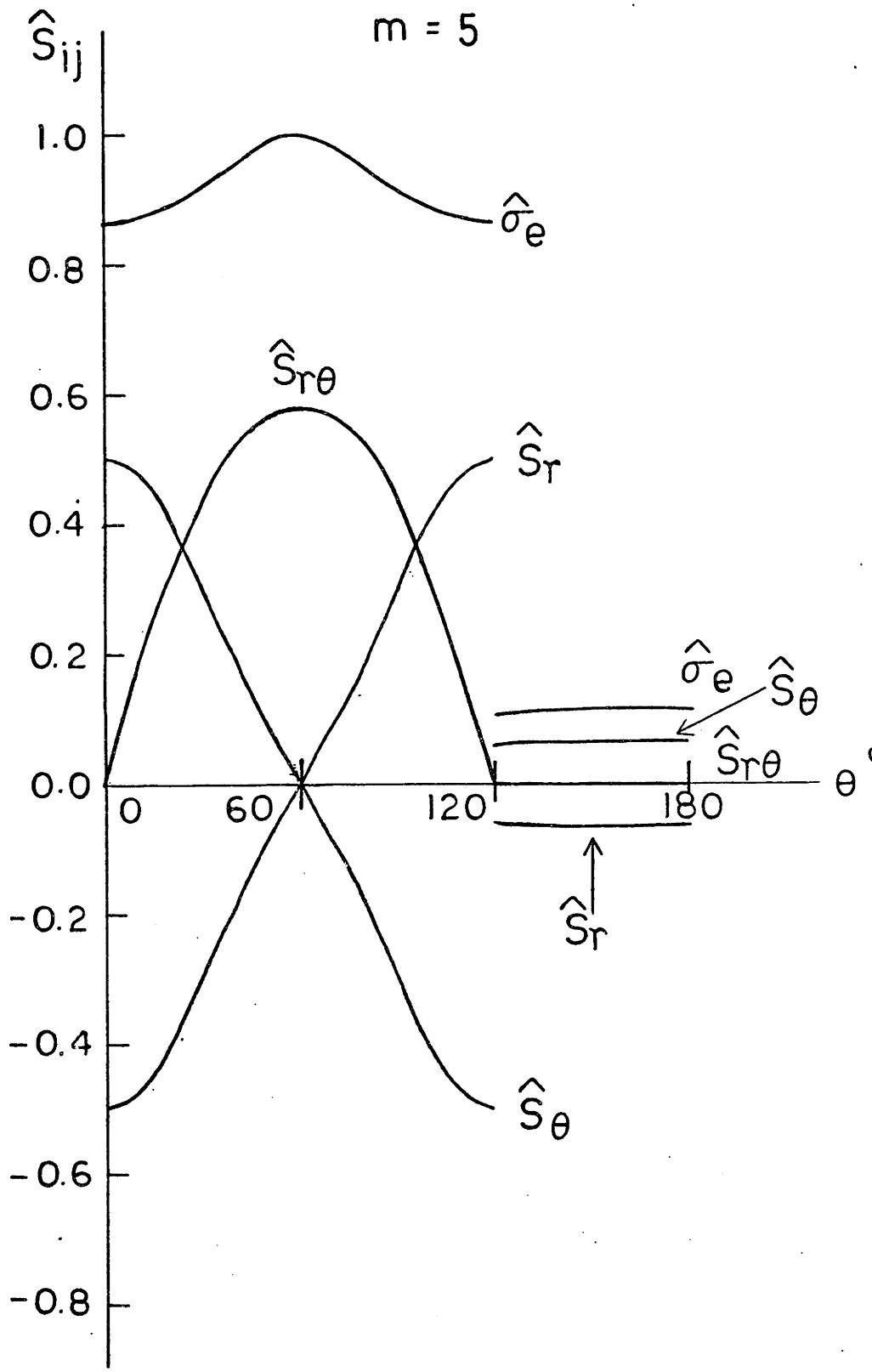

Figure 3.20 Variation of $\hat{S}_{ij}$ with θ at Triple Grain Junction, m = 5.

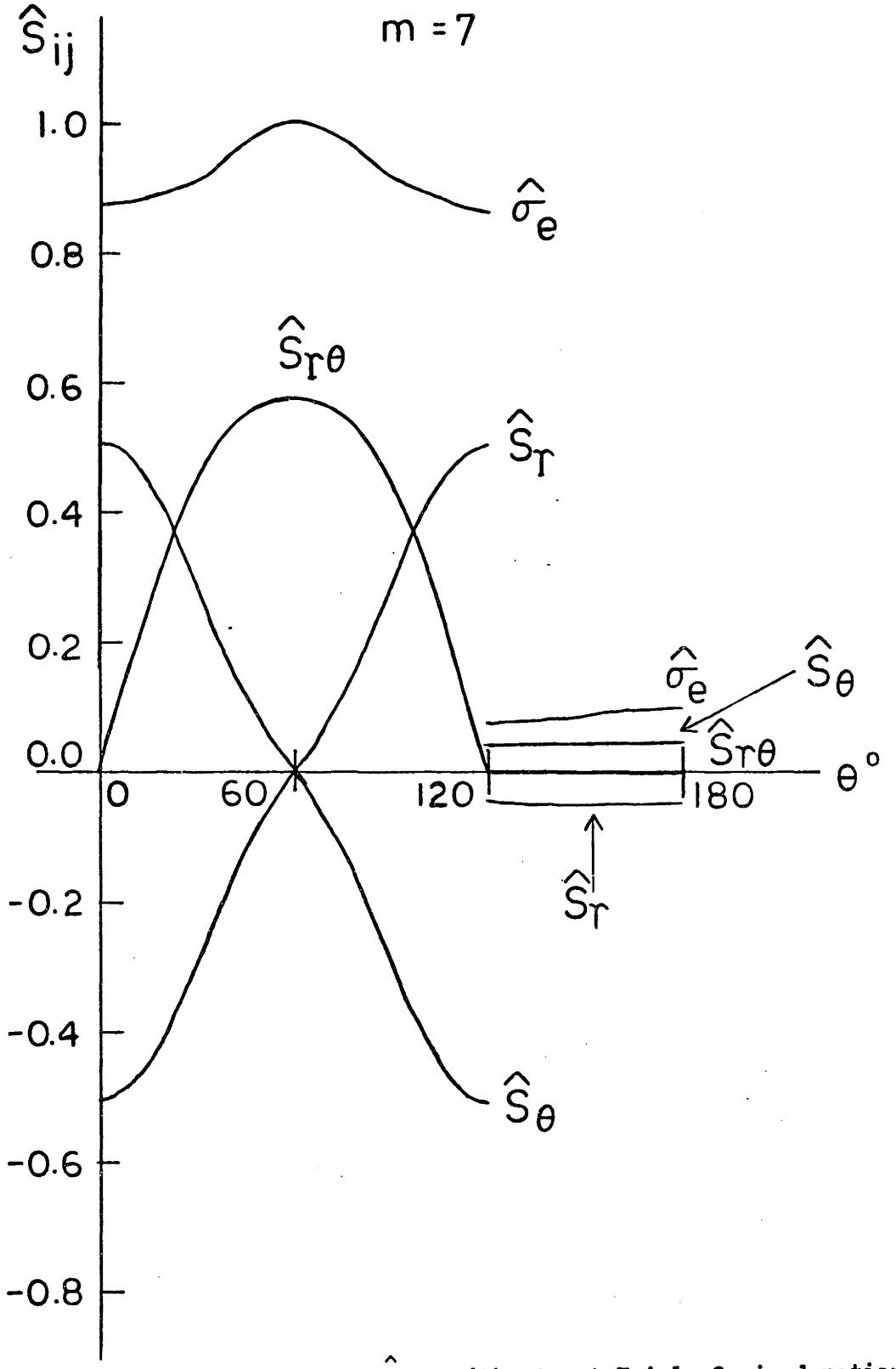

Figure 3.21 Variation of $\hat{S}_{ij}$ with θ at Triple Grain Junction, m = 7.

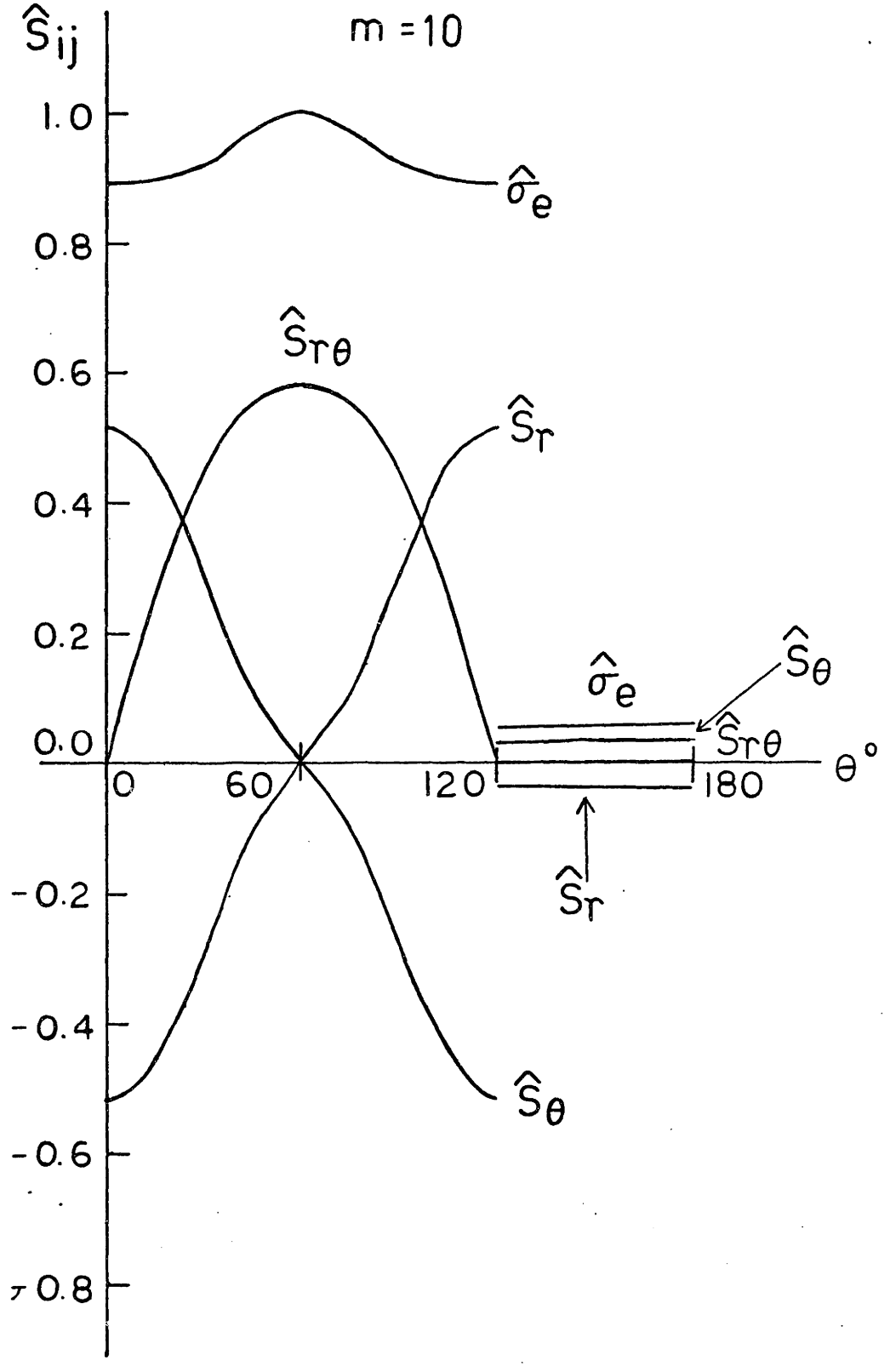

Figure 3.22 Variation of S_{ij} with θ at Triple Grain Junction, m = 10.

of a sliding slanted boundary. Stresses in grain II reveal that a nearly rigid pocket is being created there as m increases. The flow situation then resembles a well lubricated wedge being driven sideways into a vertically elongating specimen. Similar to the results for m=1 the opening stress $\hat{\sigma}_\theta$ is always tensile and maximum at the horizontal grain boundary, and compressive at the slanted grain boundary. Its magnitude increases slightly with m. Again, this distribution of $\hat{\sigma}_\theta$ gives theoretical explanation to numerous experimental observations that creep voids and cracks develop dominantly in grain boundaries perpendicular to the nominal tensile axis. This $\hat{\sigma}_\theta$ distribution dictates that these boundaries are favored sites for void nucleation. At the initial stage of damage formation, the existence of microvoids does not significantly alter the stress state. Thus, these boundaries are also the favored sites for void and finally crack growth.

Figure 3.23 shows the slipline field within the grains at the ideal plasticity limit where $m \to \infty$. This solution was also independently discovered by Brunner and Grant (1956). Although the stresses in the rigid region ABCD are indeterminate, this solution does confirm preceeding numerical results that a rigid pocket is developed in the corner DAB. This slipline field further reveals

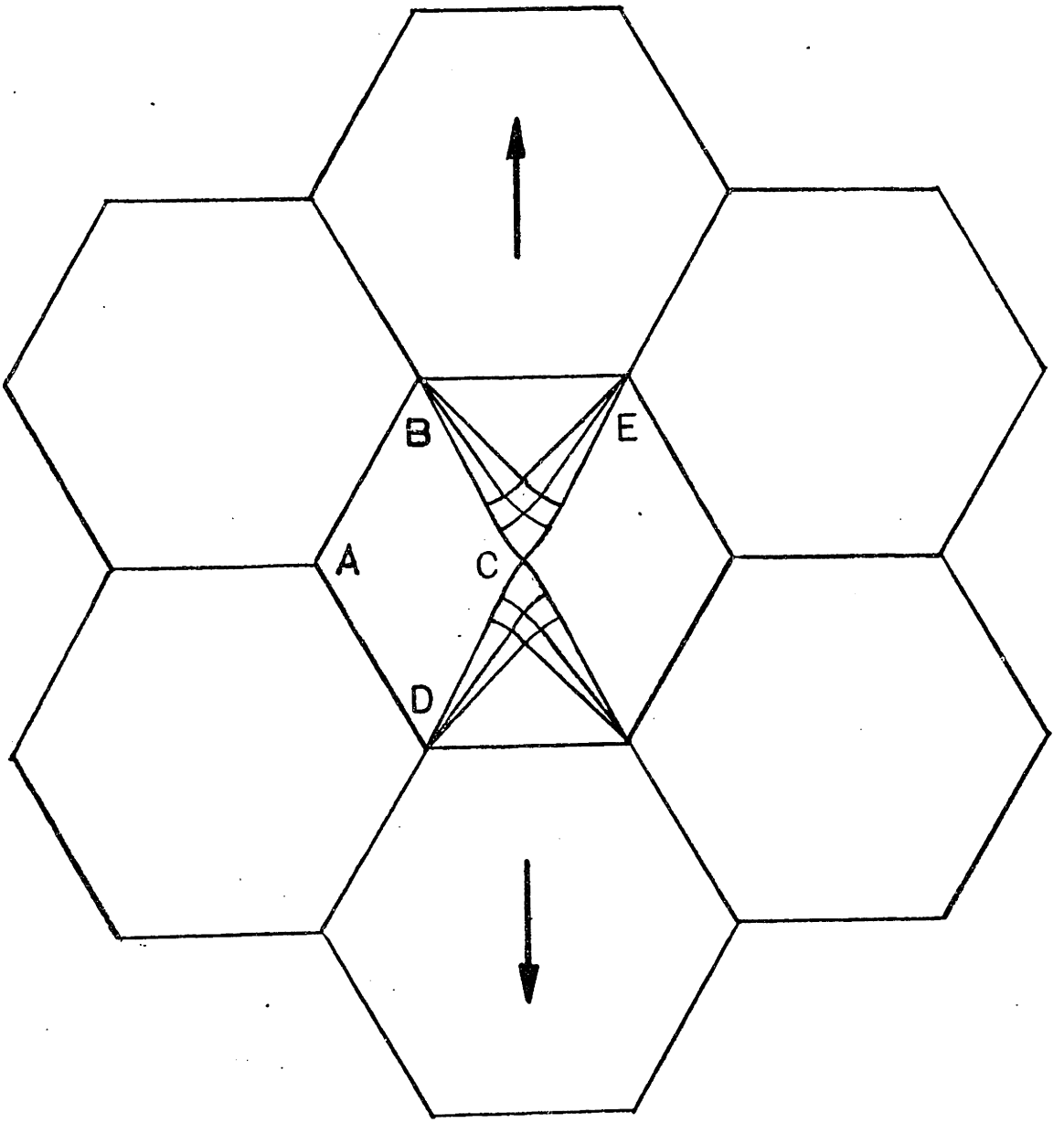

Figure 3.23: Slipline Solution at Triple Grain Junction

that the sliding of the slanted grain boundaries is being propagated into the adjoining opposite grain to form shear fan zones at B and E. This zone is flanked by α lines forming a shear fan of 17.5° width, at the extension of the slanted sliding boundary. This feature again agrees with the results of the preceeding computation. Indeed, intense shear activities manifested in the form of folds have long been observed in this location in creeping polycrystalline metal (Grant and Chaudhri 1965).

3.4 Discussion

Hutchinson's (1968) approach to analyze stationary cracks in a hardening plastic material has been extended to determine the stress singularities, at both the apexes of grain boundary hard particles and the triple grain junctions, caused by grain boundary sliding accommodated by power-law creep. The resulting stress distributions are not only physically reasonable, but also correlate and explain experimental observations.

These stress distributions are results of Eq. 3.5 which is based on the J_2 deformation theory. By the theorem of Ilyushin (1946) and by Hoff's (1954) analogy, the stress distribution is always proportional and without reversal in monotonic power-law creep. Hence, these results based on deformation theory are as rigorous as

results based on flow theory (Budiansky 1959). However, if the loading history includes load reversal, one would need to use an approach based on flow theory.

Analogous to Chapter 2, these results for free sliding give the most severe singularities for the same geometry and creep law.

The accommodation mechanism has been assumed to be purely power-law creep. However, at the focus of the stress singularity where stresses are very high, other processes like diffusion and time independent plasticity ($m \to \infty$) may locally become the more powerful accommodation mechanisms. Yet within the temperature range and nominal stress range where power-law creep is the dominant deformation mode, such diffusion and plasticity mechanisms cannot operate competitively in the entire domain. These mechanisms of diffusion and plasticity, if present, dominate only in a very short range localized at the focus of the stress singularity. Their effect is to moderate and alter the stress state and eliminate the singularity as has been discussed by Argon, Chen and Lau (1980, 1981). The power law creep solutions presented in this chapter then furnish the governing boundary conditions to this very localized inner moderation zone.

The singular stresses have been determined to within the multiplicative constant K of Eq. 2.5. This scale factor of the asymptotic singular stresses is the analog of the stress intensity factor in elastic and plastic fracture mechanics. It contains information about the remote boundary conditions, the geometry and the constitutive relationship. This creep stress intensity factor must be determined by an appropriate global analysis, usually numerical for such complex conditions, to connect the remote field and the local asymptotic singular field. However, one has to use a global analysis which is capable of solving the local singular field in great detail. Since there is no traction free interfaces connecting the local (near) field and the remote (far) field, K cannot be determined by the conventional approach of a path independent contour integral. Therefore, one has to determine K from the global solution at the immediate vicinity of the singularity.

CHAPTER FOUR

FINITE ELEMENT SOLUTIONS

4.1 Introduction

The dominant singular stress distributions caused by grain boundary sliding accommodated by power law-creep are now available for two geometric configurations of interest in the creep fracture of engineering alloys. These solutions have been computed for: (A) the apexes of hard particles embedded in sliding grain boundaries under a remote shear stress parallel to the sliding grain boundaries, and (B) at triple grain junctions under a remote tensile stress perpendicular to one of the three converging grain boundaries (see Chapter 3). These local asymptotic solutions, in analogy to asymptotic stress solutions of cracks in elastic (Williams 1957) and plastic continuua (Hutchinson 1968; Rice and Rosengren 1968), are each determinable to within a multiplicative constant, K, which has been defined in Eq. 2.5. In this thesis, K will be referred to as the creep stress intensity factor. This creep stress intensity factor needs to be obtained by an appropriate global analysis to connect the remote loading to the local asymptotic singular field.

The finite element method (Zienkiewicz 1978;

Bathe 1981) has been proven to be a very versatile numerical technique in computational stress analysis, especially in problems involving nonlinear behavior, complicated geometries, and complex boundary conditions. Gallagher (1972, 1978) has reviewed the wide spread application of finite element method in elastic and elasto-plastic fracture mechanics. Benzley and Parks (1974) has surveyed the fracture mechanics computer programs being used. Swedlow (1978a) has reported on special finite element procedures used for the crack tip and for singularity computations in general (Swedlow 1978b). Pian (1975) has evaluated different crack elements used in linear and nonlinear computations involving stress singularities.

In this chapter, a specially developed finite element algorithm is used to solve for the plane strain creep stress intensity factors related to the hard particles and the triple grain junctions. This finite element analysis utilizes specially formulated power-type singularity elements, a novel method to deal with periodicity and symmetry boundary conditions by kinematic modelling and a self adaptive scheme for automatic adjustment of step size for stable time integration.

4.2 Method of Solution

The creep behavior is obtained by incremental approach. This method first computes the elastic solution of the problem. It then computes the creep strains, based on the latest available stress distribution, for a small time increment. These creep strains are then treated as initial strains to solve for the new stress distribution at the end of the time increment. The procedure is repeated until a prescribed time is reached. This prescribed time is usually chosen to correspond to steady state at which the stress distribution does not change with time. Details of incremental, initial strain finite element formulation using Euler's method for forward marching, explicit time integration can be found in Zienkiewicz and Cormeau (1974), Snyder (1981) and Bathe (1981).

4.2.1 Elasto-power-law creep constitutive equations

In this plane strain finite element analysis, the grain matrix is modelled to deform according to Hookean elasticity and multi-axial power-law creep. If the deformation were uniaxial, the constitutive relationship in terms of the elastic strain increment, $\Delta\varepsilon^E$; the creep strain increment, $\Delta\varepsilon^C$; the total strain increment,

$\Delta\varepsilon$; the Young's modulus, E; the tensile stress, σ; the creep constants A and m, and time t would have been

$$\Delta\varepsilon = \Delta\varepsilon^{E} + \Delta\varepsilon^{C} \tag{4.1a}$$

$$\Delta\varepsilon^{C} = \int_{0}^{t} A\,\sigma^{m}\,dt \tag{4.1b}$$

$$\Delta\varepsilon^{E} = \frac{\Delta\sigma}{E} \tag{4.1c}$$

Assuming isotropy, creep incompressibility, the existence of a creep potential, and independence of creep resistance on hydrostatic stresses (Odqvist 1974), Eq. 4.1 governing the grain matrix is generalized to multiaxial elasto-power law-creep as follows:

$$\Delta\varepsilon_{ij} = \Delta\varepsilon_{ij}^{E} + \Delta\varepsilon_{ij}^{C} \tag{4.2}$$

$$\Delta\varepsilon_{kk} = \frac{1-2\nu}{E}\sigma_{kk} = \Delta\varepsilon_{kk}^{E} \tag{4.3a}$$

$$e_{ij} = \varepsilon_{ij} - \frac{1}{3}\varepsilon_{kk}\delta_{ij} \tag{4.3b}$$

$$\Delta e_{ij}^{E} = \frac{2(1+\nu)}{E}\Delta S_{ij} \tag{4.3c}$$

$$\Delta e_{ij}^{c} = \int_{o}^{t} \frac{3}{2} A \sigma_e^{m-1} S_{ij} \, dt$$
$$= \Delta \varepsilon_{ij}^{c} \qquad (4.3d)$$

where E and ν are Young's modulus and Poisson's ratio respectively, σ_{kk} is hydrostatic tension, ε_{kk} is volumetric strain, e_{ij} is deviatoric strain defined by Eq. 4.3b, S_{ij}, σ_e, A and m have been defined in Eqs. 3.1 - 3.2.

4.2.2 Self-adjusting time step incrementation

The equilibrium equation governing the displacement increments, $\Delta\underline{u}$, from time = t to time = t+Δt for our initial strain finite element formulation is

$$\underline{K}\,\Delta\underline{u} = {}^{t+\Delta t}\underline{F} - {}^{t}\underline{F} + {}^{\Delta t}\underline{F}^{c} \qquad (4.4)$$

where ${}^{t+\Delta t}\underline{F}$ is a force vector due to the applied load boundary condition at time = t+Δt, ${}^{t}\underline{F}$ is the force vector due to the internal stress distribution which is in equilibrium with the applied load at time t, ${}^{\Delta t}\underline{F}^{C}$ is the equivalent creep force in the time interval Δt due to creep strain treated as an initial strain at t. In addition $\Delta\underline{u}$ is the yet to be determined displacement increment in Δt, and $\underline{K}$ is the elastic stiffness matrix

which needs only to be assembled and decomposed once and stored in high speed storage to be used in all subsequent steps.

With Euler's forward marching time integration, the creep force is

$$ {}^{\Delta t}\underline{F}^{C} = \sum_{\text{element}} \int_{Vol} \underline{B}^{T}\, \underline{c}\, \underline{\dot{\varepsilon}}^{C}({}^{t}S_{ij})\, \Delta t \, dVol \qquad (4.5) $$

where $\underline{B}$ is the strain-displacement matrix ($\underline{\Delta\varepsilon}=\underline{B}\Delta u$), $\underline{c}$ is the Hookean matrix of elastic constants ($\underline{\Delta\sigma}=c\underline{\Delta\varepsilon}^{E}$), $\underline{\dot{\varepsilon}}^{C}({}^{t}S_{ij})$ is the creep strain rate matrix based on the deviatoric stresses at t (see, for example, Snyder 1981; Bathe 1981).

The time increment, Δt, needs to be chosen with great care. The Euler forward marching method is a conditionally stable scheme. When Δt is larger than a critical value, there is frequently numerical instability in the time evolution of the solution. This usually manifests itself in violently oscillating results. If allowed to propagate, the instability can grow quickly to terminate the computation by overflow or underflow.

Although the search for a method to determine the optimal time step Δt has long attracted keen interest,

the traditional strategies of selection of Δt are mainly empirical in nature. "Rule-of-thumb" strategies of selecting Δt such that in each step the effective creep strain increment is less than some arbitrary fraction (typically 1% to 15%) of the accumulated total strain (Levy and Pifko 1981; Zienkiewicz and Cormeau 1974), or that the new Δt is not more than an arbitrary fraction (typically 150%) of the immediately preceeding Δt (Zienkiewicz and Cormeau 1974), are frequently used. Their use, however, cannot always ensure numerical stability.

In our finite element computations, Δt is automatically self adapted according to the latest available largest equivalent stress of all the spatial integration points, $(\sigma_e)_{max}$, by

$$\Delta t = f \cdot \frac{2}{3}(1+\nu)\frac{1}{m}\frac{1}{EA(\sigma_e)_{max}^{m-1}} \tag{4.6}$$

where f is an adjustable parameter that can be prescribed to have different values for each time step.

If f is set equal to 2, Eq. 4.6 becomes the limiting case of

$$\Delta t \leq \frac{4(1+\nu)}{3}\frac{1}{m}\frac{1}{EA(\sigma_e)_{max}^{m-1}} \tag{4.7}$$

which is a stability criterion developed by Cormeau (1975) for the type of explicit time integrating, initial strain, incremental finite element algorithm that we are using. This criterion is derived from applying classical stability requirements (Lambert 1973; Gear 1971) to the upperbound estimate of the largest eigenvalue of the Jacobian matrix of the system of linearlized ordinary differential equations that govern the stresses at each spatial integration point. Irons and Treharne (1971) have developed a similar criterion. Equation 4.7, which is based on the linearized system of differential equations rather than the original nonlinear ones, has been found to be conservative for some boundary value problems by Bassani and McClintock (1981).

In our computations, f has been varied from larger than 2 (for quick approach to steady state) to smaller than 2 (for better accuracy). Its effect on the time evolution of the solution will be reported in Sections 4.3 and 4.4.

4.2.3 The power-type singularity element

The displacement interpolation functions of conventional finite elements are constructed so that the elements can simulate rigid motion, linear displace-

ment (or constant strain), and, for some elements, increasingly higher order terms. They are thus equipped to simulate the nonsingular portion of the series solution in continuum mechanics. They cannot, however, give an exact representation to the other portion of a series solution which involves a singularity in strain and stress (Williams 1952, 1957, 1961), even if the geometry and boundary conditions dictate that such a singularity should exist in the field solution. When a singularity exists, using substantial mesh refinement of these conventional elements improves the numerical solution, but the convergence to a final solution is slow (Tong and Pian 1972). Very large numbers of conventional elements are usually required to provide a solution that yields stress intensity factors of reasonable accuracy (5 - 10%) for simple crack problems in linear elastic analysis (Chan et al. 1970; Kobayashi et al. 1969). On the other hand, using elements that contain the actual type of the singular behavior at the crack tips lead to increased accuracy of the near tip solutions with fewer elements, and produce accurate estimation of stress intensity factors by methods that depend on the near tip fields for solution (Henshall and Shaw 1975; Tong, Pian and Lasry 1973; Hilton and Hutchinson 1969; Barsoum 1977;

Gallagher 1972, 1978). Tracey and Cook (1977) have developed a power-type singularity element which they have used to analyse cracks in an elastic bimaterial, and branch crack in elastic material. The displacement shape functions of their element are such that the element is able to represent both constant displacement and a displacement varying as r^q in the radial direction, and represent both constant and linear displacements in the circumferential direction. This element is therefore not compatible with the quadratic isoparametric element which is versatile and the "work horse" of most displacement based finite element programs. Also, lacking a linear displacement term in the radial direction, this singularity element does not satisfy the constant first derivative requirement of the element convergence criterion (Zienkiewicz 1977). Lacking such a term prevents this element from modelling radial constant strain (and hence constant stress) behavior. Therefore, its radial dimension must be kept very small so that the exclusion of this behavior from its domain is inconsequential. These drawbacks can be rectified by redeveloping Tracey and Cook's special element to add the radial linear displacement term and a quadratic circumferential displacement term. The new element is a four node C^0-continuity element (Fig. 4.1a). Its dis-

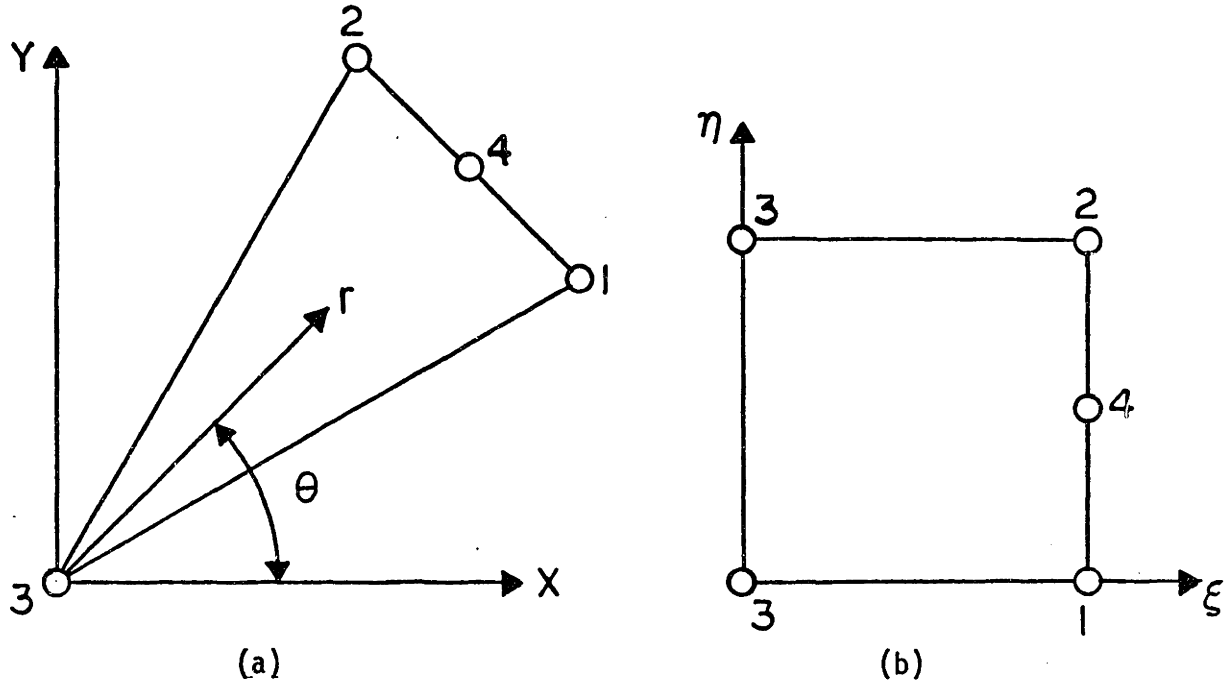

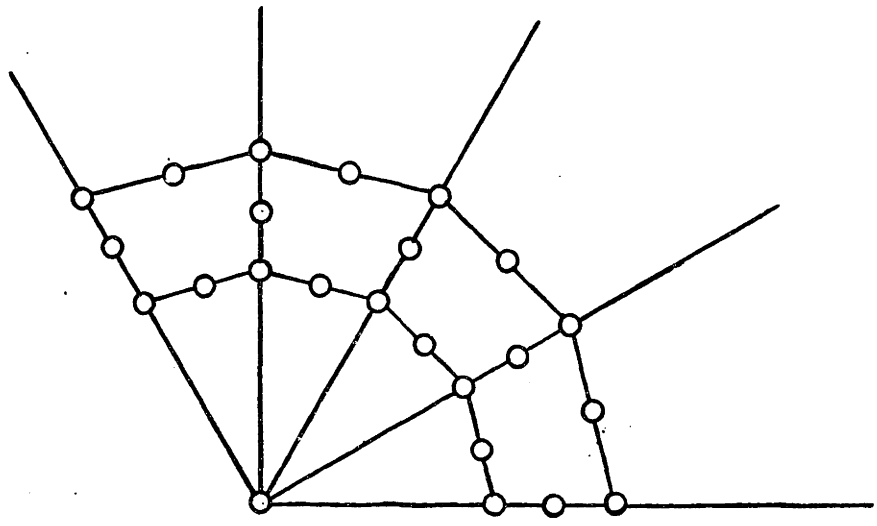

(c)

Figure 4.1 Special Element in (a) Physical Space, (b) Natural Space and (c) Application.

placement interpolation functions are different from its coordinate mapping functions, while its coordinate mapping functions are identical to those of the serendipity isoparametric element. For an element mapping into a unit square of $0 \leq \xi \leq 1$ and $0 \leq \eta \leq 1$ in the natural space (ξ,η), Fig. 4.1b, these special displacement interpolation functions that give rise to the power-type distribution in strain ($\varepsilon \sim r^{q-1}$), are:

$$N_1 = \frac{\xi + \alpha\xi^q}{1+\alpha}(1-2\eta)(1-\eta) \tag{4.8a}$$

$$N_2 = \frac{\xi + \alpha\xi^q}{1+\alpha}(-1+2\eta)\eta \tag{4.8b}$$

$$N_3 = 1 - \frac{\xi + \alpha\xi^q}{1+\alpha} \tag{4.8c}$$

$$N_4 = 4\frac{\xi + \alpha\xi^q}{1+\alpha}(\eta - \eta^2) \tag{4.8d}$$

When the parameter q takes the value of 1, or when the parameter α takes the value of 0 this special element is reduced to a standard 5-node isoparametric element with the two corner nodes of the side opposite to the 3-node side collapsed into one physical node. Details of the special element can be found in Appendix B.

In the radial direction in the physical space,

this special element is capable of representing constant displacement, constant strain and power-type singular strain. Thus it covers not just the most dominant local stress singularity but also the constant stress term in the field solution. In the circumferential direction, it can represent constant displacement, constant strain and linear strain. It is compatible with adjoining serendipity 8-node isoparameter elements.

When applied to solve for the creep stress intensity factors for the hard particle or the triple grain junction, a fan-shaped array of these isosceles-triangular special elements, with their singularity nodes at the origin of the strain singularity, is connected to a surrounding mesh of 8-node isoparametric elements (Fig. 4.1c). Special quadratures have been developed to integrate the stiffness matrix, equivalent force vector and equivalent creep force vector of the special elements (Appendix B). A 2x2 Gauss-Legendre quadrature is used for the 8-node isoparametric elements.

4.2.4 Kinematic modelling of boundary conditions

Symmetry and periodicity (repetition in space) can simplify the statement of a boundary value problem. However, they frequently give rise to boundary conditions

that are outside the available conventional boundary condition models of common general purpose finite element programs. Special algorithms have been developed for linear multipoint constraints on displacement (Abel and Shephard 1978; Curiskis and Valliappan 1978). Constraints on stresses in nonlinear material are more difficult to deal with. Considerable formulation and programming efforts are required even for a special purpose program (Ghahremani 1980). In small strain finite element analysis, kinematic modelling can be used to readily obtain the desired constrained boundary conditions on displacements and stresses, without special formulation or programming.

For example, Fig. 4.2a shows an arrangement consisting of three bars connected to a freely rotating beam. Equilibrium at the midpoint, E, of the beam dictates that the normal force at A, $(F_n)_A$, must be equal to the normal force at B, $(F_n)_B$. Also, if the material of the bars AF, CE, BG is rigid compared to the material of RACBT, then the normal displacements at A and B, $(U_n)_A$ and $(U_n)_B$ respectively, are anti-symmetric about C. Since the analysis is for small strain and the bars are perpendicular to ACB, the shear force, F_s, is zero at nodes A, C, and B.

The beam can be modelled by a 3-node beam

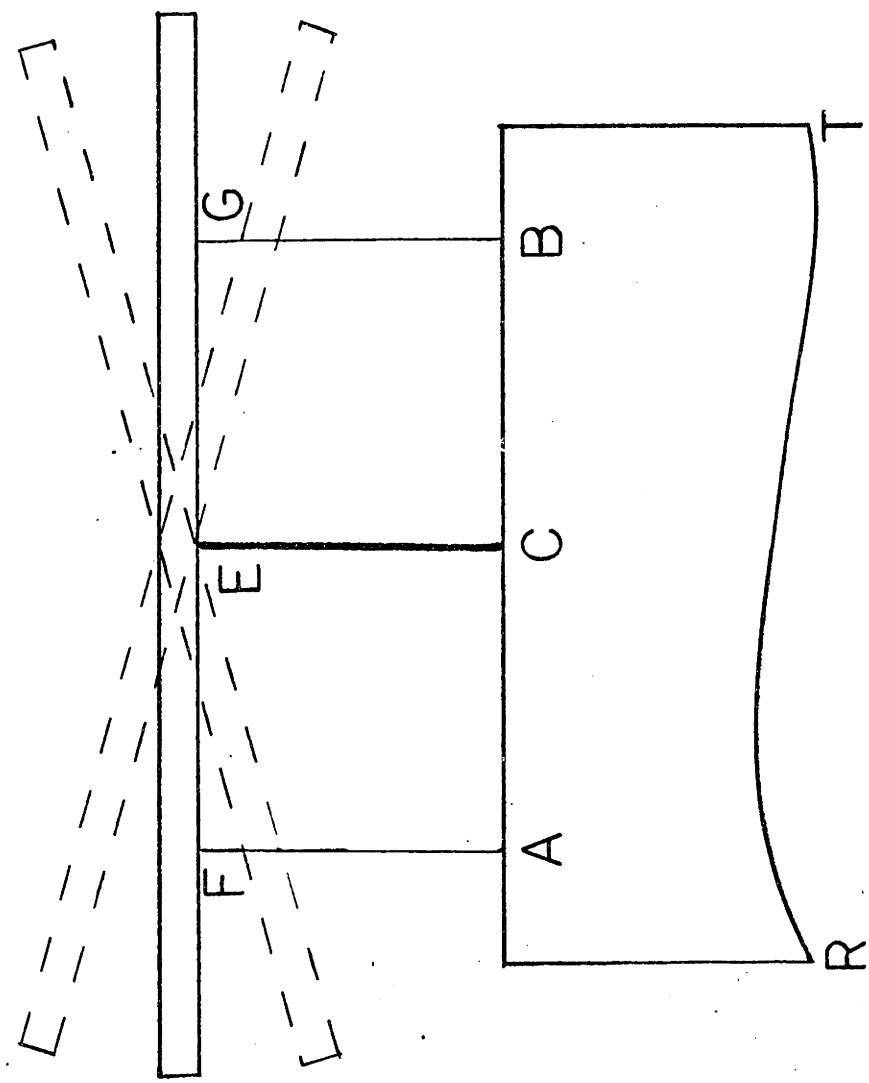

Figure 4.2a Kinematic Arrangements for Boundary Conditions on ACB.

element, or equally well, by a conventional two-dimensional element with high Young's modulus. We use a five node isoparametric element to model it. Other combinations of any available two-dimensional elements giving rise to the required three nodes on line FEG can be used.

When several units of these arrangements, are used, staggering one on top of the other, with node E in common, as is shown schematically in Fig. 4.2.b, the condition of $\sigma_s = 0$, σ_n symmetric about C and U_n antisymmetric about C on boundary ACB can be simulated. This concept is applied to model that part of the boundary conditions which arises from symmetry and geometric repetition in the triple grain junction problem (Fig. 4.4).

A different kinematic arrangement is shown in Fig. 4.3. Here several bars, AF, BG, CH, DI and EJ, having high axial but very low bending stiffnesses and vanishingly small length, connect the boundary ABCDE to the surface of a rigid but freely rotating plate KFGHIJL. The bars are perpendicular to ABCDE. The plate can rotate freely about a pivot L which is physically located at the intersection of lines PA and NE. The bars and the plate are designated with much higher modulus than AENOP. In

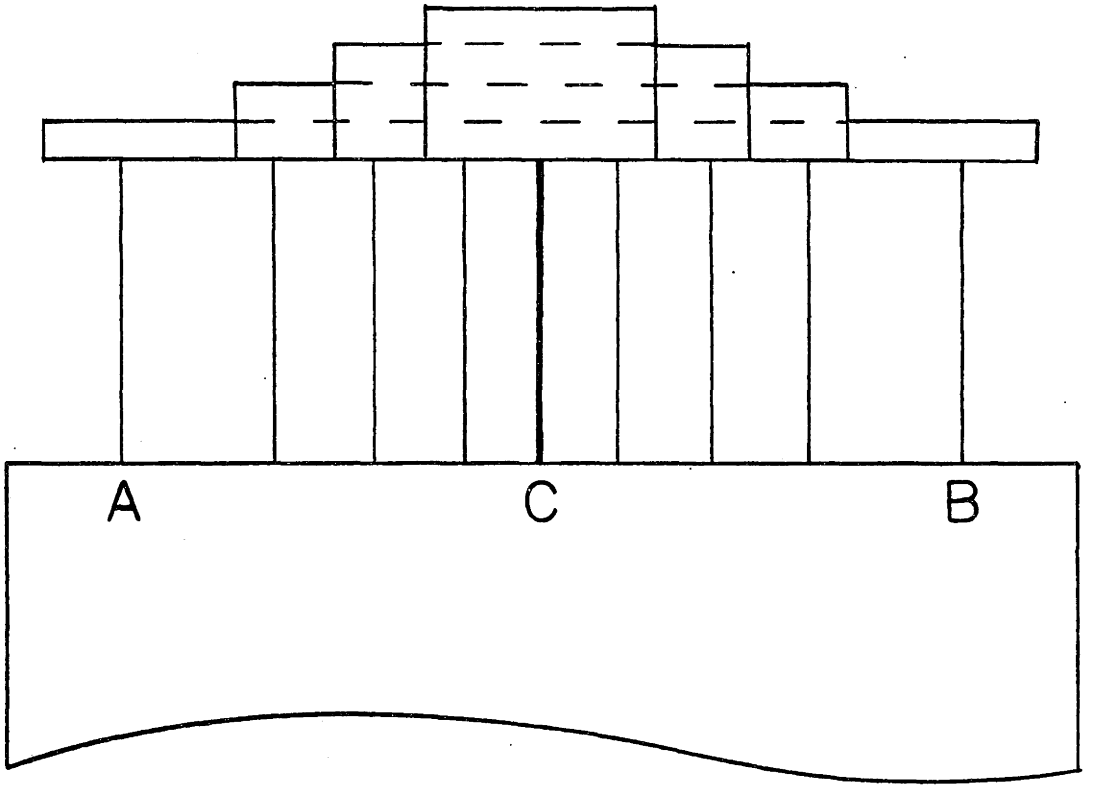

Figure 4.2b Kinematic Boundary Model for $\sigma_s = 0$, σ_n Symmetric about C and U_n Antisymmetric about C on ACB.

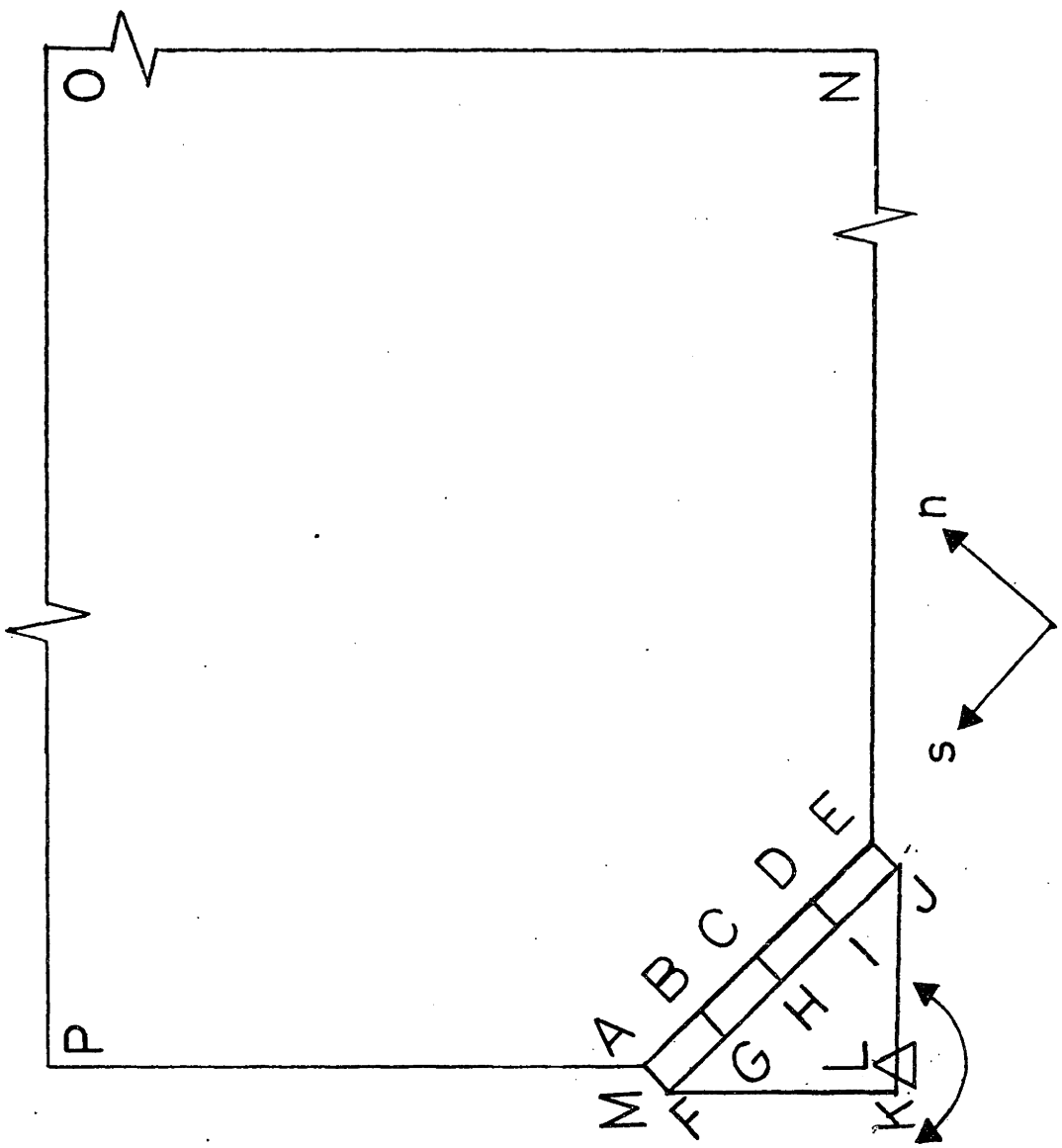

Figure 4.3: Kinematic Boundary Condition Model for Free Sliding on the Surface of a Hard Particle that can Rotate.

small strain analysis, this kinematic arrangement simulates the condition that boundary ABCDE slides freely on the surface of a rigid particle which can rotate, i.e., on boundary ABCDE, $\sigma_s = 0$ and U_n has the same magnitude as the U_n on FGHIJ of the rigid particle.

One high order two dimensional element can model the rotating rigid plate. Alternatively, a combination of several low order two dimensional elements can simulate the rotating rigid plate equally well. Such an arrangement is used to model the interface boundary between the grain matrix and the hard particle in Section 4.3.

The method of kinematic modelling of boundary conditions has also been applied in a recent study of stress redistribution in a creeping continuum with a rigid or an elastic inclusion by McClintock (1981), producing good results.

4.2.5 Incompressibility constraint in FEM

In finite element analysis, except where the components of the stress tensor corresponding to a particular direction can be assumed zero a priori (such as in plane stress analysis), incompressibility imposes constraints that require special treatement (Fried 1973 ; Nagtegaal, Parks and Rice 1974; Argyris, Dunne,

Angelopoulos, and Bichat 1974). Since Herrman's (1965) pioneering work, several special finite element approaches have been reported to be effective in various cases involving incompressibility. There are four major categories of approaches: (A) Apply reduced/selective integration to displacement based finite element formulation (Naylor 1974; Zienkiewicz 1977; Malkus and Hughes 1977; Hughes 1980); (B) Incorporate the incompressibility constraint into the variational equation governing equilibrium by the Lagrange multiplier or the penalty function method (Herrman 1965; Oden 1968; Key 1969; Nagtegaal, Parks, and Rice 1974; Hughes, Liu and Brooks 1979; Bercovier and Engelman 1979; Bercovier, Hasbani, Gilon and Bathe 1980); (C) Use special elements in which the kinematically admissible displacement fields are intrinsically incompressible (Needleman and Shih 1978); and (D) Use an assumed stress hybrid finite element formulation (Tong 1969; Pian and Lee 1976). The last word in this research area is far from said. Investigators are currently in hot pursuit to further study and to develop a general finite element program for incompressible behavior (Bathe 1981).

In our computations, the effect of the incompressibility constraint is felt when the accumulated

creep strains dominate over the elastic strains. The finite element solution produces stresses that deviate from the field solution of Chapter 3 by an oscillatory hydrostatic component. Using 2x2, or 1x1 Gauss-Legendre quadrature for the special element (instead of the special quadrature rule of Appendix B) does not alleviate this problem. All 8-node isoparametric elements have been treated by reduced integration by 2x2 Gauss-Legrendre quadrature. On the other hand, plots of the angular distribution of the effective stress and the deviatoric stresses agree well with the field solution of Chapter 3.

It has been reported that over constraint can cause the finite element mesh to "lock" to produce erroneous displacement solutions (Nagtegaal, Parks and Rice 1974; Tsach 1981). However, our incremental initial strain finite element results indicate that the incompressibility constraint apparently does not cause a general locking of the mesh to produce a randomly erroneous displacement. Instead, it causes a peculiar locking of the mesh to produce a displacement field that deviates from the correct solution in a particular way: only the volumetric strain derived from this displacement is in error, while the deviatoric strains are given correctly. Therefore, the total stresses are subject to error but

the deviatoric stresses are not. This has also been encountered by Naylor (1974) who has reported that oscillatory error exists only in hydrostatic pressure, but not in deviatoric stresses in his iterative tangent stiffness finite element analysis of an elastic-plastic sphere under internal pressure.

This characteristic of our solution enables the creep stress intensity factors to be determined, free from the effect of incompressibility, from the distribution of the equivalent stress σ_e, the shear stress $\sigma_{r\theta}$ or any other deviatoric stress quantities:

$$\sigma_e = K r^{\lambda} \hat{\sigma}_e \qquad (4.9a)$$

$$\sigma_{r\theta} = K r^{\lambda} \hat{\sigma}_{r\theta} \qquad (4.9b)$$

and

$$S_{ij} = K r^{\lambda} \hat{S}_{ij} \qquad (4.9c)$$

4.3 FEM Solution for the Hard Particle

Figure 4.4 defines the geometry and boundary conditions for the hard particle on the grain boundary. Figure 4.5 shows the finite element mesh in which the special singular element of Section 4.2.3 is used in conjunction with 8-node isoparametric elements. The

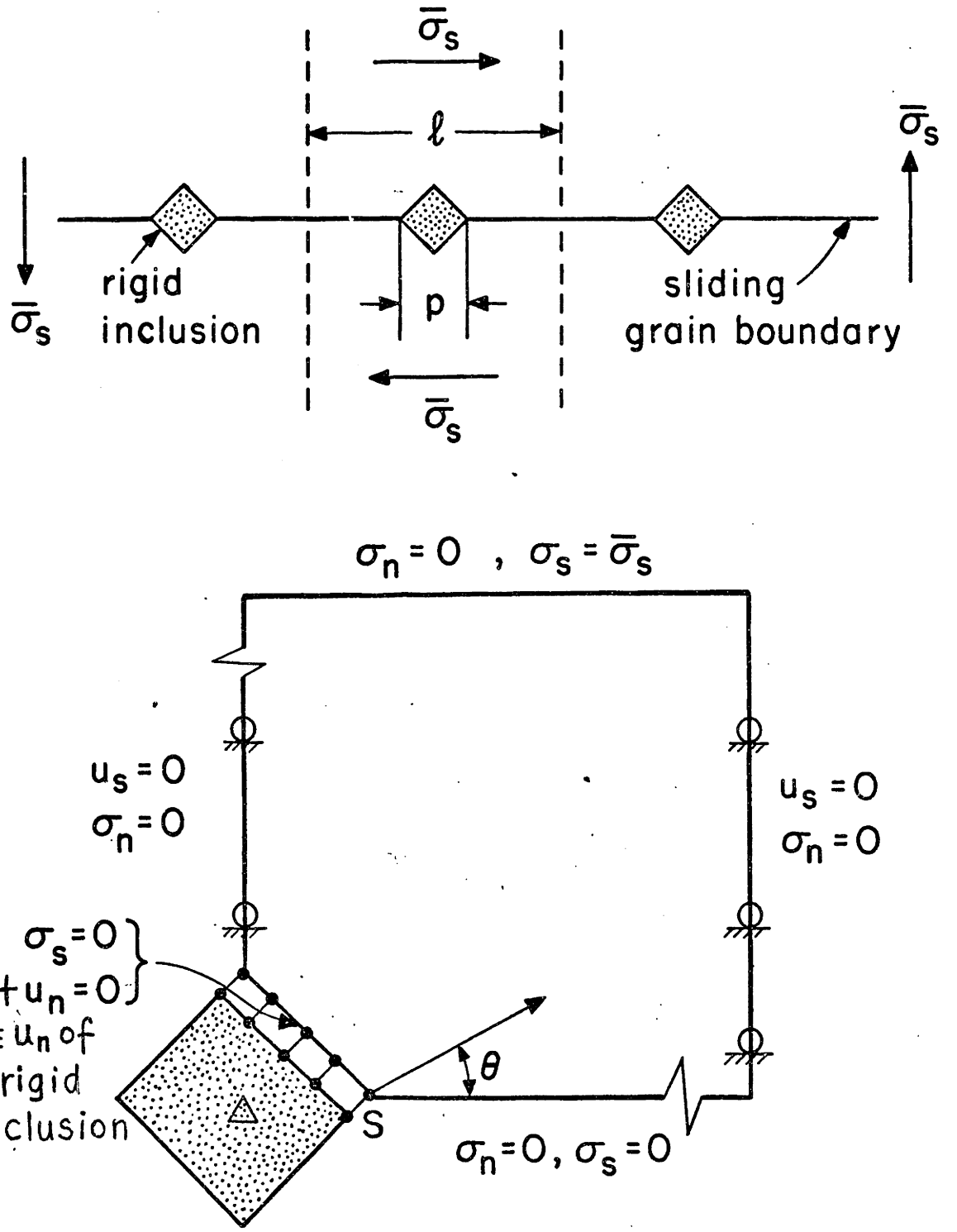

Figure 4.4 Definition of Problem on Stress Concentration Around Grain-Boundary Particles: Statement of the FEM Problem.

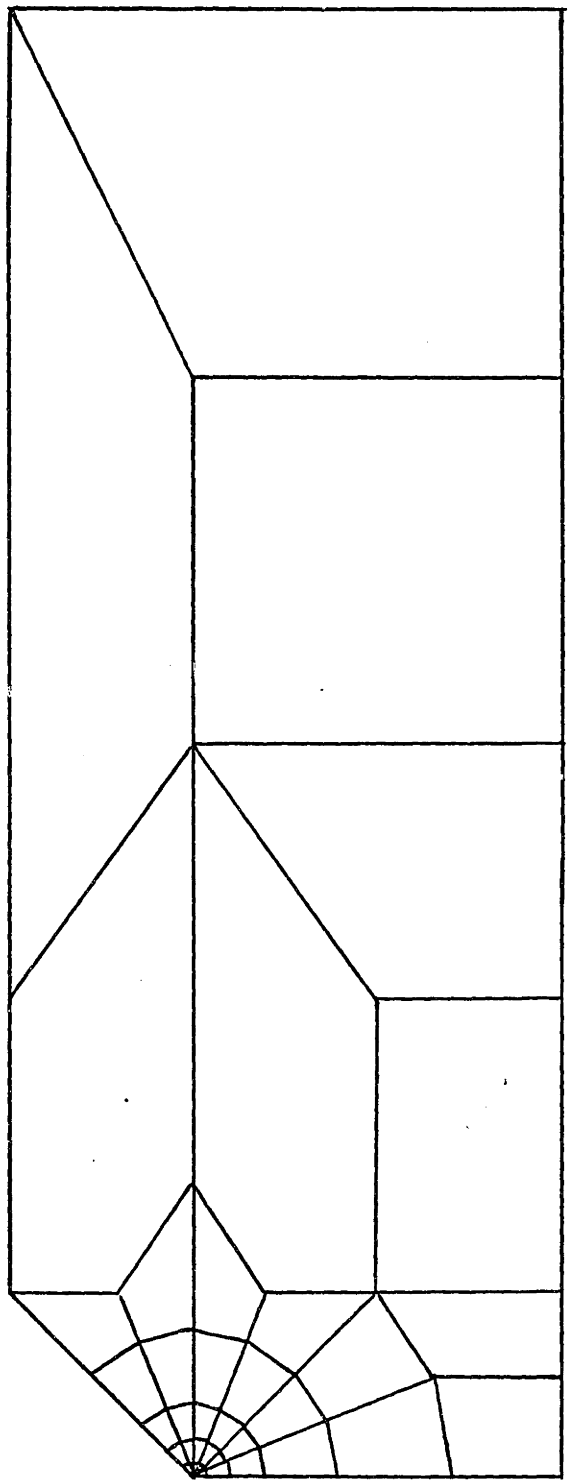

Figure 4.5 Finite Element Mesh for the Hard Particle Problem.

mesh shown is for ℓ/p of 3.0, but is readily extensible to other ℓ/p (say, $\ell/p = 10.0$). Chen and Argon (1981) have recently reported on creep cavitation in 304 stainless steel in which the observed average ℓ/p ratio was 3.5.

At time, $t = 0$, a far field shear stress $\sigma_s = 10^{-3}E$ is applied and kept constant. Finite element solutions are obtained for $m = 3$ and 5. For each m, a convenient set of values are assigned to E, ν and A of Eqs. 4.2 - 4.3. The actual values of E, ν and A do not enter the final steady state creep stress solution. They may be regarded as mere vehicles to be used to reach the final stress solution.

Figure 4.6 shows the comparison of the finite element results for the θ-variation of the deviatoric stresses, $\hat{S}_{ij}$, with the dominant singular solution of Chapter 3. The discrete points are finite element results of $r^{\lambda}S_{ij}$ $(=K\,\hat{S}_{ij})$ divided by a scaling constant, h. This scaling constant h is determined from requiring one particular point of the FEM result, that of $r\sigma_e/h(=\hat{\sigma}_e K/h)$ at $\theta = 62.8°$, to have the same value as $\hat{\sigma}_e(62.8°)$ of the dominant singular solution. By just "attaching" this one point of the FEM solution to the singular solution, it is observed that all other

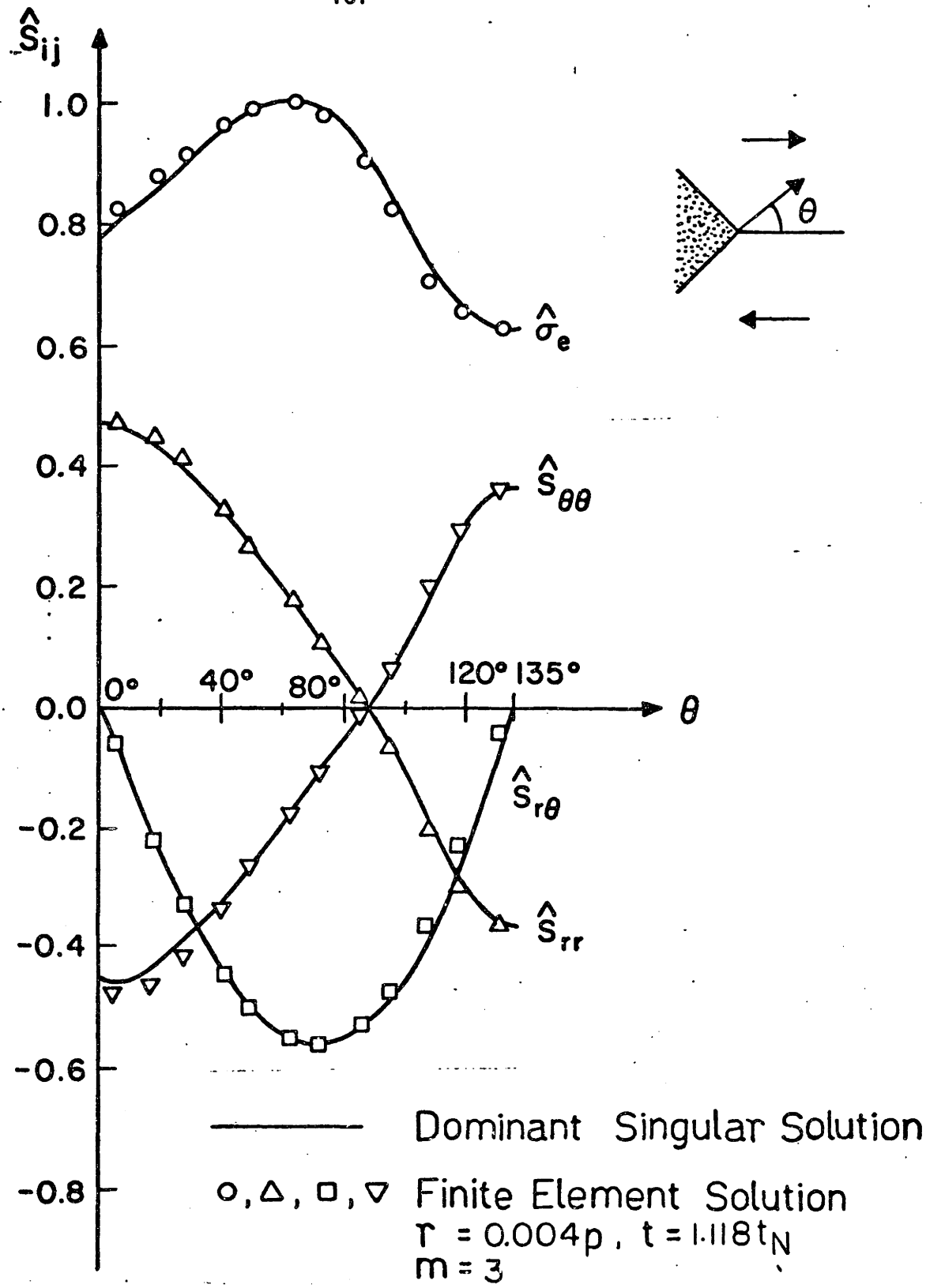

Figure 4.6 FEM Solution at the Apex of a Hard Particle of $\omega = \pi/4$ $m = 3$, $r = 0.004p$, $t = 1.118t_N$.

points of the FEM solution fall on the solid lines representing the dominant singular solution. This indicates that the sampling points of these finite element results are within the dominant singularity zone, and these finite element results indeed obey

$$\sigma_e = K r^{\lambda} \hat{\sigma}_e \tag{4.10a}$$

and

$$S_{ij} = K r^{\lambda} \hat{S}_{ij} \tag{4.10b}$$

Then K is given by the value of h.

At the sampling time of $t = 1.118\ t_N$, where t_N is the time for the nominal creep strain to become equal to the nominal elastic strain ($t_N = [\varepsilon^E(\sigma_s)]/[\dot{\varepsilon}^C(\sigma_s)] = 1/(EA\sigma_s^{m-1})$, the accumulated creep strain at the stress sampling points at r = 0.004p are at least 900% of the elastic strains.

The scaling of the $r^{\lambda}\sigma_e (=K\hat{\sigma}_e)$ at $\theta = 62.8°$ by h determines K. Since the FEM results agree with the singularity solution very well in all components of $\hat{S}_{ij}$ and at all θ, K can be determined from any component of S_{ij} at any θ. We determine K from σ_e at a θ value where σ_e is close to maximum. For m = 3, as determined from r = 0.004p at $t = 1.118t_N$,

$Kp^{\lambda}/\sigma_s = 0.965$.

Figure 4.7 shows the corresponding distributions for m = 5, at $t = 1.923t_N$. Similarly good agreement between the FEM and the singular solutions is obtained for all components of $\hat{S}_{ij}$. The value of $\frac{kp^{\lambda}}{\sigma_s}$ determined from this data is 1.109. Figures 4.7 to 4.13 show the variation of $\hat{S}_{ij}$ of the FEM solution (for m = 5) as a function of distance, r/p, from the origin of the singularity. It is observed that $\hat{S}_{ij}$ starts to deviate appreciably from the singular solution for $r \geq 0.177p$. For $r < 0.177p$, K values determined from $\hat{S}_{ij}$, especially those from $\hat{\sigma}_e$ and $\hat{s}_{r_\theta}$ at $\theta \sim \pi/3$ are trustworthy. At $\theta \sim \pi/3$, $\hat{\sigma}_e$ and $\hat{S}_{r_\theta}$ obtain their maximum value, and will, therefore, give the least error in the K determination. Figure 4.14 shows the value of kp^{λ}/σ_s as a function of r/p. It is apparent from Fig. 4.14 and Figs. 4.7 and 4.13 that even though the $\hat{S}_{ij}$ computed by FEM may deviate from the singular solution at some θ, $\hat{\sigma}_e$ at $\theta \sim \pi/3$ is seldom influenced by such local deviation. Thus, $\frac{kp^{\lambda}}{\sigma_s}$ determined from $\hat{\sigma}_e$ at $\theta = 62.8°$ is valid for a surprisingly long range (large r/p), as is evident from Fig. 4.14.

Figures 4.15 to 4.23 demonstrate the gradual

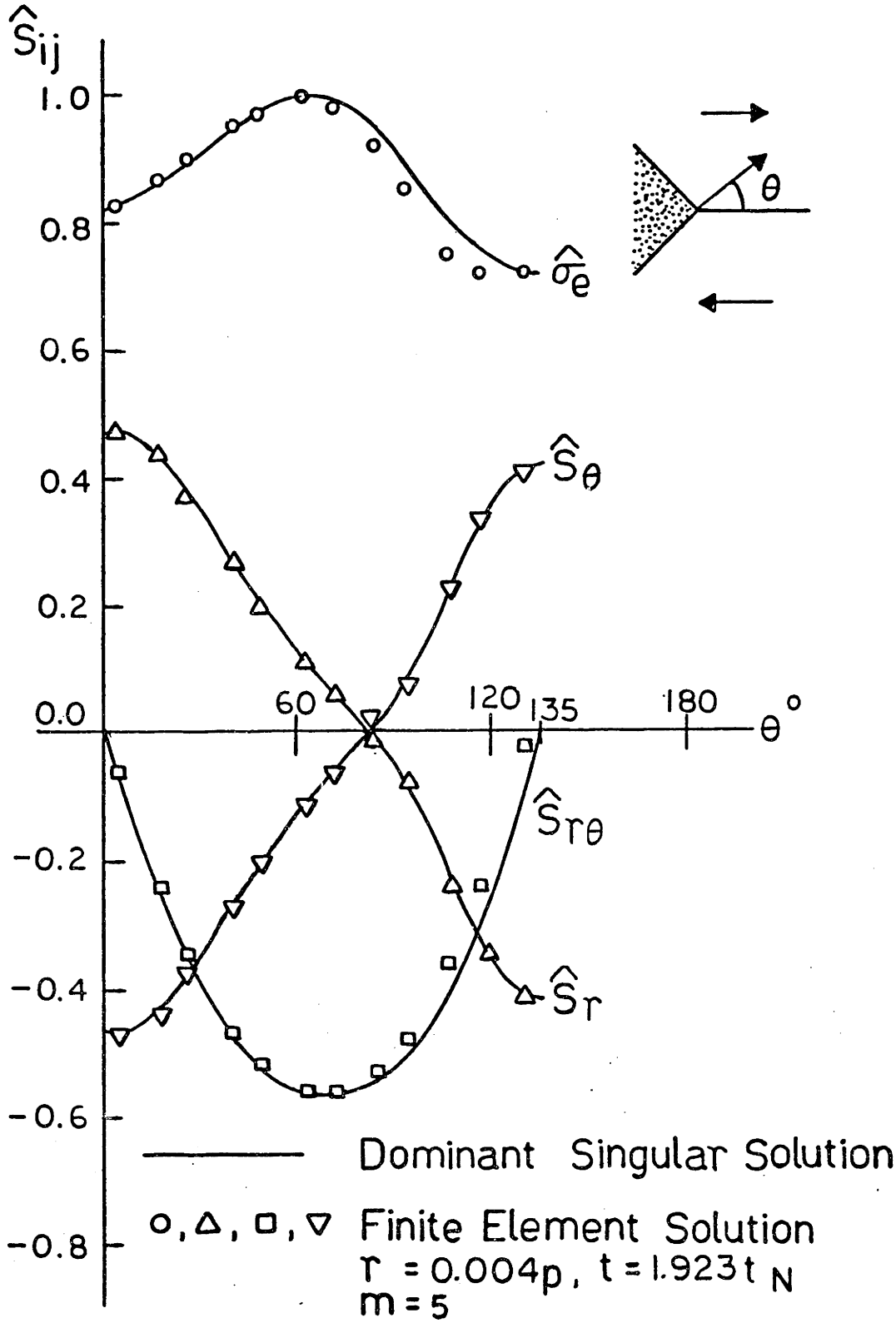

Figure 4.7 FEM Solution at the Apex of a Hard Particle of $\omega = \pi/4$, $m = 5$, $r = 0.004p$, $t = 1.923t_N$.

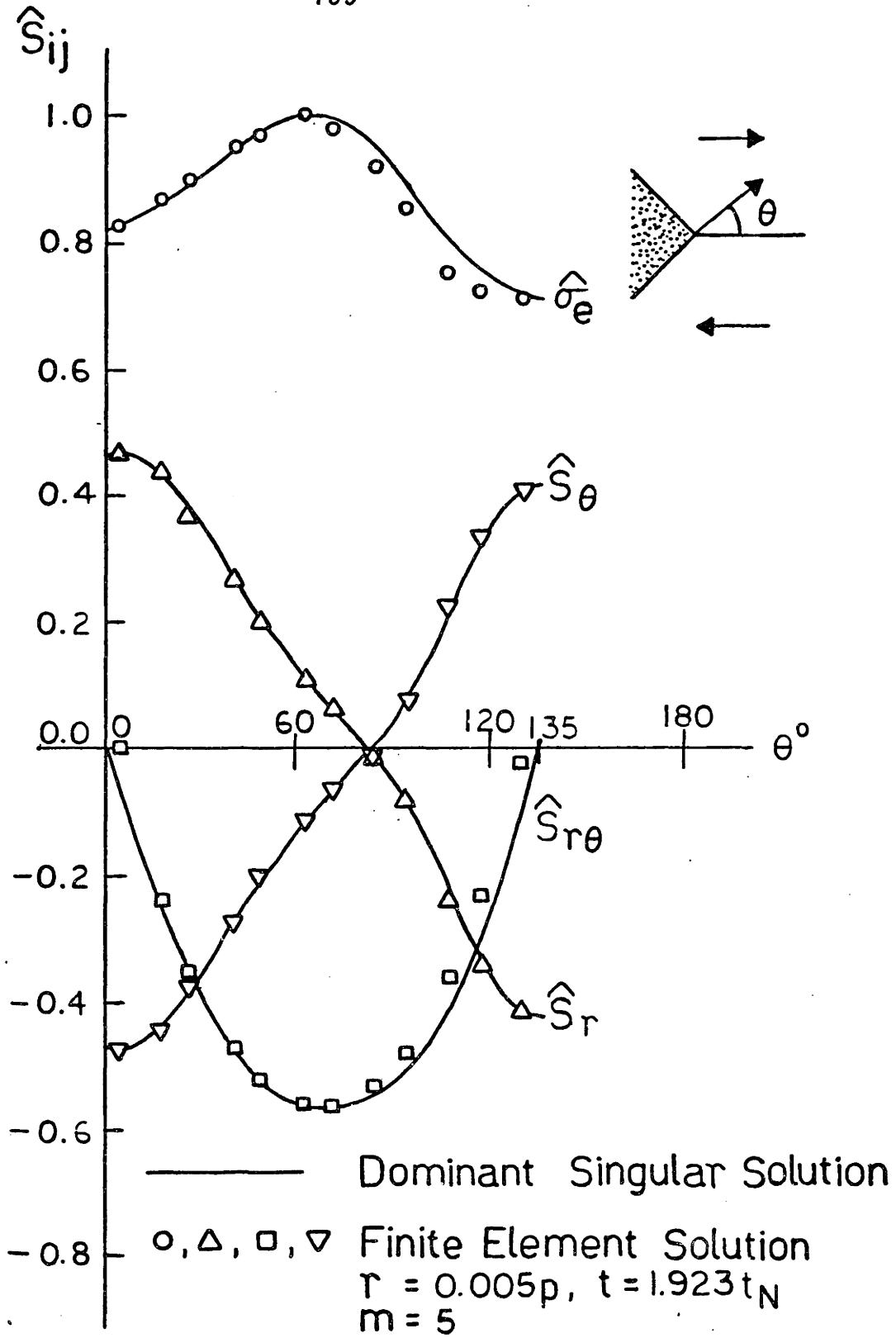

Figure 4.8 FEM Solution at the Apex of a Hard Particle of $\omega = \pi/4$, m = 5, r = 0.005p, t = 1.923t_N.

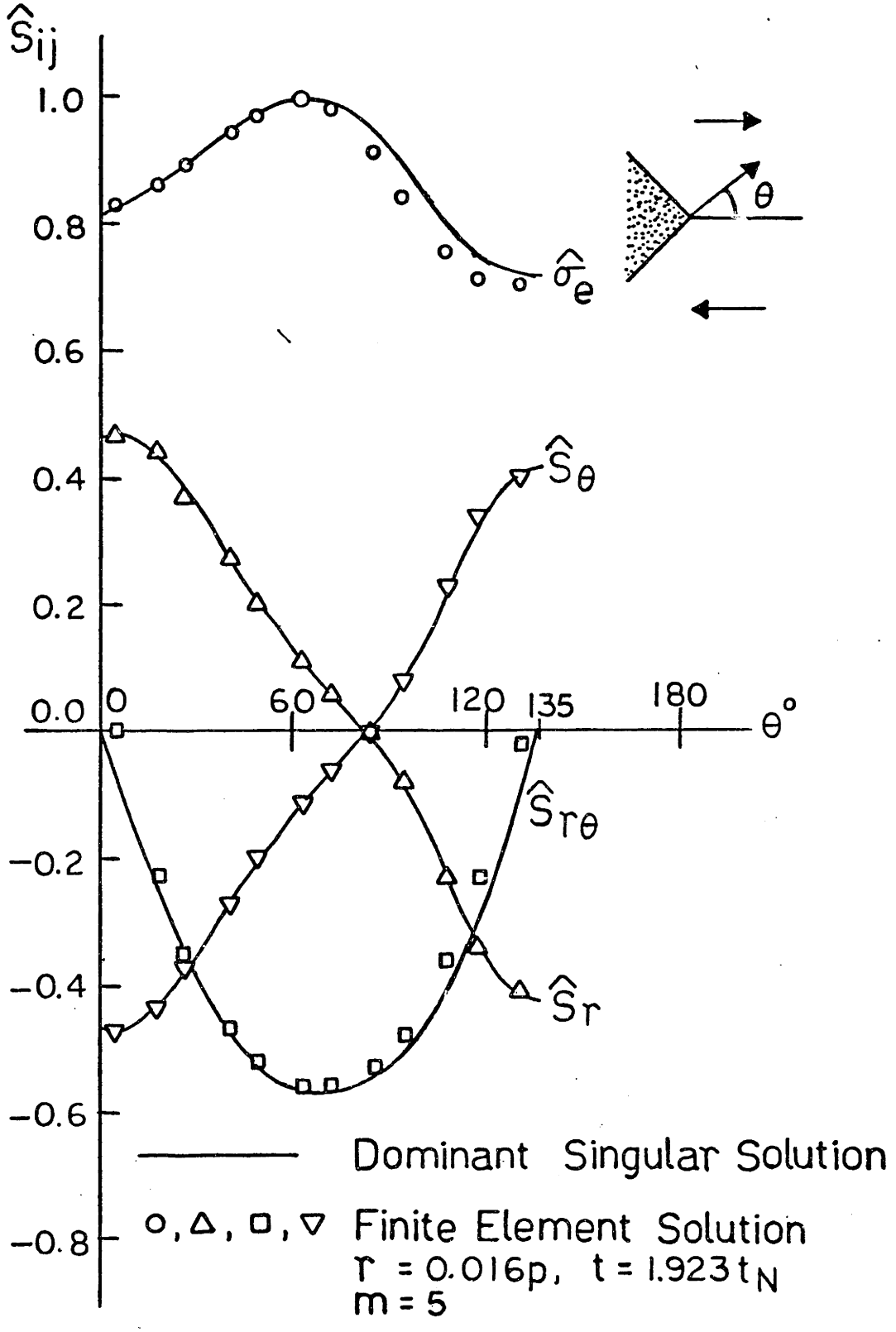

Figure 4.9 FEM Solution at the Apex of a Hard Particle of $\omega = \pi/4$, $m = 5$, $r = 0.016p$, $t = 1.923t_N$.

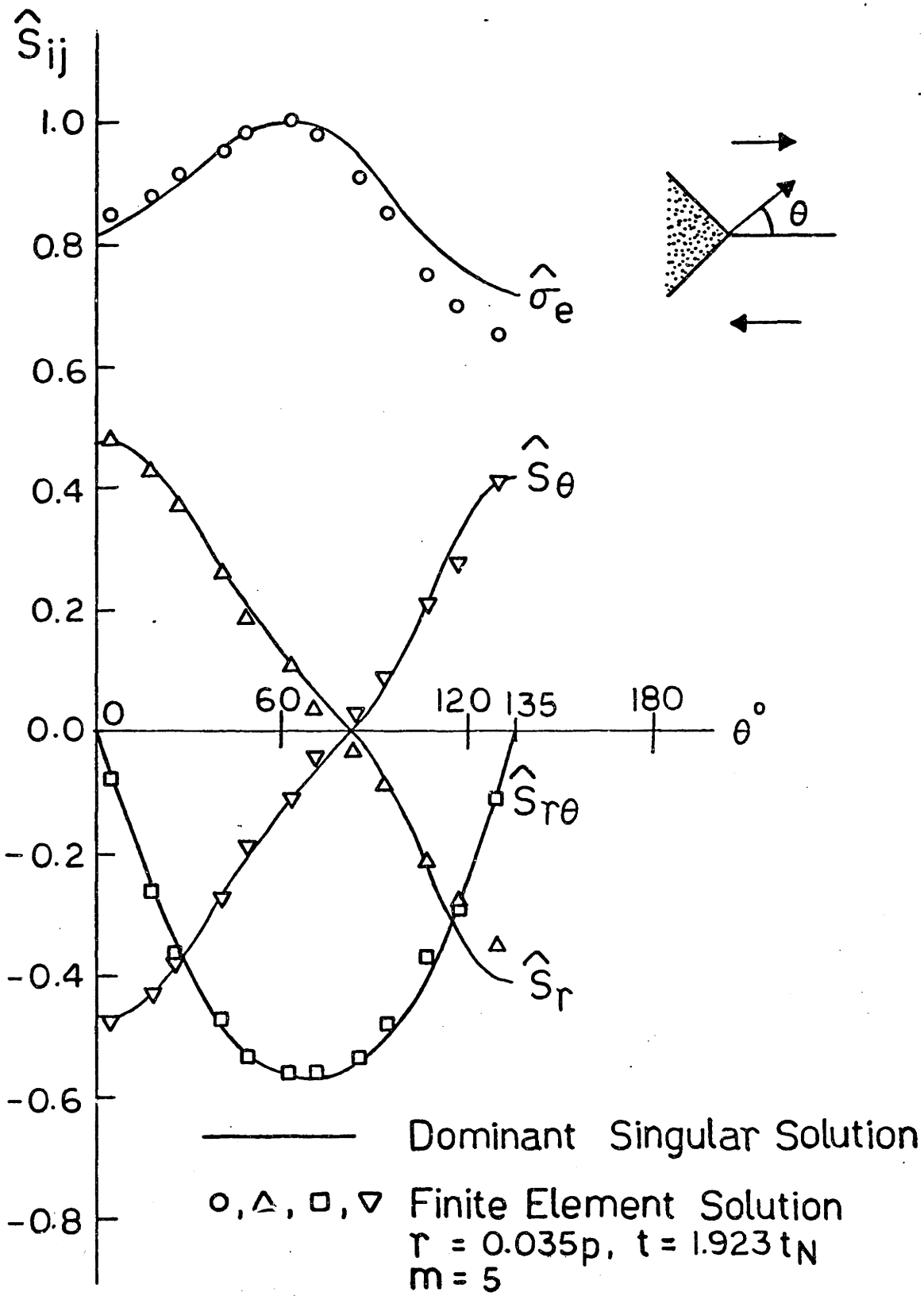

Figure 4.10 FEM Solution at the Apex of a Hard Particle of $\omega = \pi/4$ $m = 5$, $r = 0.035p$, $t = 1.923t_N$.

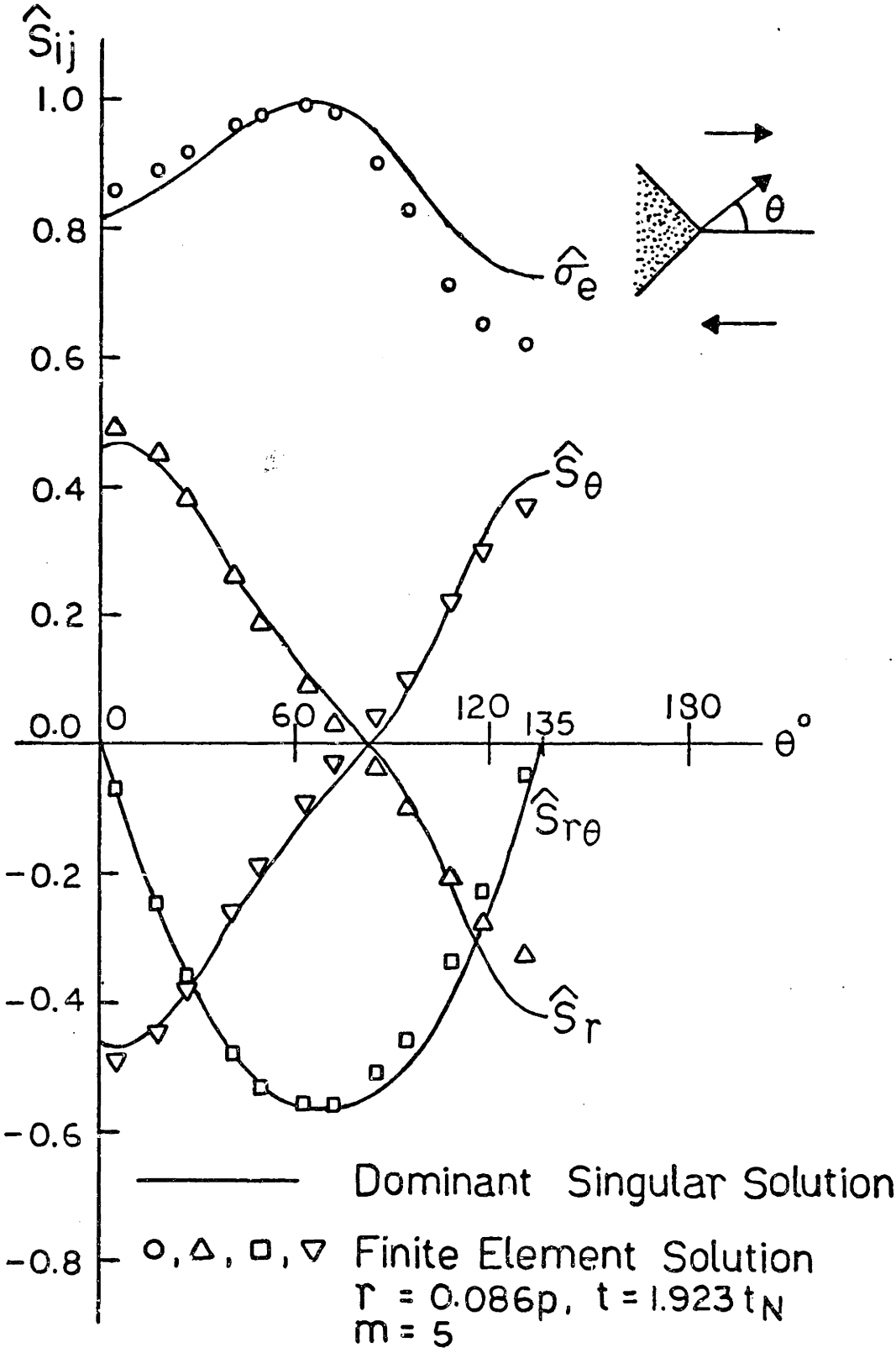

Figure 4.11 FEM Solution at the Apex of a Hard Particle of $\omega = \pi/4$, $m = 5$, $r = 0.086p$, $t = 1.923t_N$.

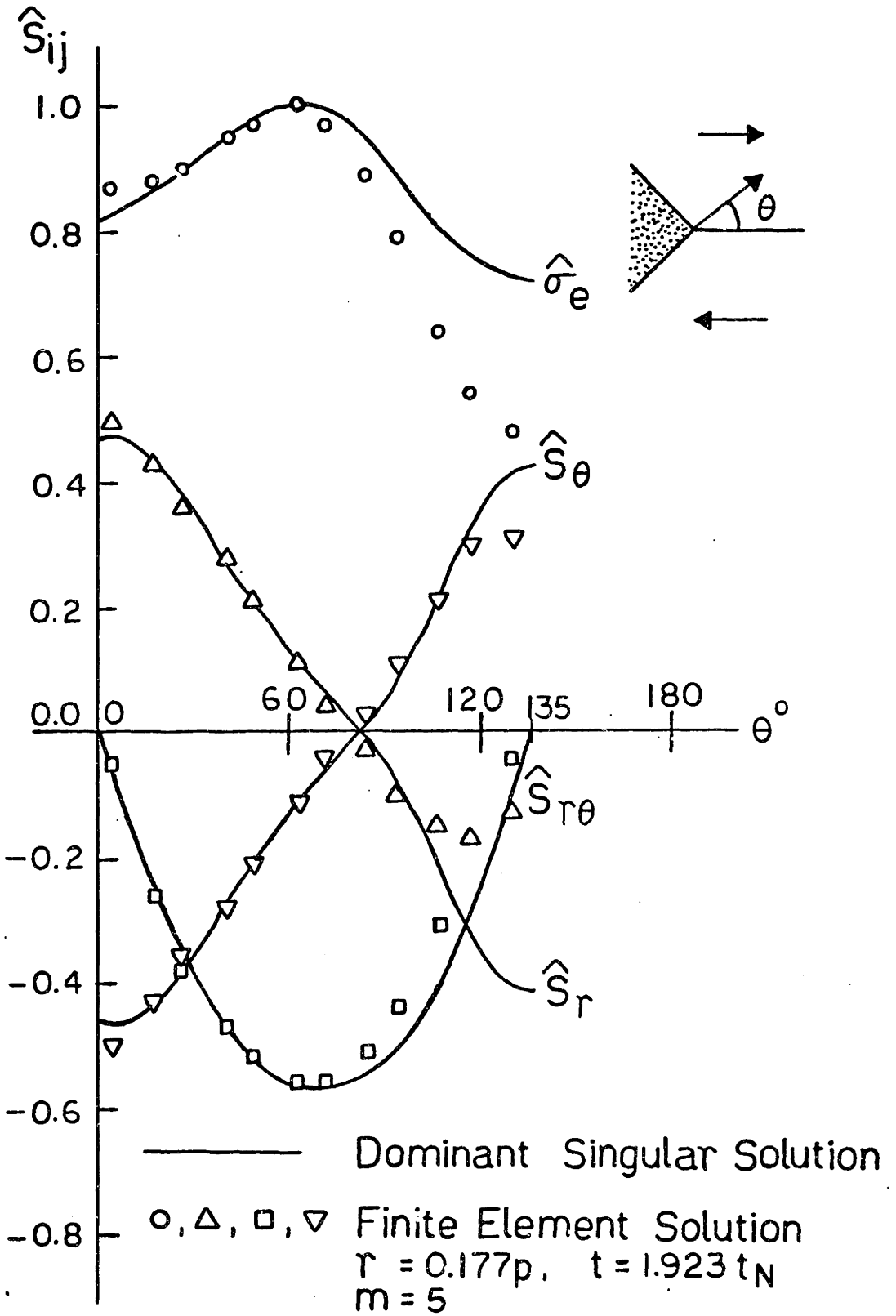

Figure 4.12 FEM Solution at the Apex of a Hard Particle of $\omega = \pi/4$, $m = 5$, $r = 0.177p$, $t = 1.923t_N$.

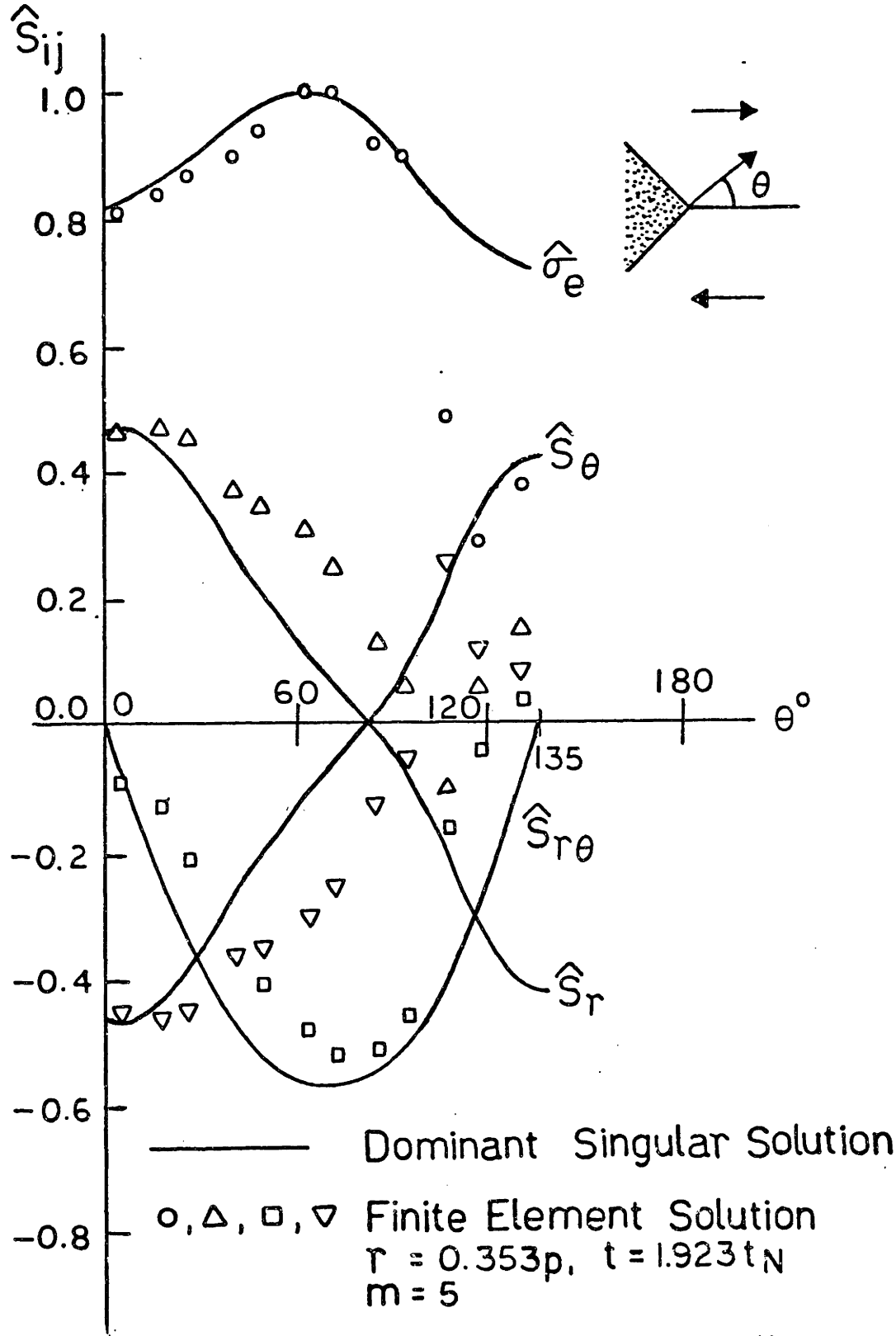

Figure 4.13 FEM Solution at the Apex of a Hard Particle of $\omega = \pi/4$, $m = 5$, $r = 0.353p$, $t = 1.923t_N$.

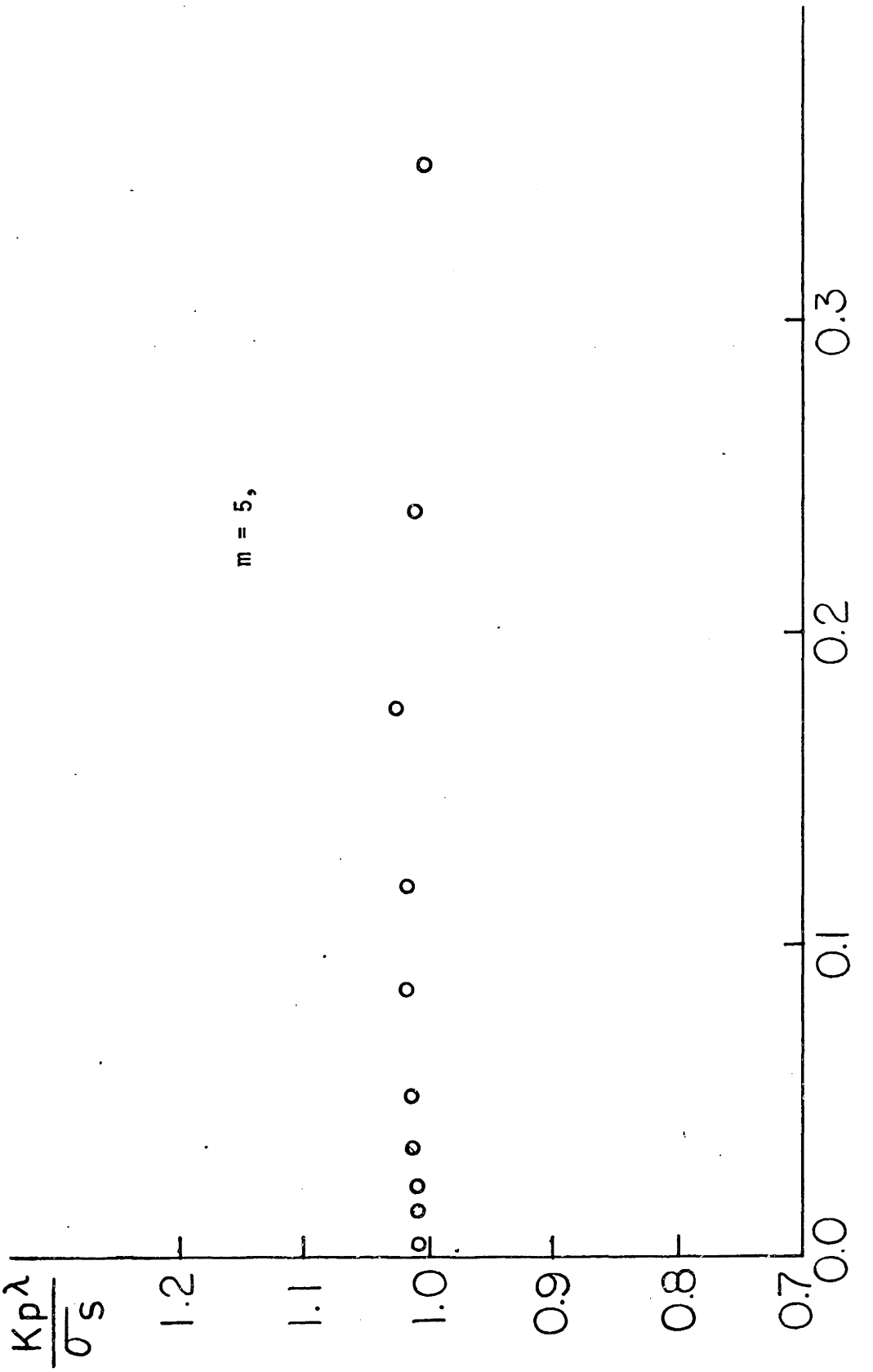

Figure 4.14 Variation of $(Kp^{\lambda})/\sigma_s$ with r/p at $t/t_N = 1.923$, m = 5.

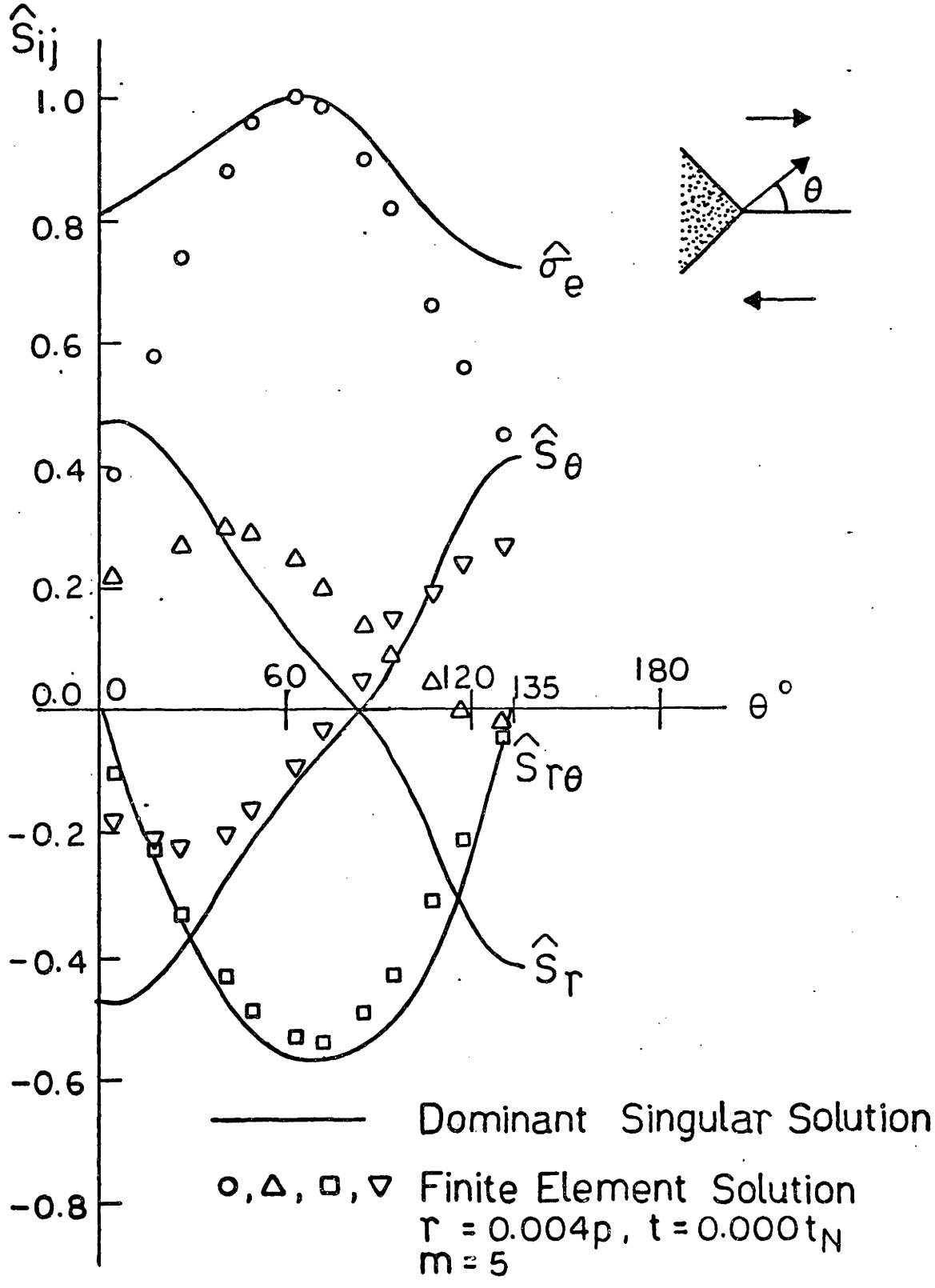

Figure 4.15 FEM Solution at the Apex of a Hard Particle of $\omega = \pi/4$, $m = 5$, $r = 0.004p$, $t = 0.000t_N$.

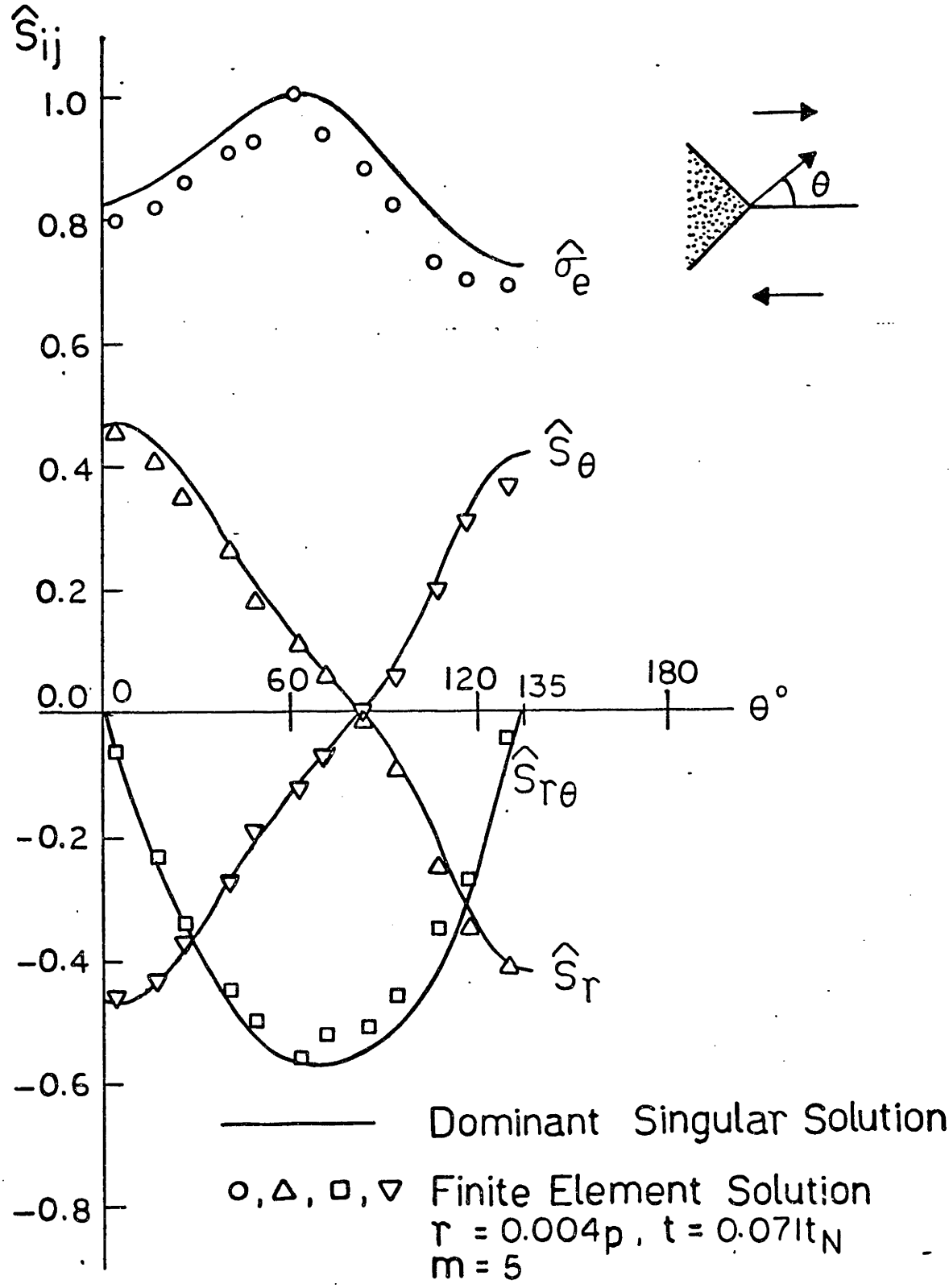

Figure 4.16 FEM Solution at the Apex of a Hard Particle of $\omega = \pi/4$, $m = 5$, $r = 0.004p$, $t = 0.071t_N$.

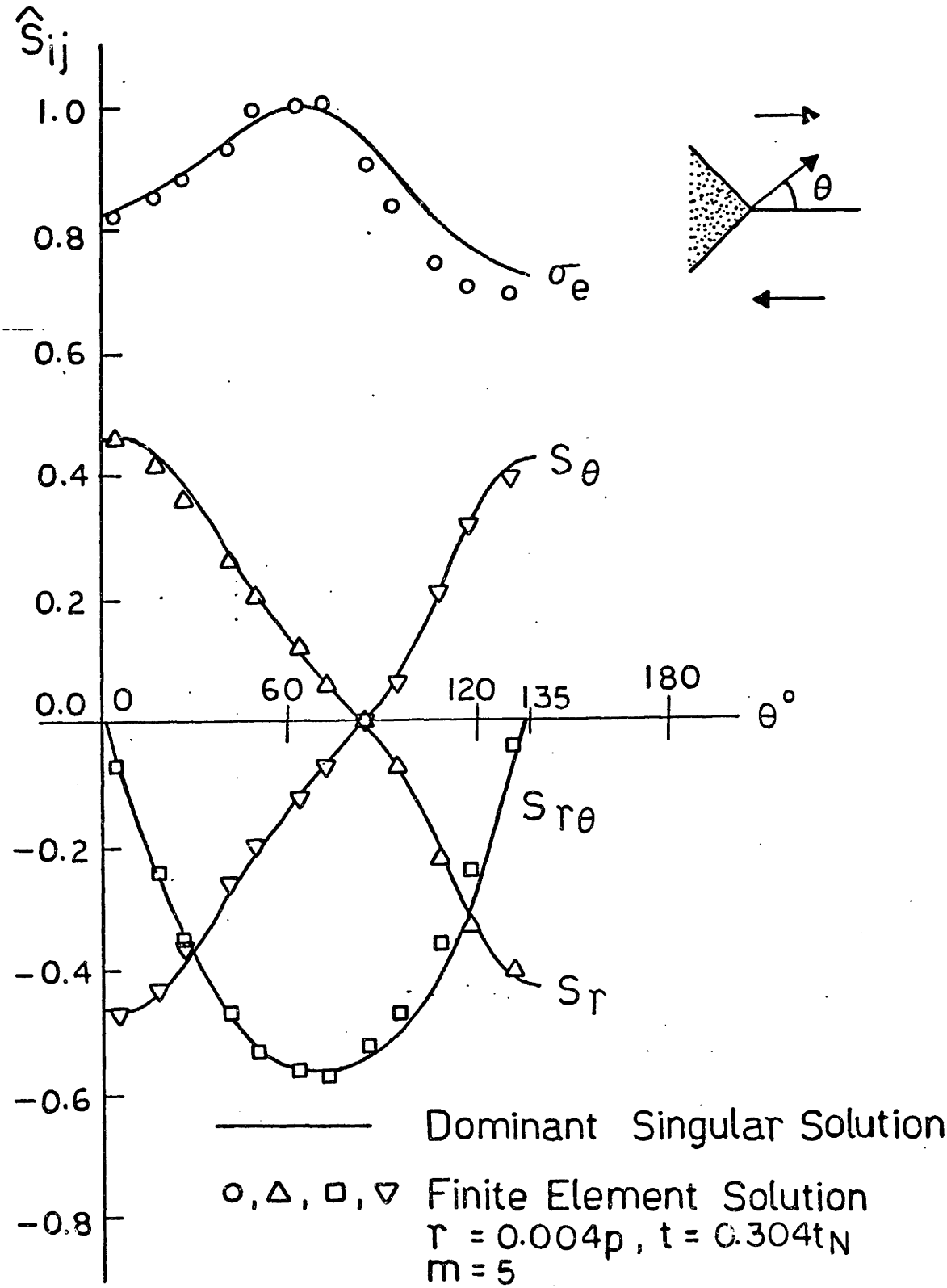

Figure 4.17 FEM Solution at the Apex of a Hard Particle $\omega = \pi/4$, $m = 5$, $r = 0.004p$, $t = 0.304t_N$.

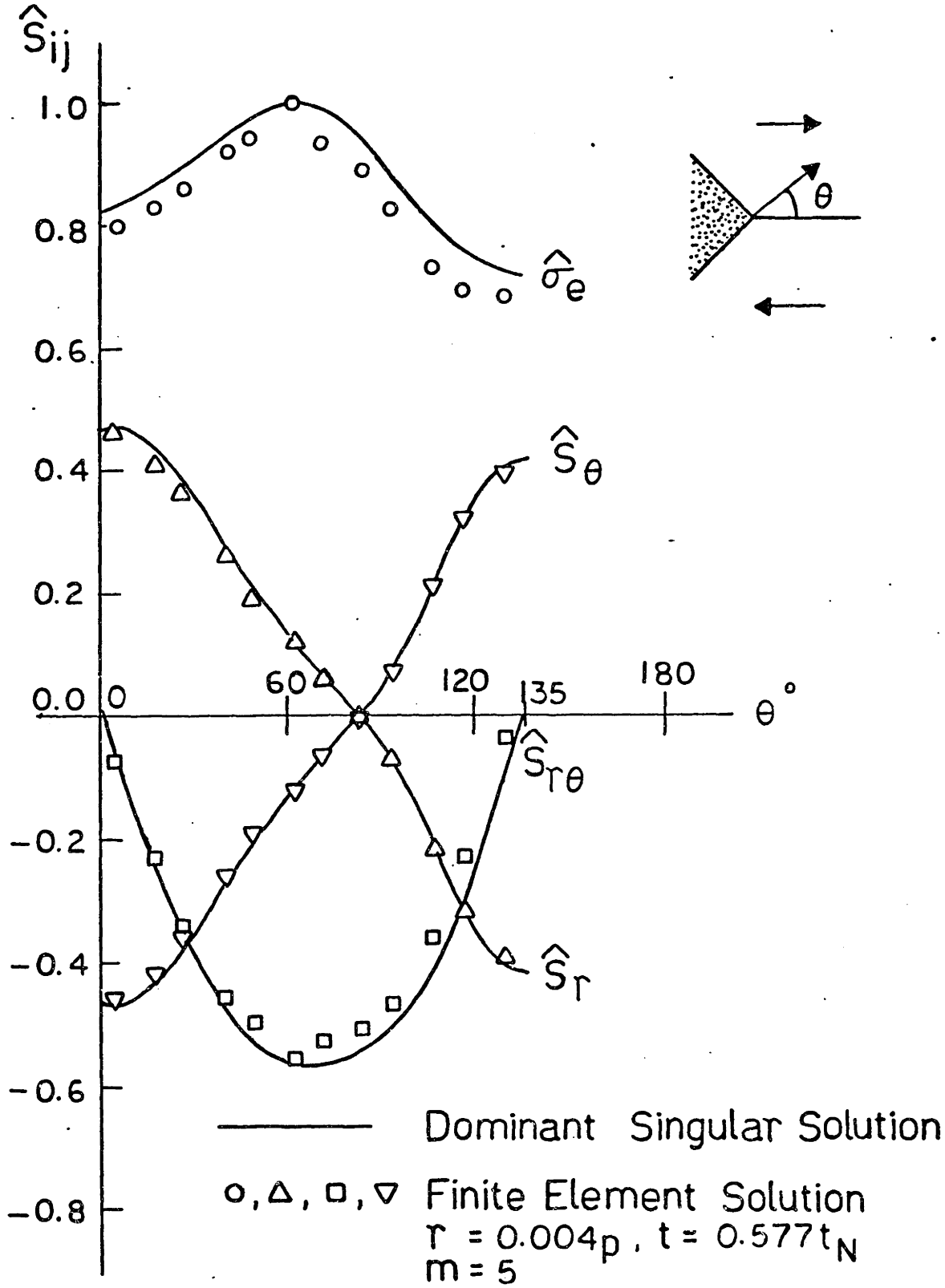

Figure 4.18 FEM Solution at the Apex of a Hard Particle of $\omega = \pi/4$, $m = 5$, $r = 0.004p$, $t = 0.577t_N$.

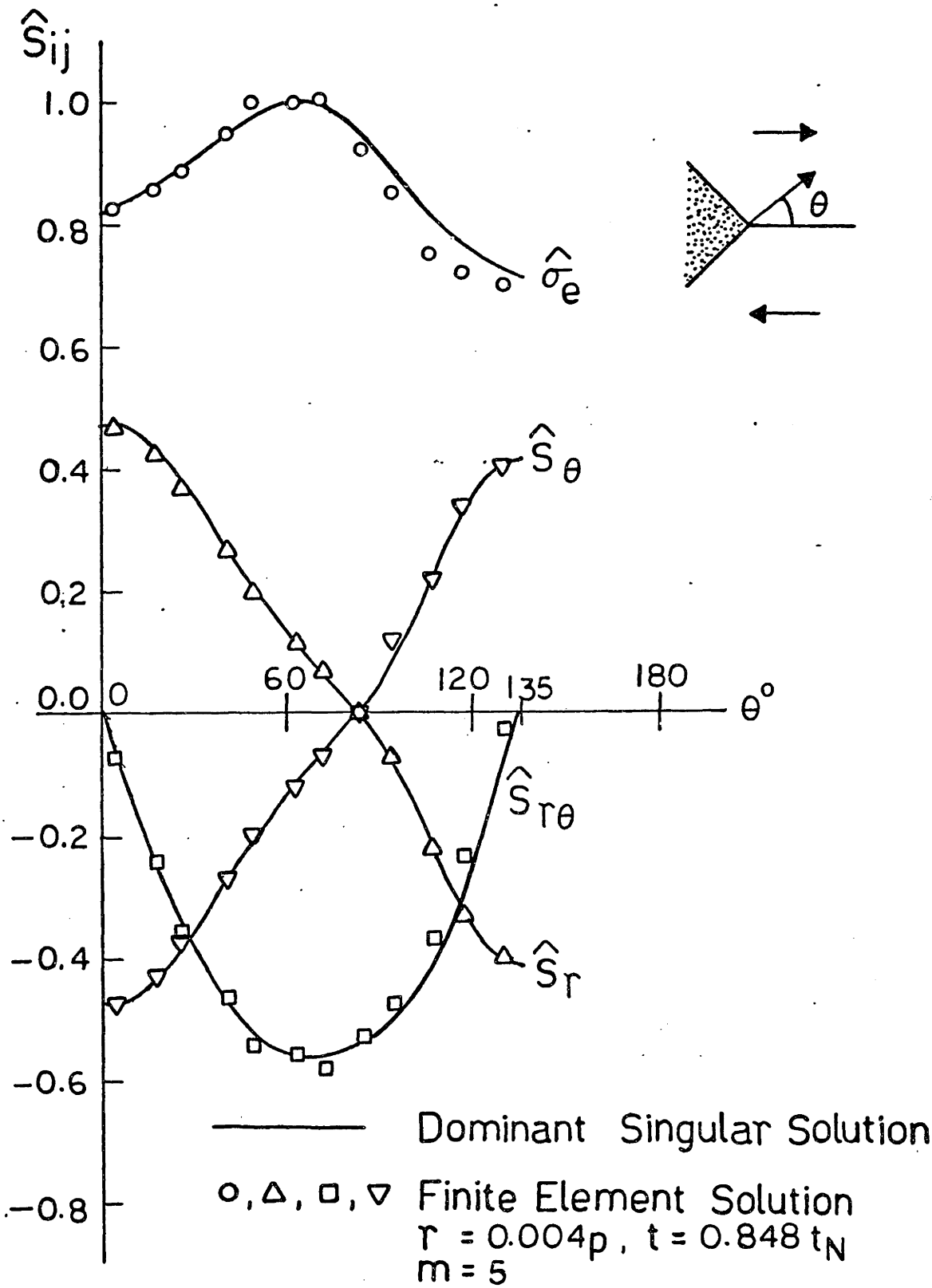

Figure 4.19 FEM Solution at the Apex of a Hard Particle of $\omega = \pi/4$, $m = 5$, $r = 0.004p$, $t = 0.848t_N$.

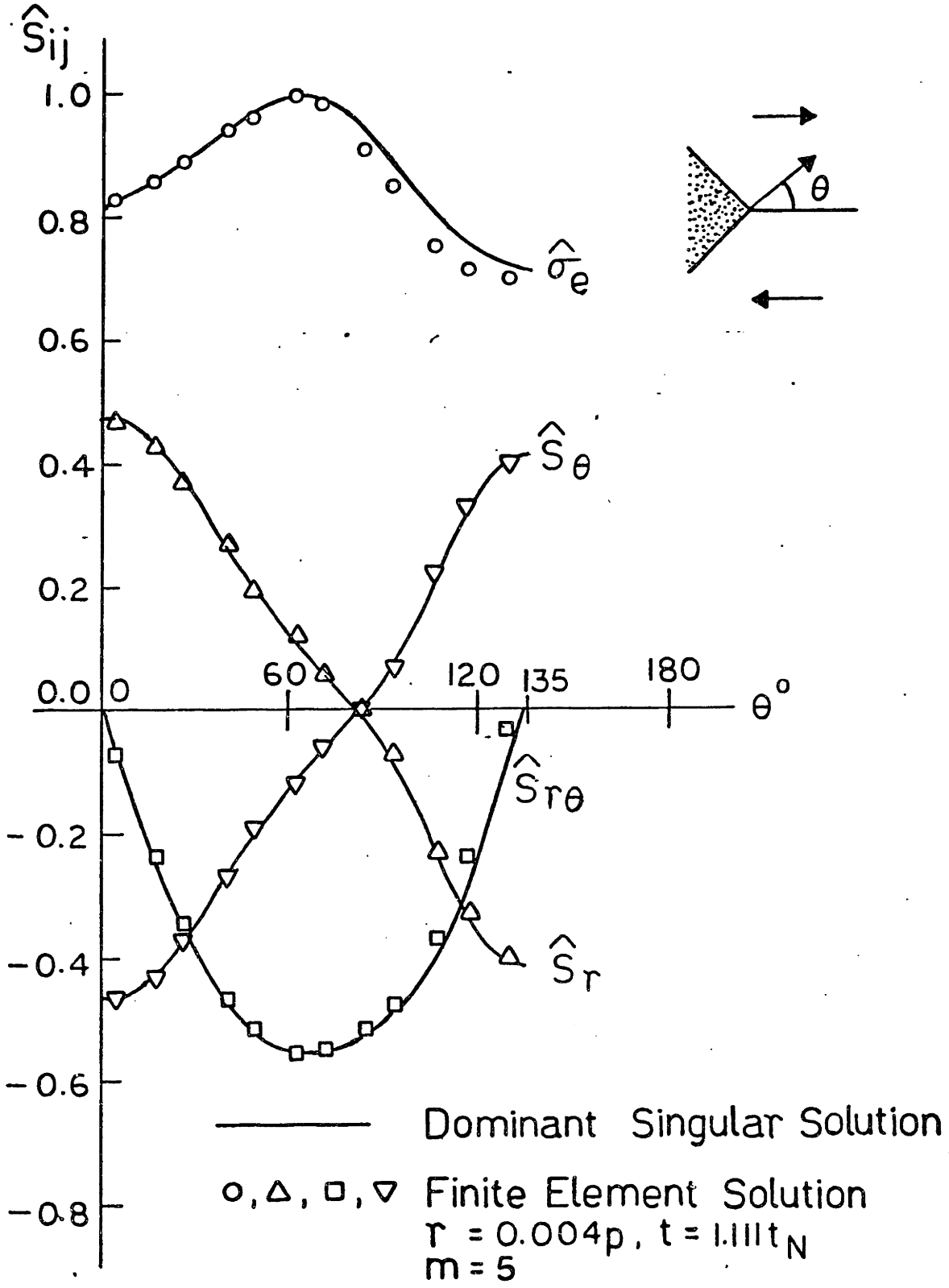

Figure 4.20 FEM Solution at the Apex of a Hard Particle of $\omega = \pi/4$, $m = 5$, $r = 0.004p$, $t = 1.111t_N$.

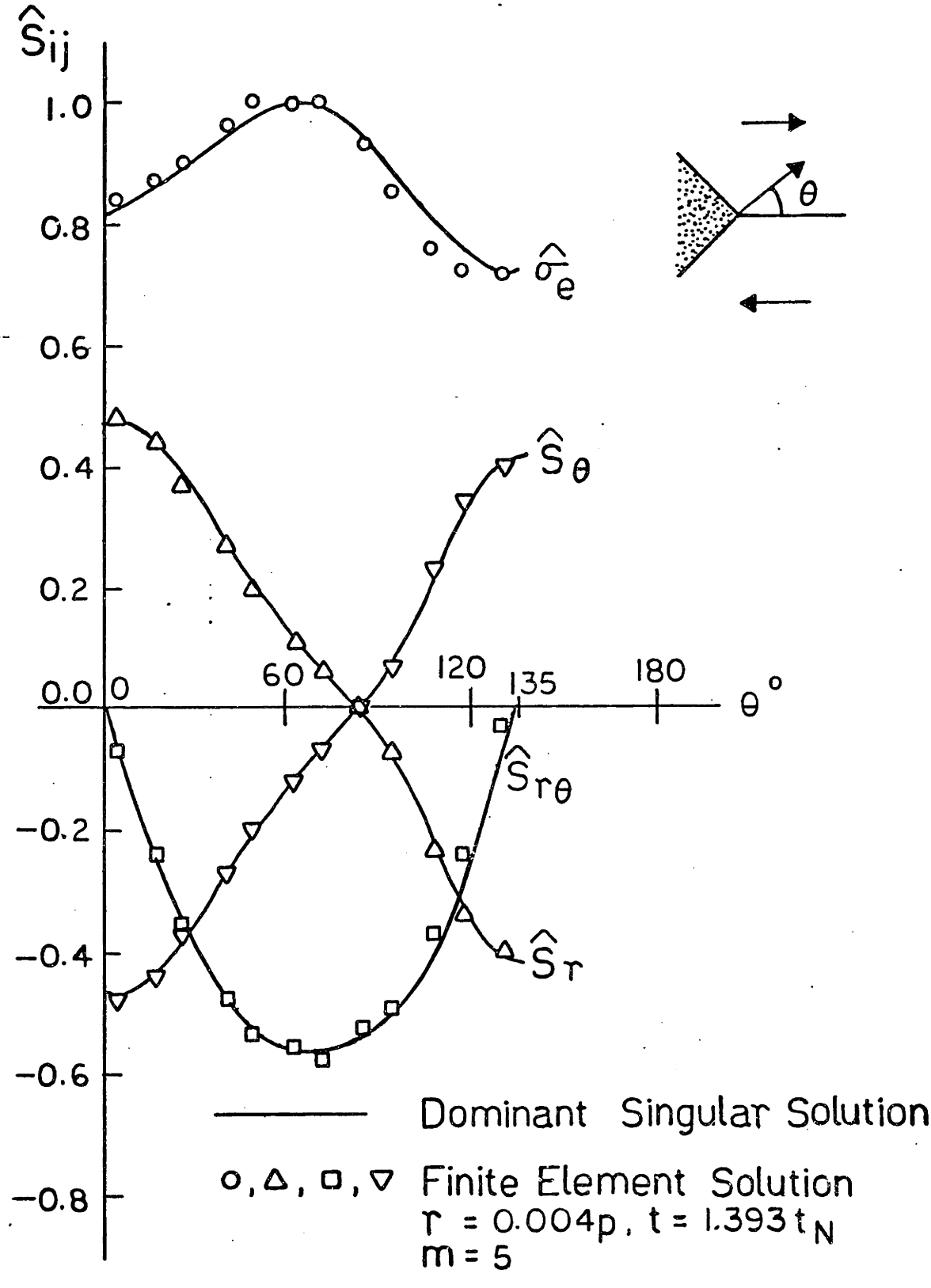

Figure 4.21 FEM Solution at the Apex of a Hard Particle of $\omega = \pi/4$, $m = 5$, $r = 0.004p$, $t = 1.393t_N$.

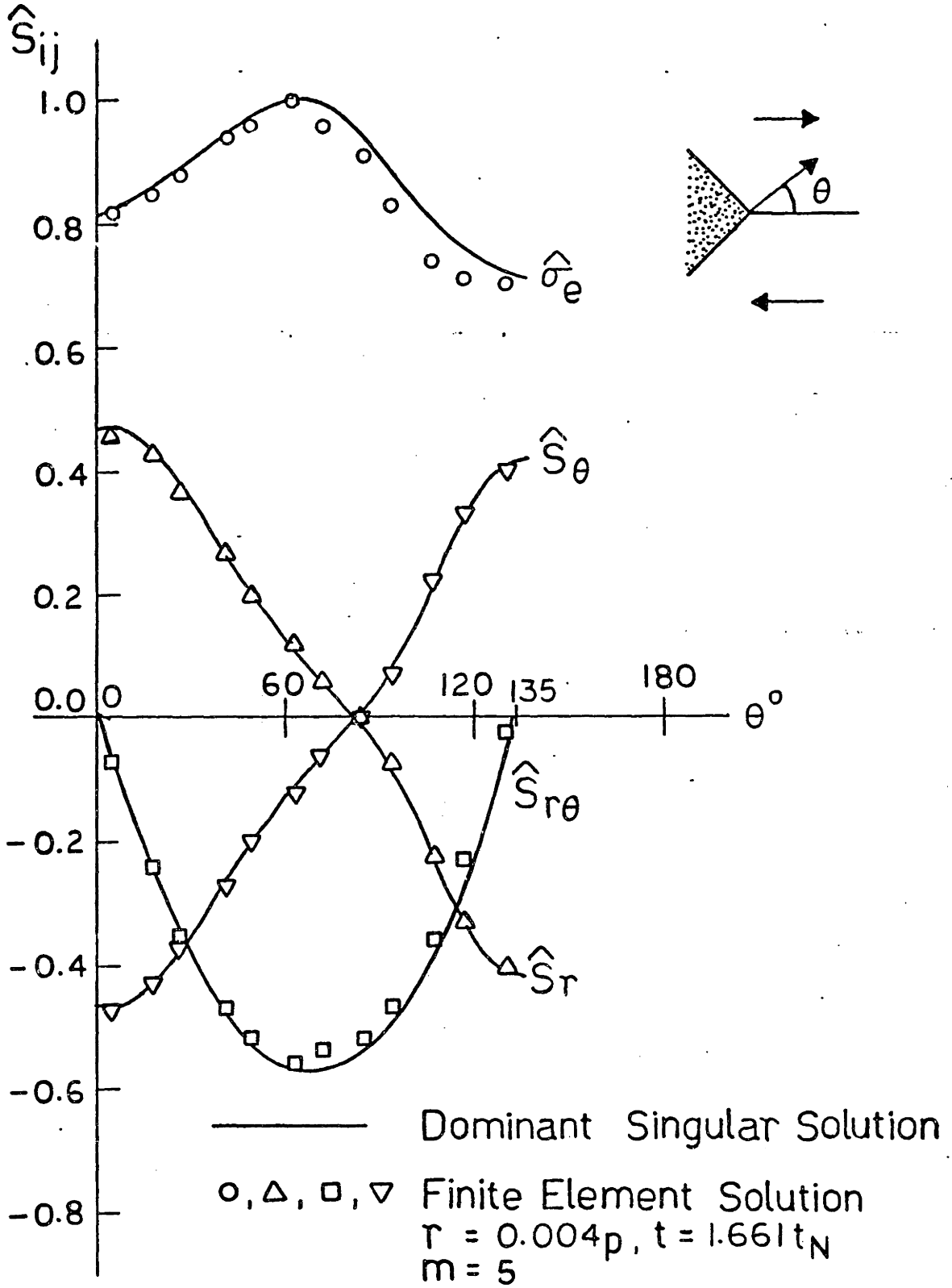

Figure 4.22 FEM Solution at the Apex of a Hard Particle of $\omega = \pi/4$, $m = 5$, $r = 0.004p$, $t = 1.661 t_N$.

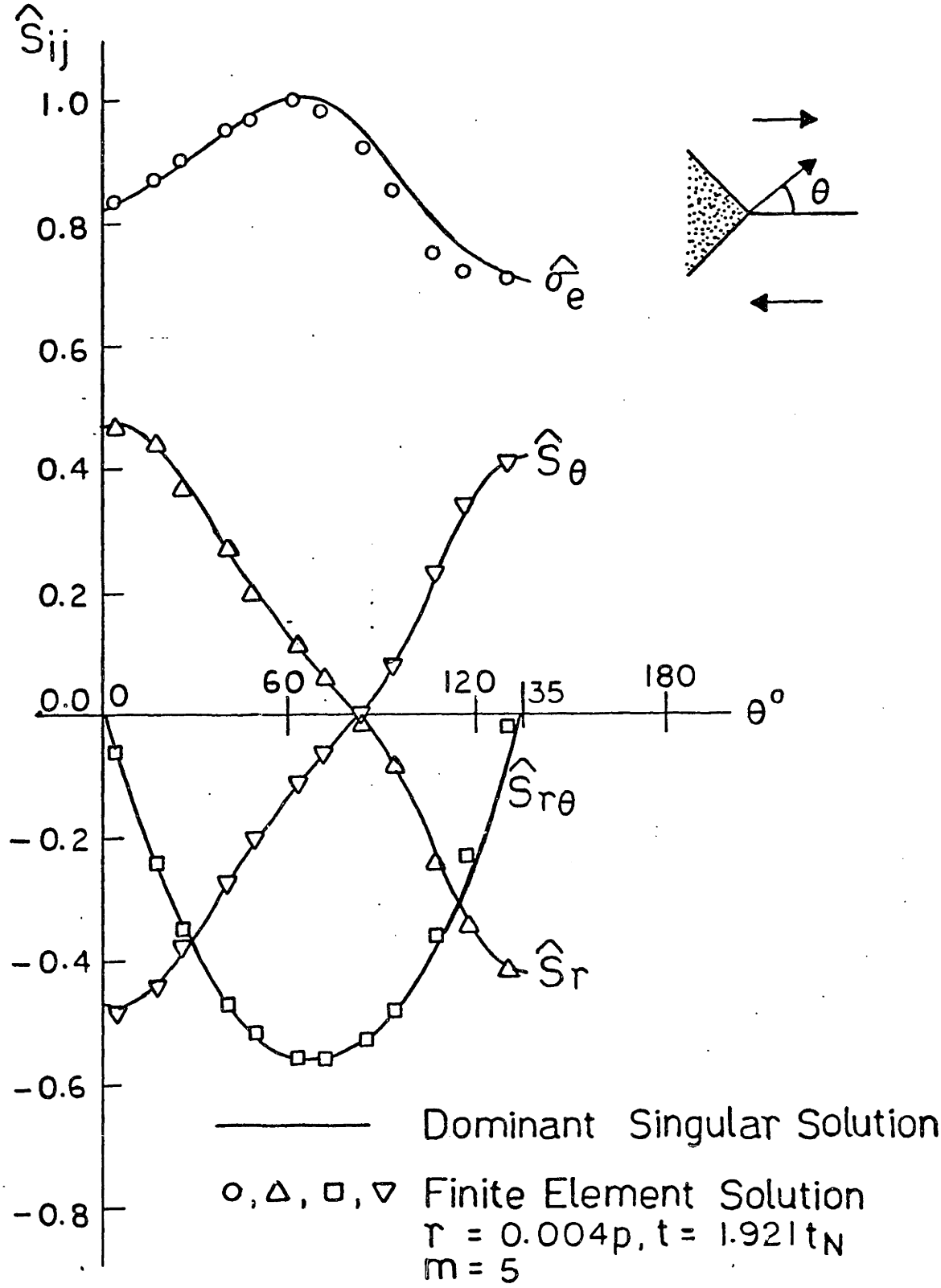

Figure 4.23 FEM Solution at the Apex of a Hard Particle of $\omega = \pi/4$, $m = 5$, $r = 0.004p$, $t = 1.921t_N$.

dominance of the creep strain over the elastic strain as a function of time. It is apparent that after $t = 0.0577t_N$, the deviatoiic stresses at $r = 0.004p$ are dominated by the steady state singular creep solution. Figure 4.24 shows the value of Kp^{λ}/σ_s determined from data corresponding to Figs. 4.16 to 4.23. There are only minimal fluctuations in Kp^{λ}/σ_s over time, indicating the self-adapting time step selection scheme of Section 4.2.2 (with f mostly in a sequence of 5,5,2,2,2, repeat steps) works quite well.

With values of Kp^{λ}/σ_s obtained for m = 3 and m = 5, one can estimate the Kp^{λ}/σ_s values for other m by extrapolation. First, one can apply overall equilibrium consideration to a characteristic repeat unit of the geometry (Fig. 4.4) and assume that the $\hat{\sigma}_{\theta\theta}$ (of the singular solution) at the particle-grain interface is the only stress to balance the far field shear stress, σ_s, as was done by Argon, Chen and Lau (1980). This gives

$$\frac{Kp^{\lambda}}{\sigma_s} \cdot \frac{p}{\ell} \cdot \tan\omega = \frac{(1+\lambda)(2\cos\omega)^{\lambda}}{\hat{\sigma}_{\theta\theta}(\pi-\omega)} \equiv I(m) \qquad (4.11)$$

where ω is the apex half angle of the particle. However, in reality, $\hat{\sigma}_{\theta\theta}(\pi-\omega)$ of the singular solution

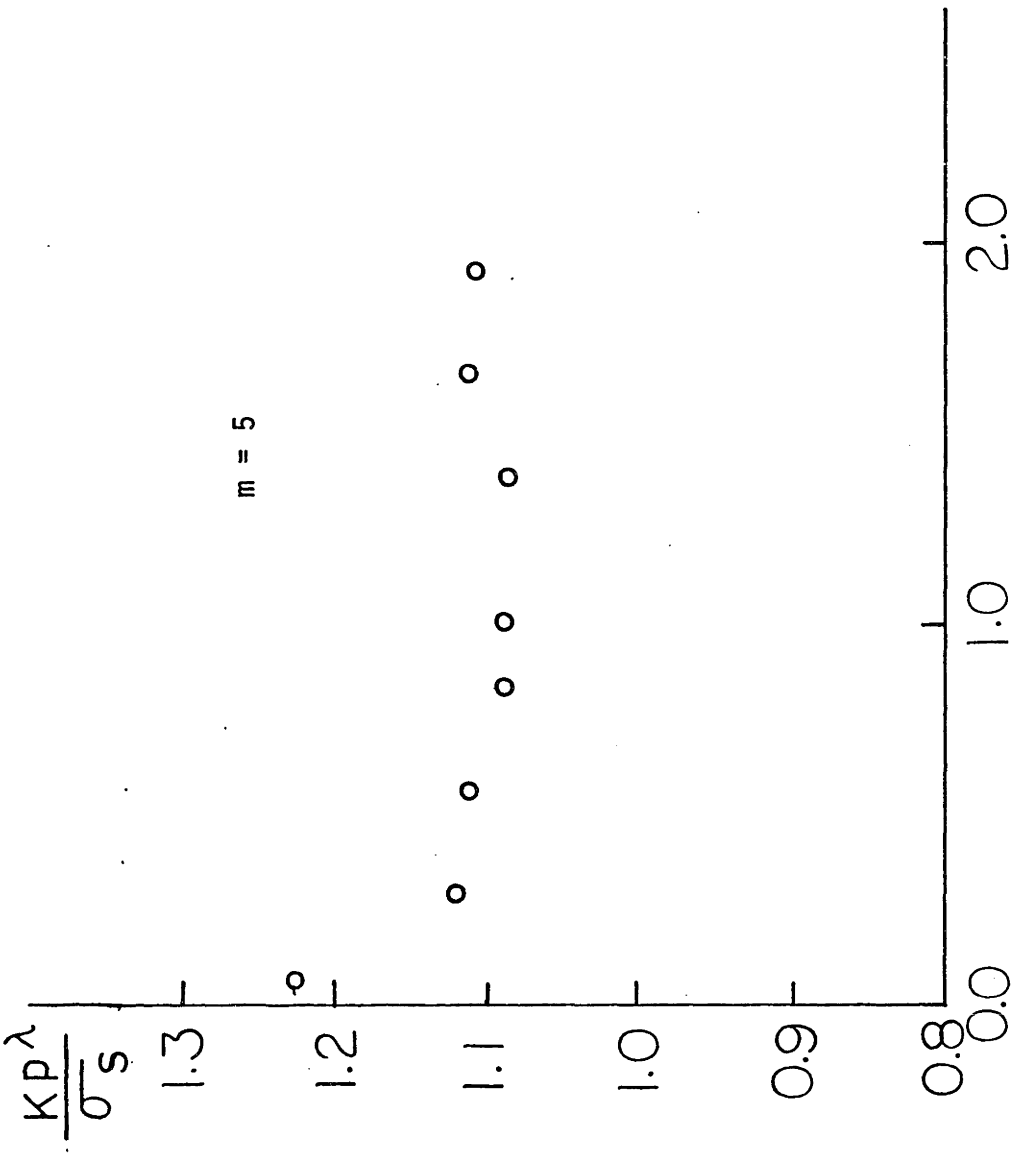

Figure 4.24 Variation of $(Kp^{\lambda})/\sigma_s$ with t/t_N, m = 5, r/p = 0.004.

does not have a range over the entire surface of the particle. Equation 4.11 thus tends to overestimate K_p^{λ}/σ_s. The amount of this overestimation can be treated as an empirical correction factor C which most likely varies with m. Hence, a more appropriate estimation of K_p^{λ}/σ_s is

$$\frac{K_p^{\lambda}}{\sigma_s} \cdot \frac{P}{\ell} \cdot \tan\omega = C(m) \cdot I(m) \qquad (4.12)$$

This function C(m) can be empirically determined. From our m = 3 and m = 5 results,

$$C(m) = 0.689 + 0.039 \cdot (m-3) \qquad (4.13)$$

The function I(m) is known once the singularity solution of Chapter 3 is known, and Eq. 4.13 and 4.12 then enables one to estimate K_p^{λ}/σ_s. For a square, hard particle of $\omega=\pi/4$, I(m) and $(K_p^{\lambda}/\sigma_s)\cdot(P/\ell)$ are shown in Fig. 4.25. Actual values of I(m), C(m) and $(K_p^{\lambda}/\sigma_s)\cdot(P/\ell)\cdot\tan\omega$ are given in Table 4.1.

4.4 FEM Solution for the Triple Grain Junction

Figure 4.26 states the geometry and boundary conditions at the triple grain junction. Figure 4.27 shows the finite element mesh used in our analysis.

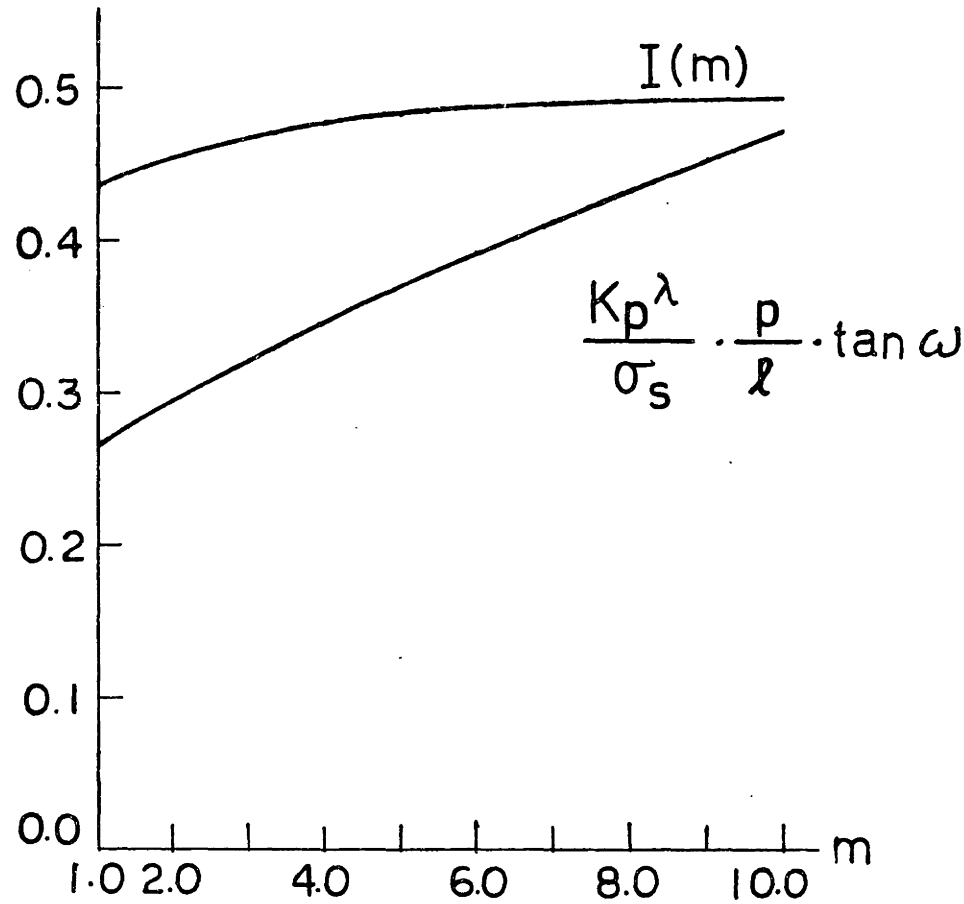

Figure 4.25 Variation of I(m) and $(Kp^{\lambda}/\sigma_s)\cdot(p/\ell)\cdot\tan\omega$ with m for a Square Hard Particle of $\omega = \pi/4$.

TABLE 4.1

I(m), C(m) and $\frac{Kp^{\lambda}}{\sigma_s}\cdot\frac{p}{\ell}\cdot\tan\omega$ FOR A HARD PARTICLE OF $\omega=\pi/4$

m	$I(m) = \frac{(1+\lambda)(2x\cos 45°)^{\lambda}}{\hat{\sigma}_{\theta\theta}(135°)}$	C(m)	$\frac{Kp^{\lambda}}{\sigma_s \cdot / \ell / p}$
1	0.437	0.611	0.267
2	0.454	0.650	0.295
3	0.468	0.689	0.322
4	0.477	0.728	0.347
5	0.482	0.767	0.370
6	0.486	0.806	0.392
7	0.489	0.845	0.413
8	0.490	0.884	0.433
9	0.492	0.923	0.454
10	0.493	0.962	0.474

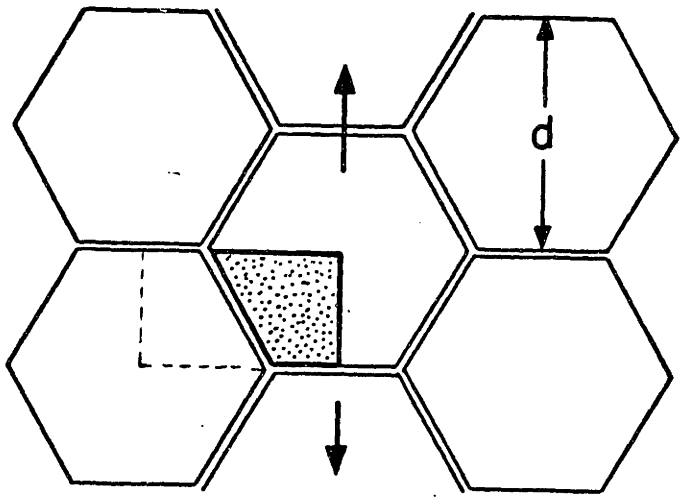

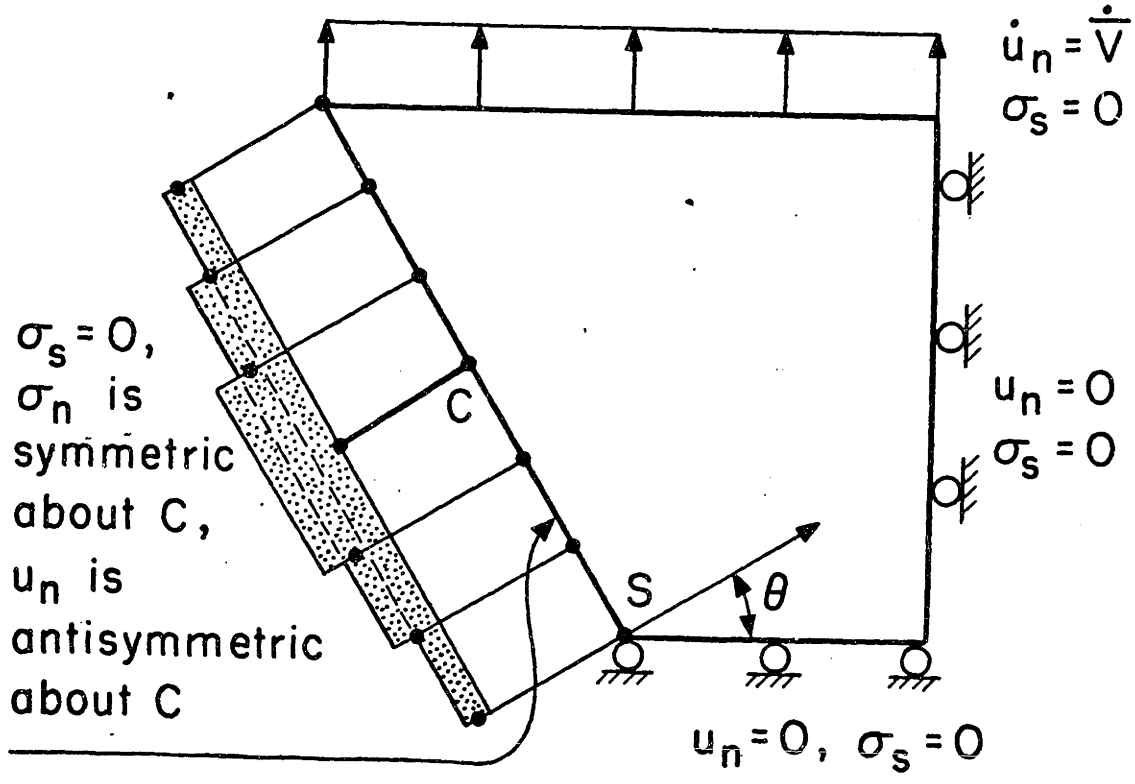

Figure 4.26 Definition of Problem on Triple Grain Junction Stress Concentration: Statement of the FEM Problem.

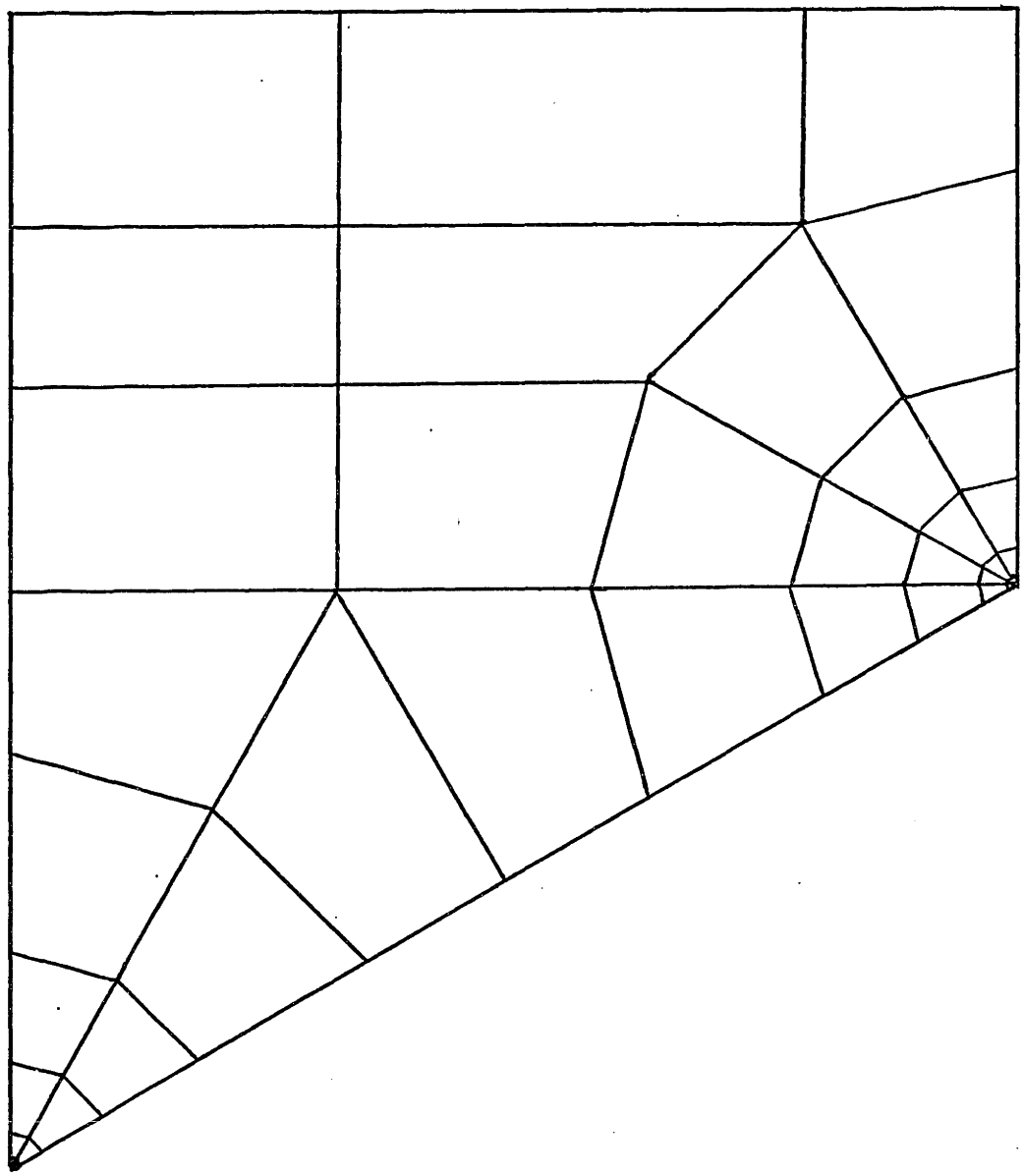

Figure 4.27 Finite Element Mesh for the Triple Grain Junction Problem.

Solutions have been obtained for m=3 and m=5.

The principal boundary condition is the vertical velocity $\dot{\bar{V}}$ (Fig. 4.26) which was assigned a value at t=0 and kept constant for all subsequent time. The value of $\dot{\bar{V}}$ was assigned such that at steady state creep, it will generate a nominal stress, $\sigma_N=10^{-3}E$. The first time step was assigned as $\Delta t = 1t_N$ such that its solution (at $t=t_N$) corresponds to an elastic response of the boundary moving at $\dot{\bar{V}}$ for t_N. The very high stresses then activate massive creep deformation in the second and subsequent steps to quickly reach steady state creep. Useful information for the determination of K is furnished by those stress sampling points in which the accumulated creep strain dominates over the elastic strain. The time step increments, other than the first step, are automatically chosen by Eq. 4.6. For m=3, f (Eq. 4.6) is always set to be 1.0. For m=5, f is assigned a sequence which consists mostly of (5,5,2,2,2, repeat). The computed quantity of $r^{\lambda}\sigma_e(66.22°) = K\hat{\sigma}_e(66.22°)$ of the finite element solution, after divided by a scaling constant h, is used to match to $\hat{\sigma}_e(66.22°)$ of the singular solution and hence determine Kd^{λ}/σ_N.

Figure 4.28 shows the comparison of FEM result and the singular solution of Chapter 3, at r=0.001d, after

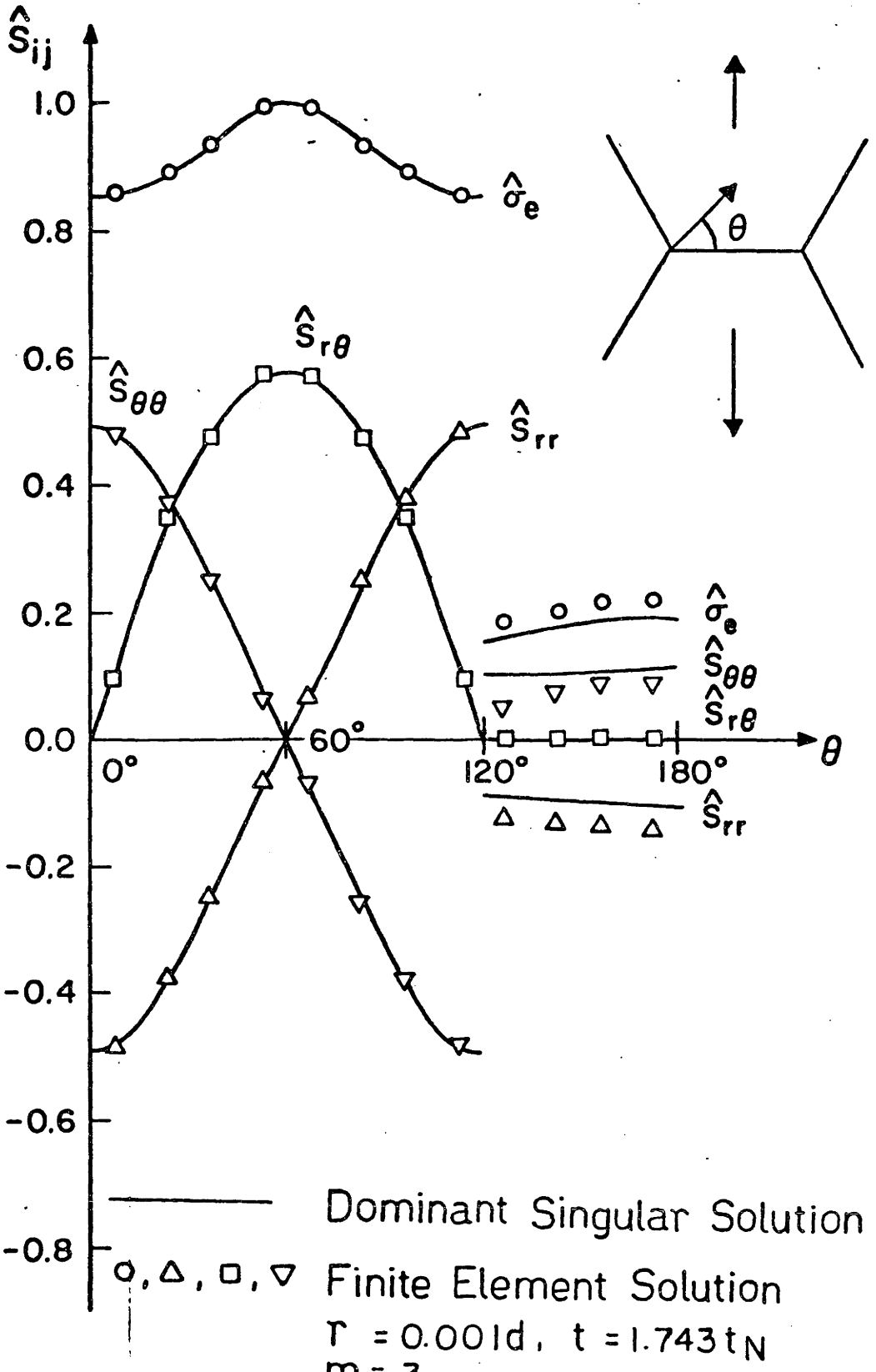

Figure 4.28 FEM Solution at Triple Grain Junction, m = 3, r = 0.001d. t = 1.743t_N.

the above-mentioned match is made. The agreement is very good for $0 < \theta < 2\pi/3$ from which we determine Kd^{λ}/σ_N. The agreement is not as good in $2\pi/3 < \theta < \pi$. This is due to the fact that such data is taken from a corner of the mesh where displacement rate boundary conditions are enforced (Fig. 4.26 - 4.27). From these results from m = 3, the value of Kd^{λ}/σ_N is found to be 0.753.

For m = 5, Figs. 4.29 to 4.34 shows $\hat{S}_{ij}$ at various distance, r/d, at $t = 3.230t_N$. The dominant singular solution apparently is a good approximation at the triple point up to r = 0.096d. Figure 4.35 shows the computed Kd^{λ}/σ_N as a function of r/d for m = 5. Similar to the hard particle problem, Kd^{λ}/σ_N determined from $\hat{\sigma}_e$ at $\theta \simeq \pi/3$ (where $\hat{\sigma}_e$ is maximum) gives good accuracy even at large r/d where $\hat{S}_{ij}$ may locally deviate from the dominant singular solution.

Figures 4.36 to 4.45 show the effect of time (and accumulated creep strain) on the stress distribution at r = 0.001d. Contrary to the hard particle problem, $t_N = 1.0$ corresponds to the first step here and hence is the elastic solution. Figure 4.37 shows that at $t = 1.055t_N$, the creep strain and singular stress solution begin to dominate.

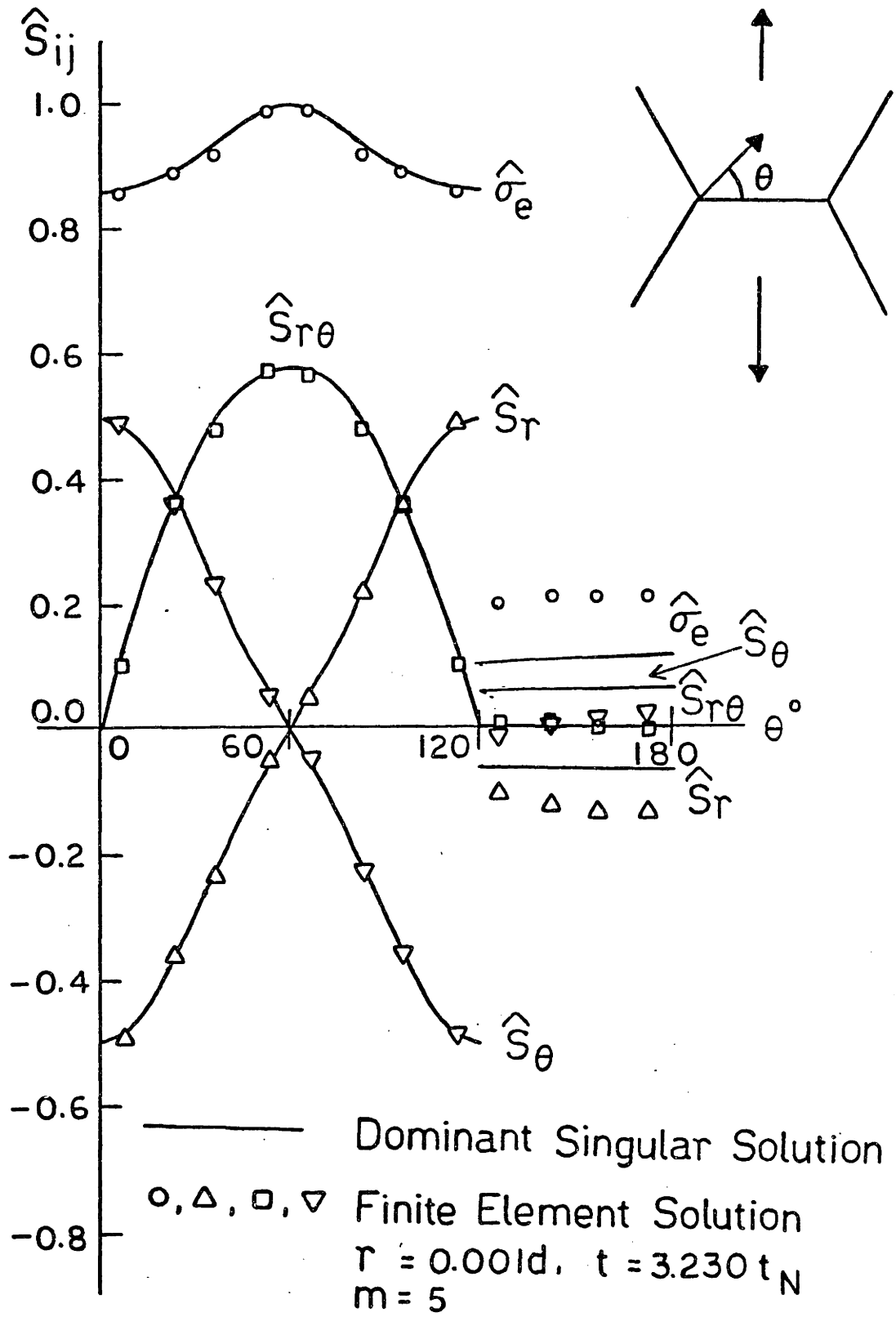

Figure 4.29 FEM Solution at Triple Grain Junction, m = 5, r = 0.001d, $t = 3.230t_N$.

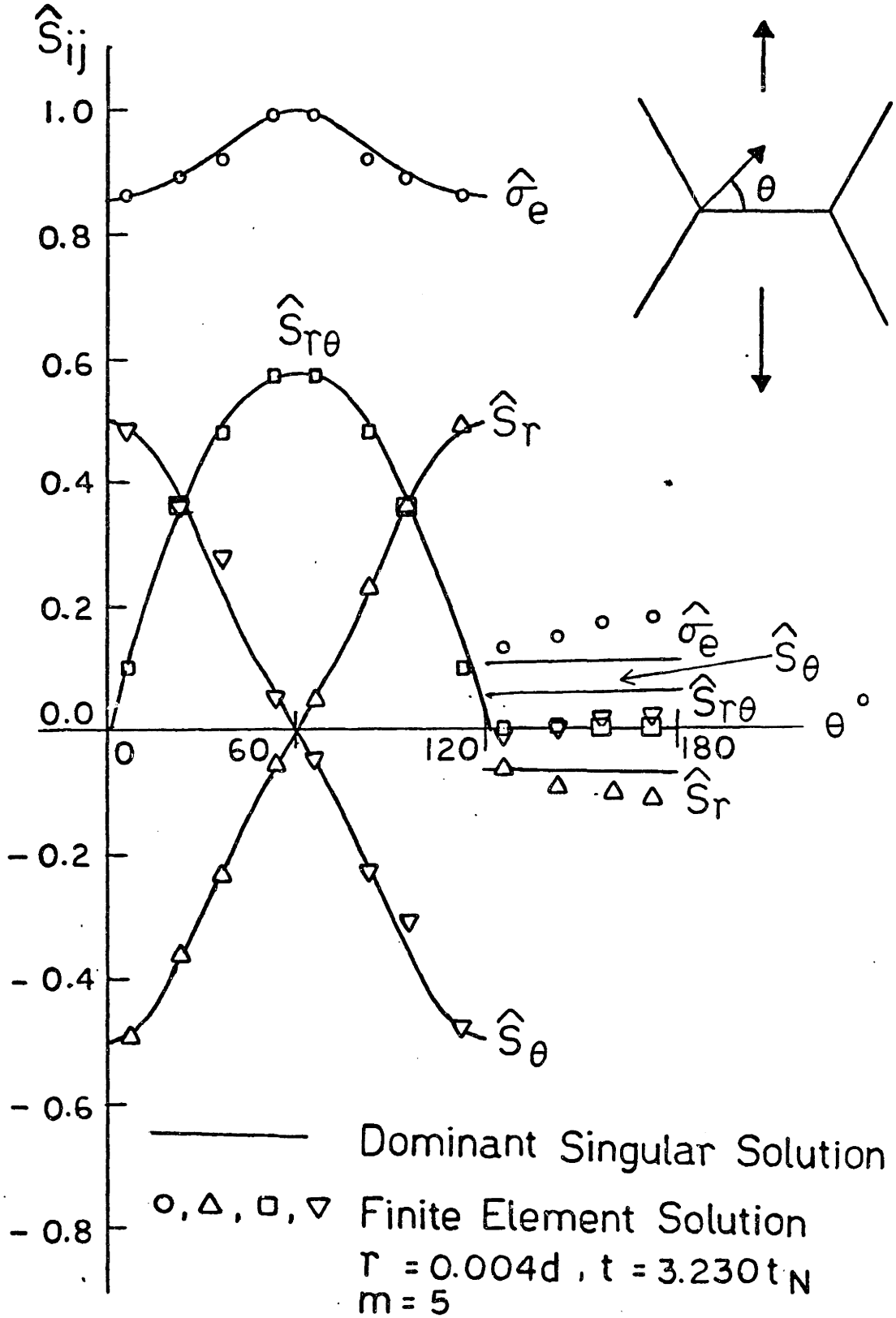

Figure 4.30 FEM Solution at Triple Grain Junction, m = 5, r = 0.004d, t = 3.230t_N.

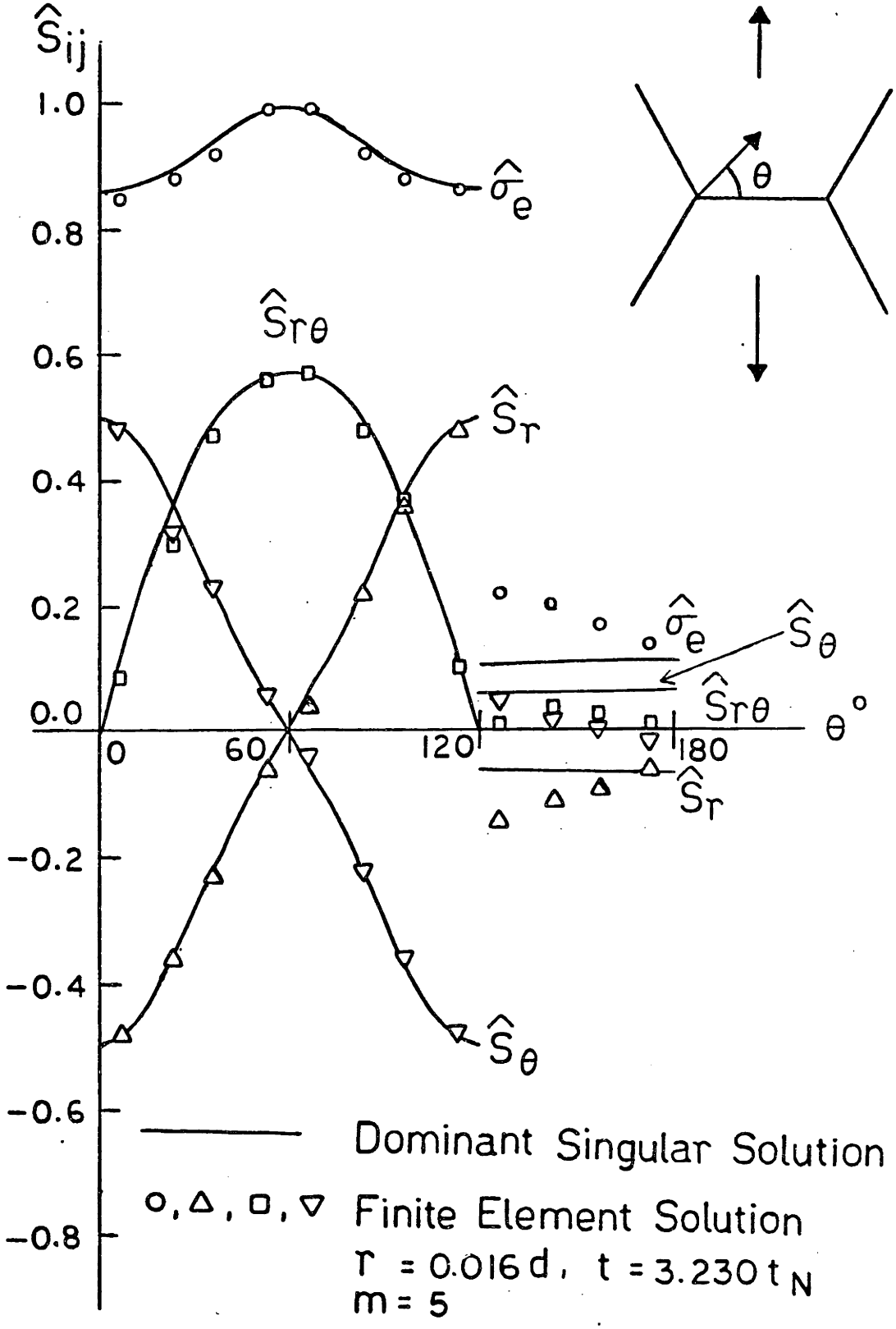

Figure 4.31 FEM Solution at Triple Grain Junction, m = 5, r = 0.016d, t = 3.230t_N.

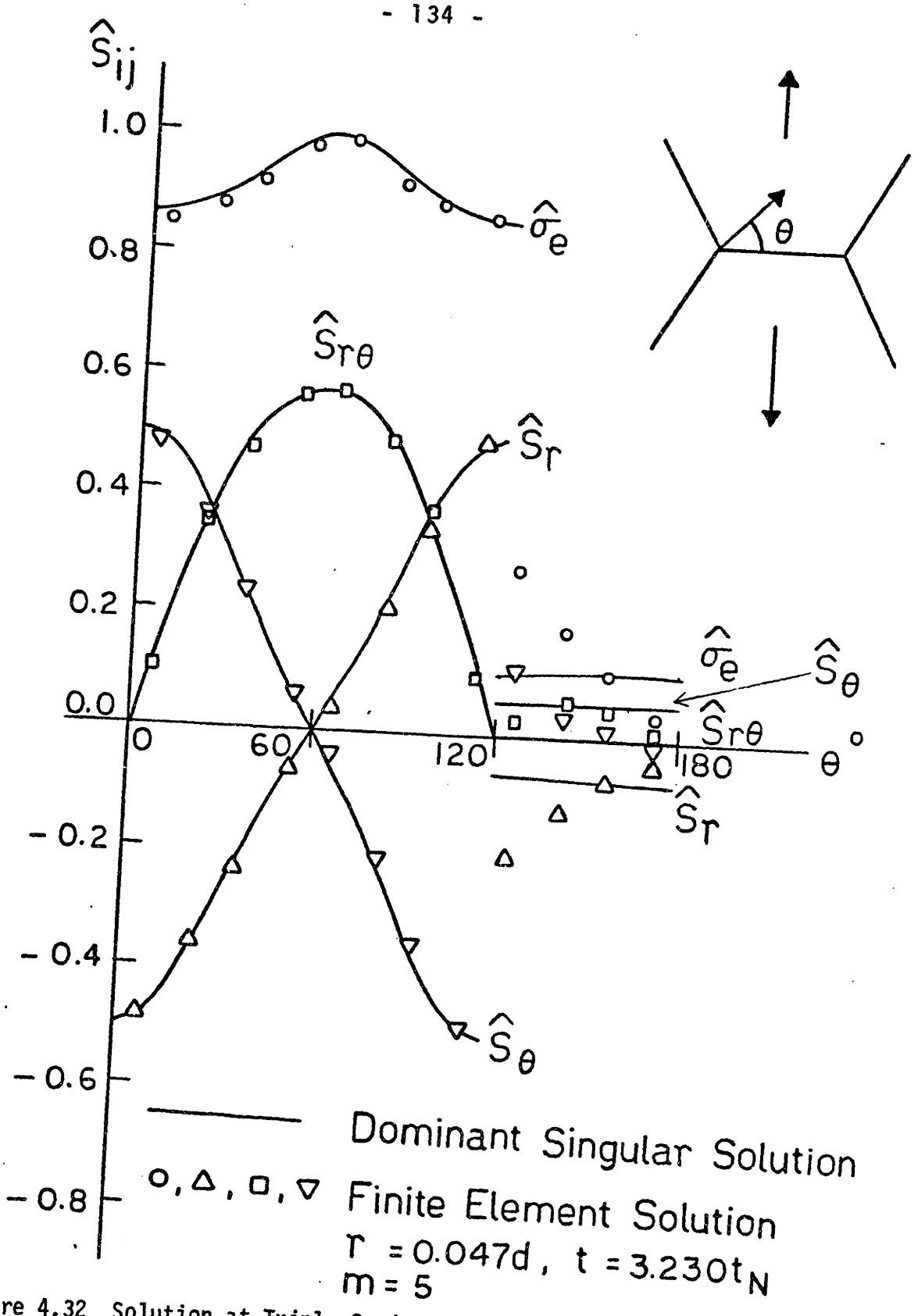

Figure 4.32 Solution at Triple Grain Junction, m = 5, r = 0.047d, $t = 3.230t_N$.

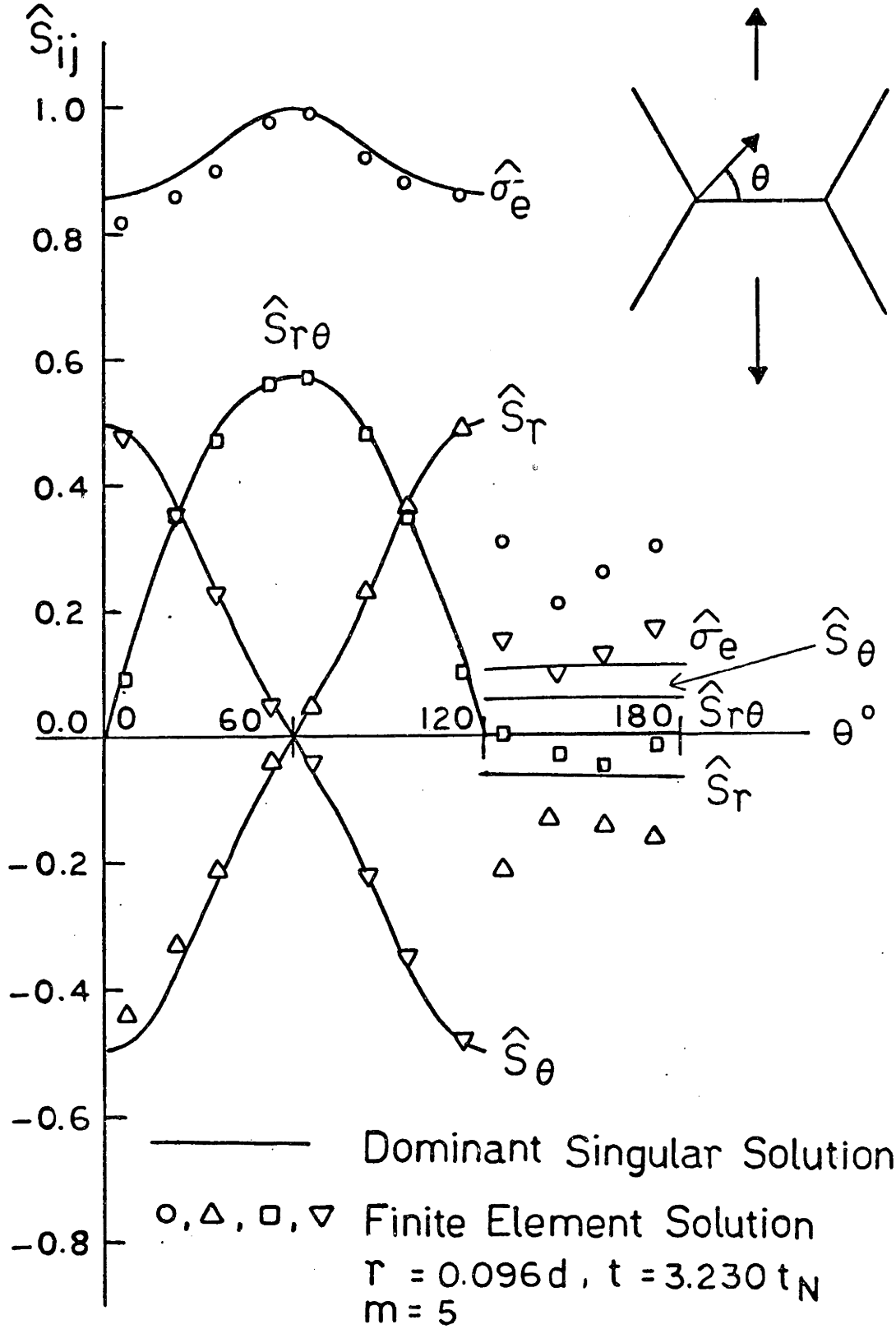

Figure 4.33 FEM Solution at Triple Grain Junction, m = 5, r = 0.096d, t = 3.230t_N.

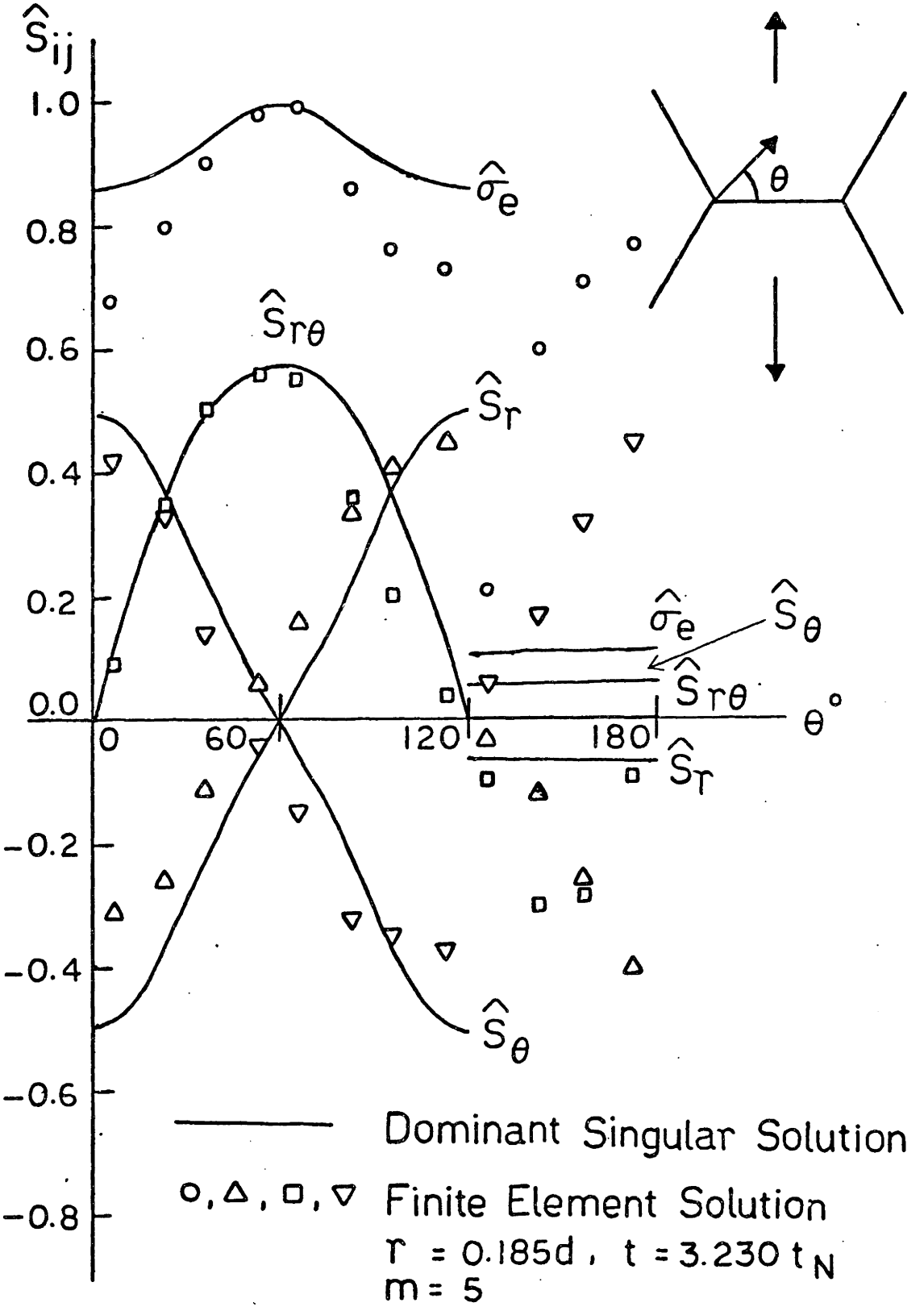

Figure 4.34 FEM Solution at Triple Grain Junction, m = 5, r = 0.185d, t = 3.230t_N.

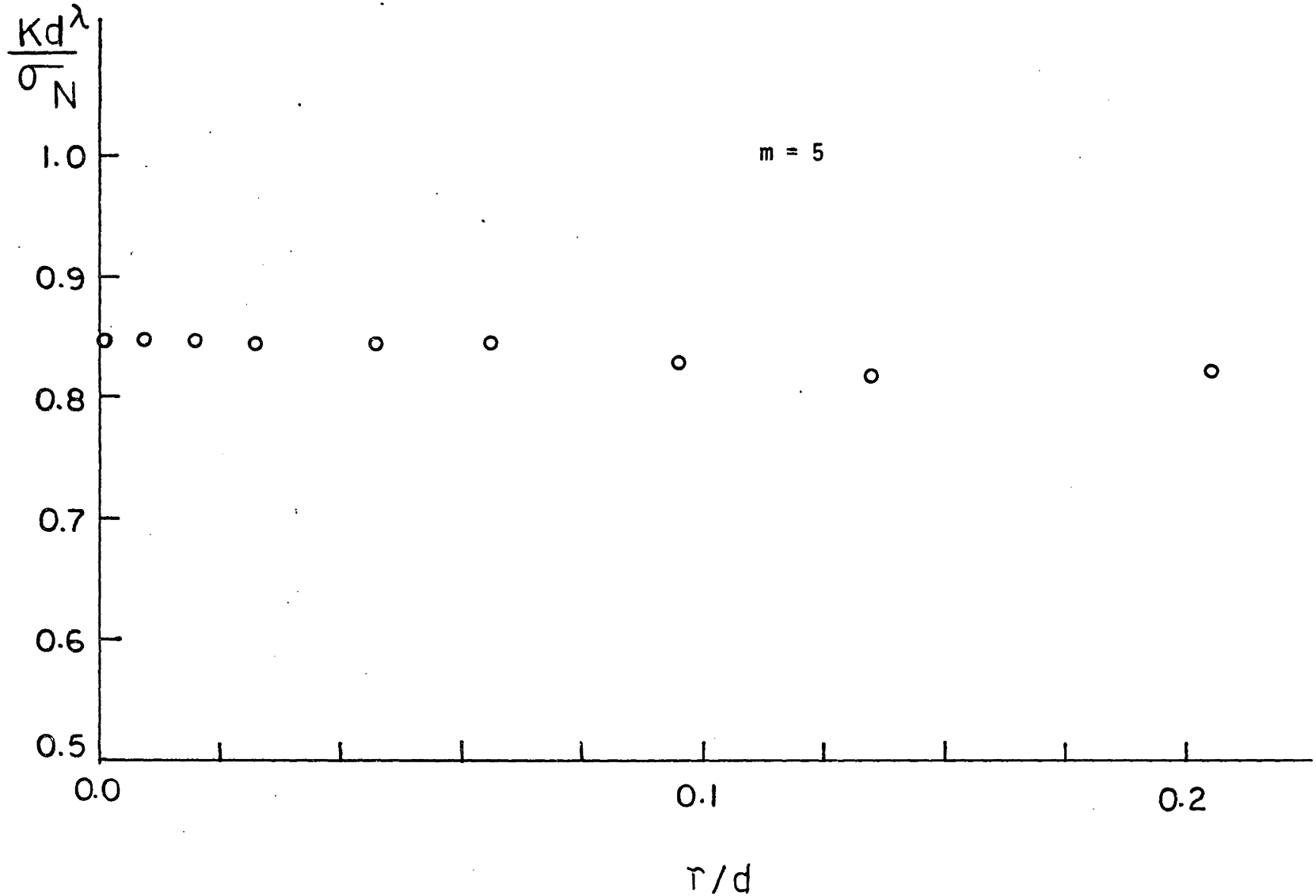

Figure 4.35 Variation of $(Kd^{\lambda})/\sigma_N$ with r/d at $t = 3.230t_N$, m = 5.

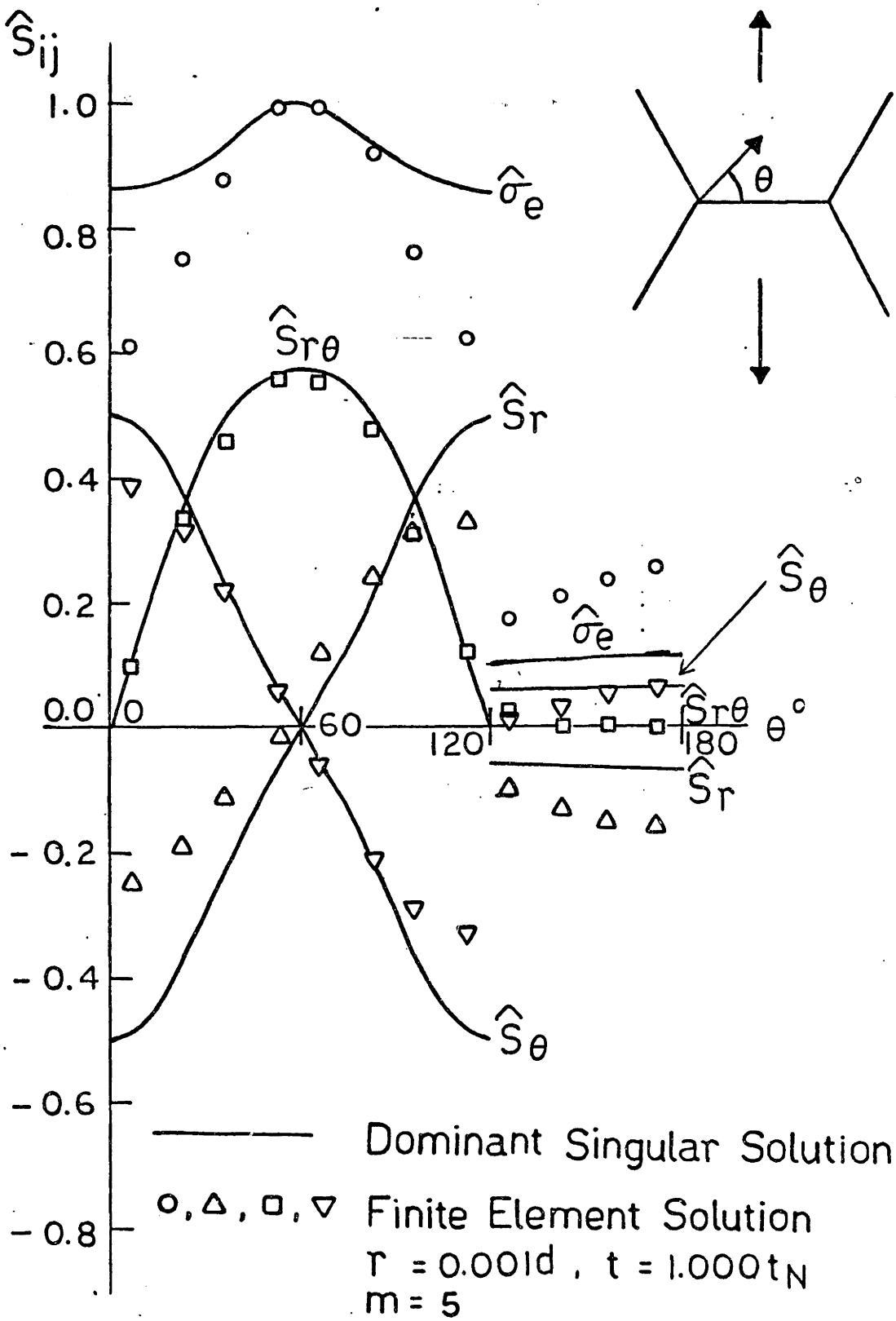

Figure 4.36 FEM Solution at Triple Grain Junction, m = 5, r = 0.001d, t = 1.000t_N.

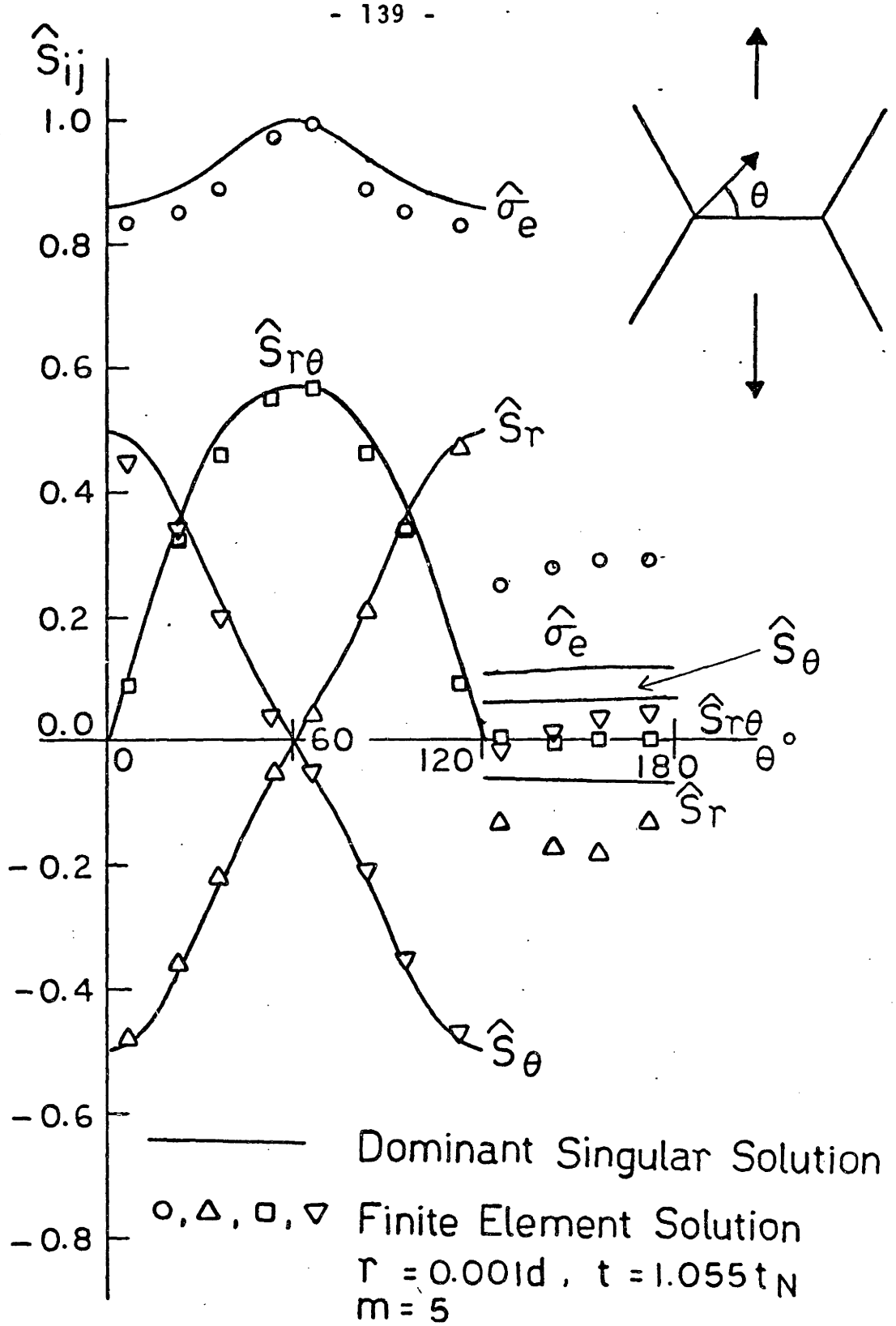

Figure 4.37 FEM Solution at Triple Grain Junction, m = 5, r = 0.001d, t = 1.055t_N.

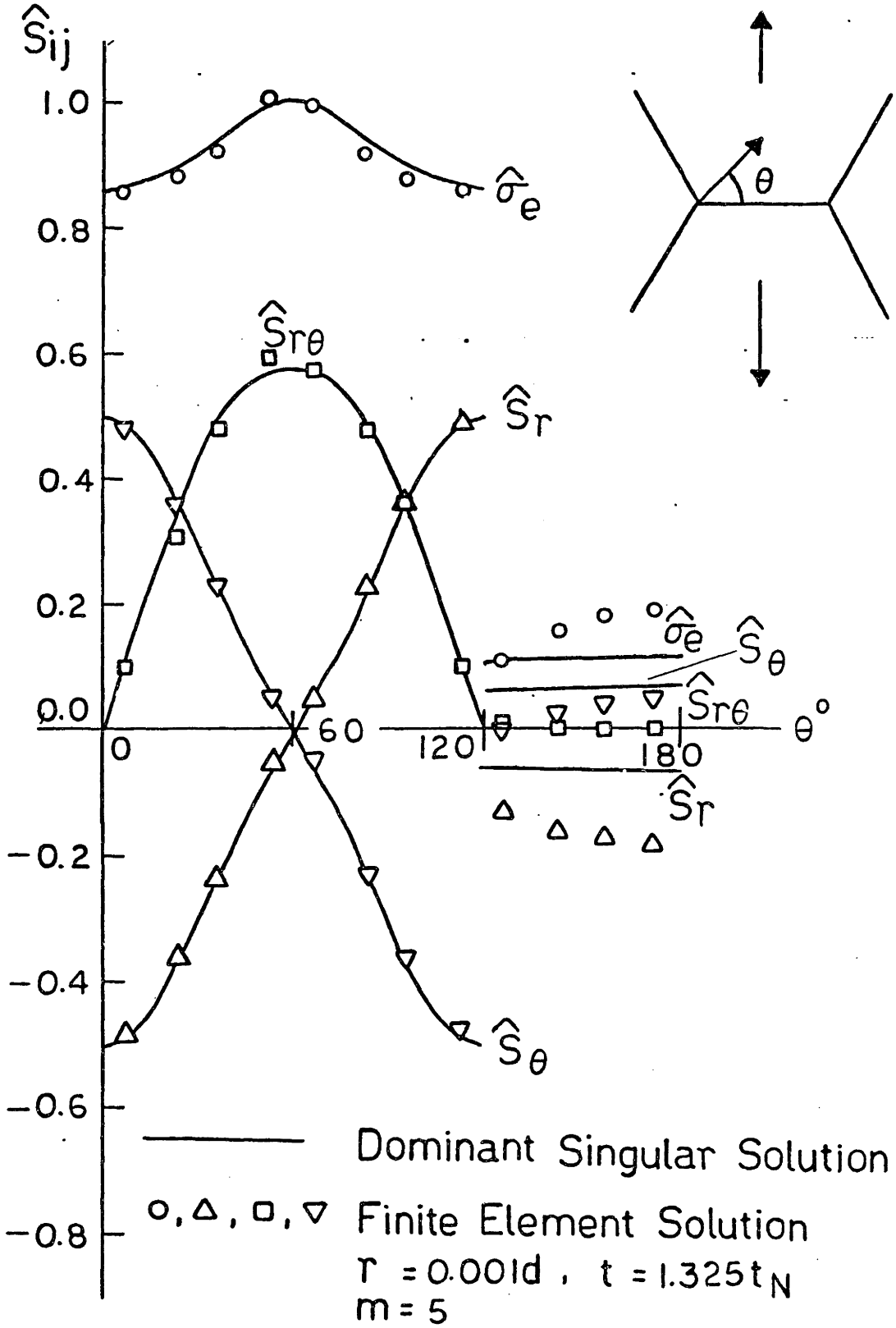

Figure 4.38 FEM Solution at Triple Grain Junction, m = 5, r = 0.001d, t = 1.325t_N.

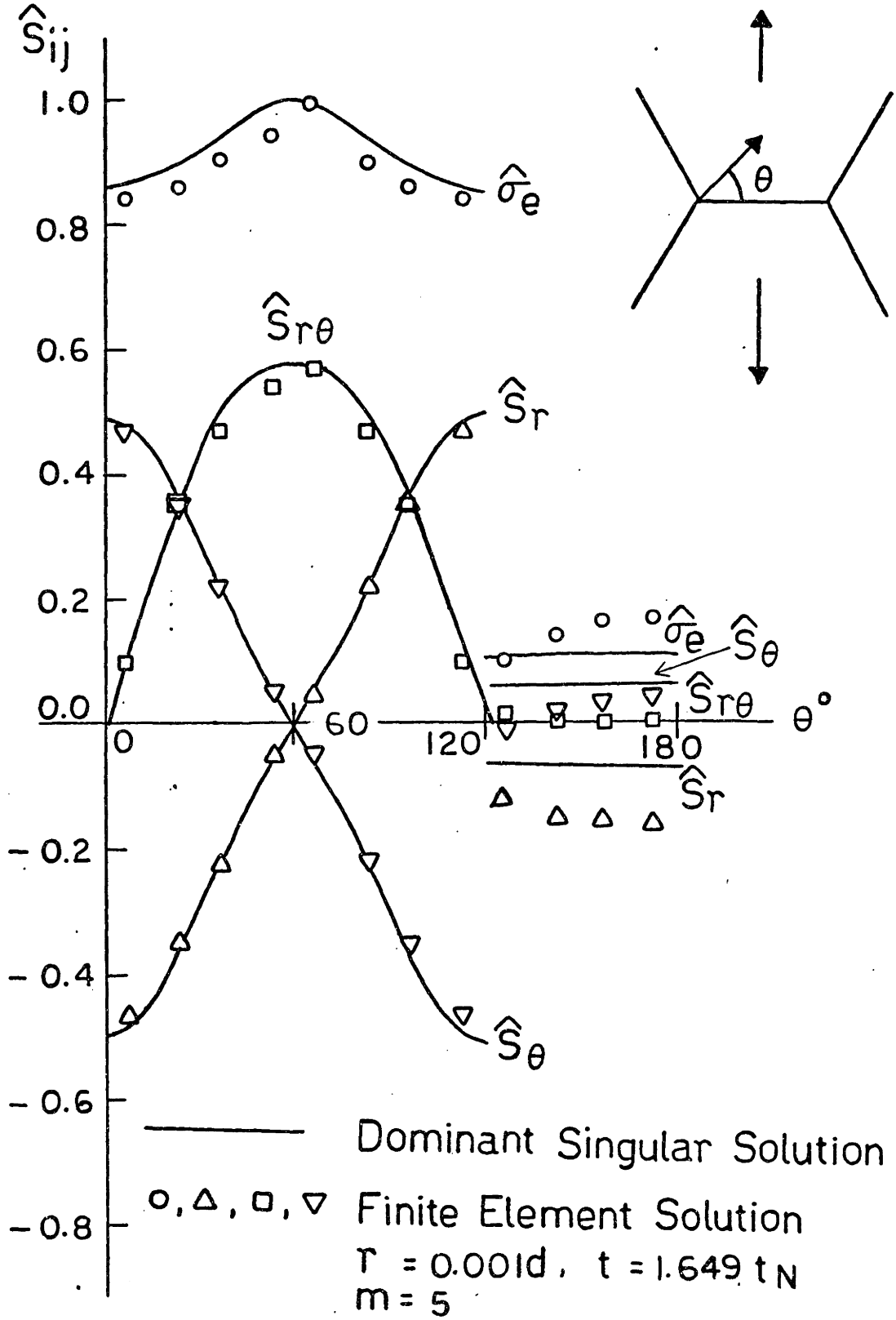

Figure 4.39 FEM Solution at Triple Grain Junction, m = 5, r = 0.001d, t = 1.649t_N.

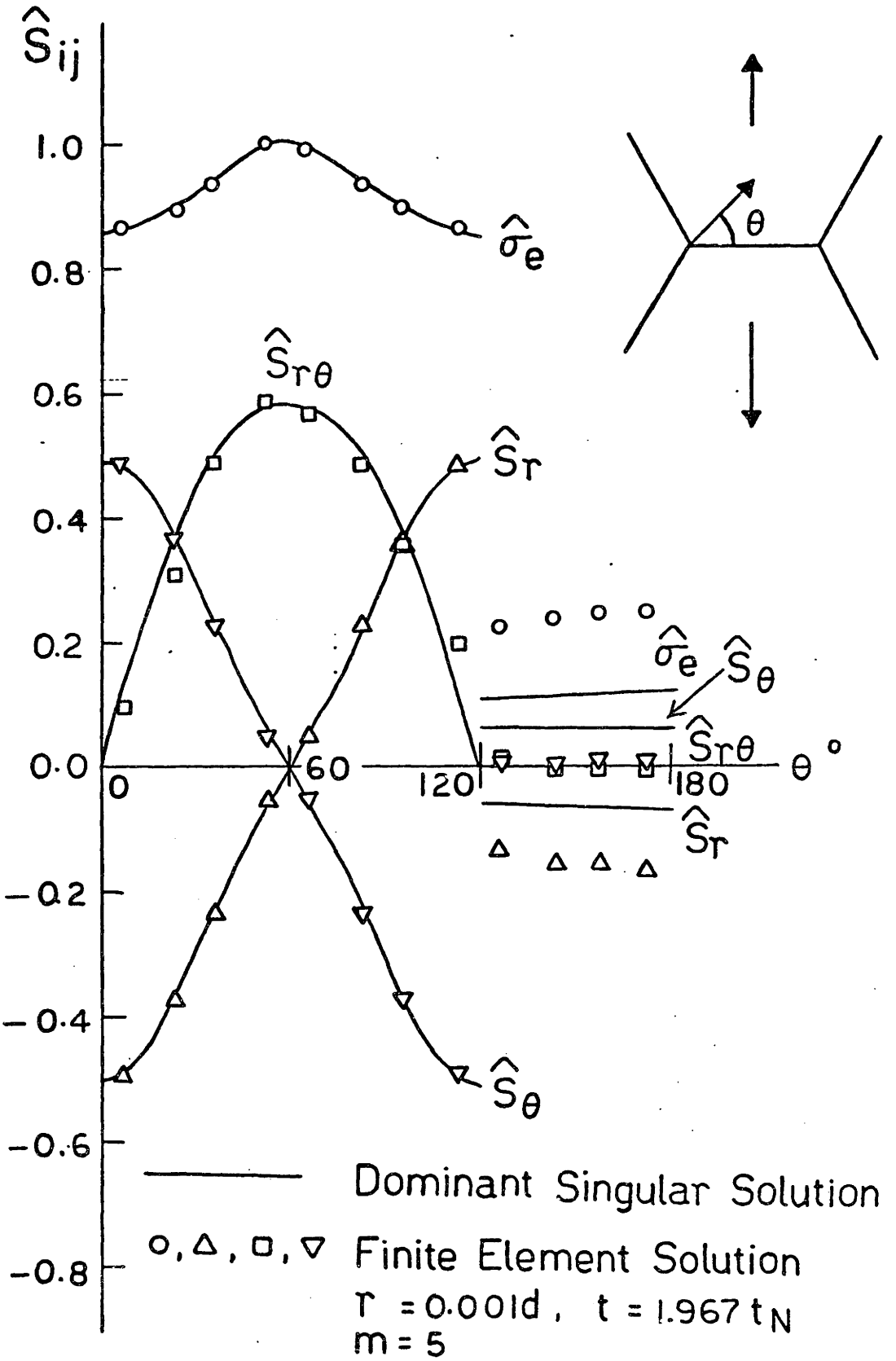

Figure 4.40 FEM Solution at Triple Grain Junction, m = 5, r = 0.001d, t = 1.967t_N.

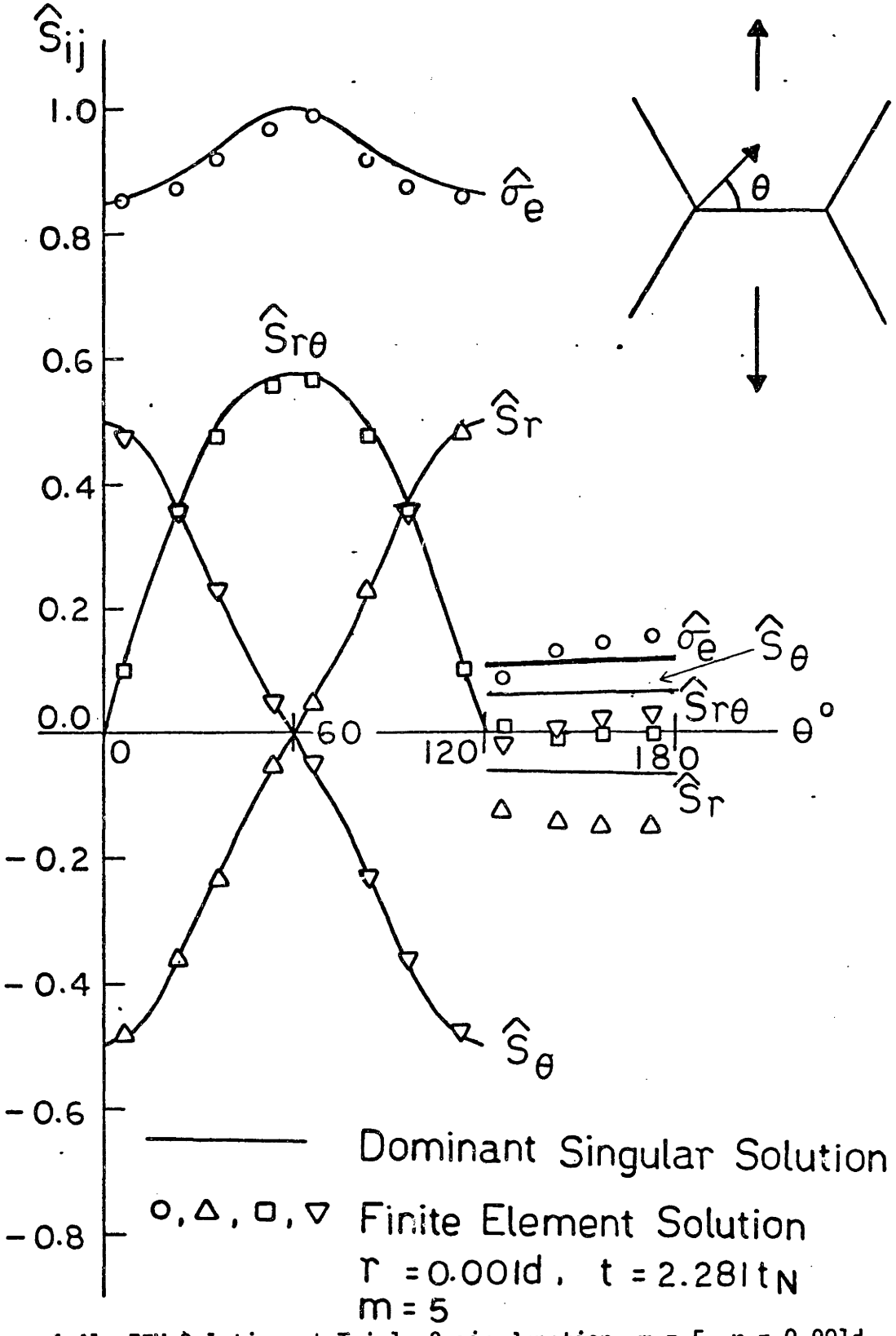

Figure 4.41 FEM Solution at Triple Grain Junction, m = 5, r = 0.001d, t = 2.281t_N.

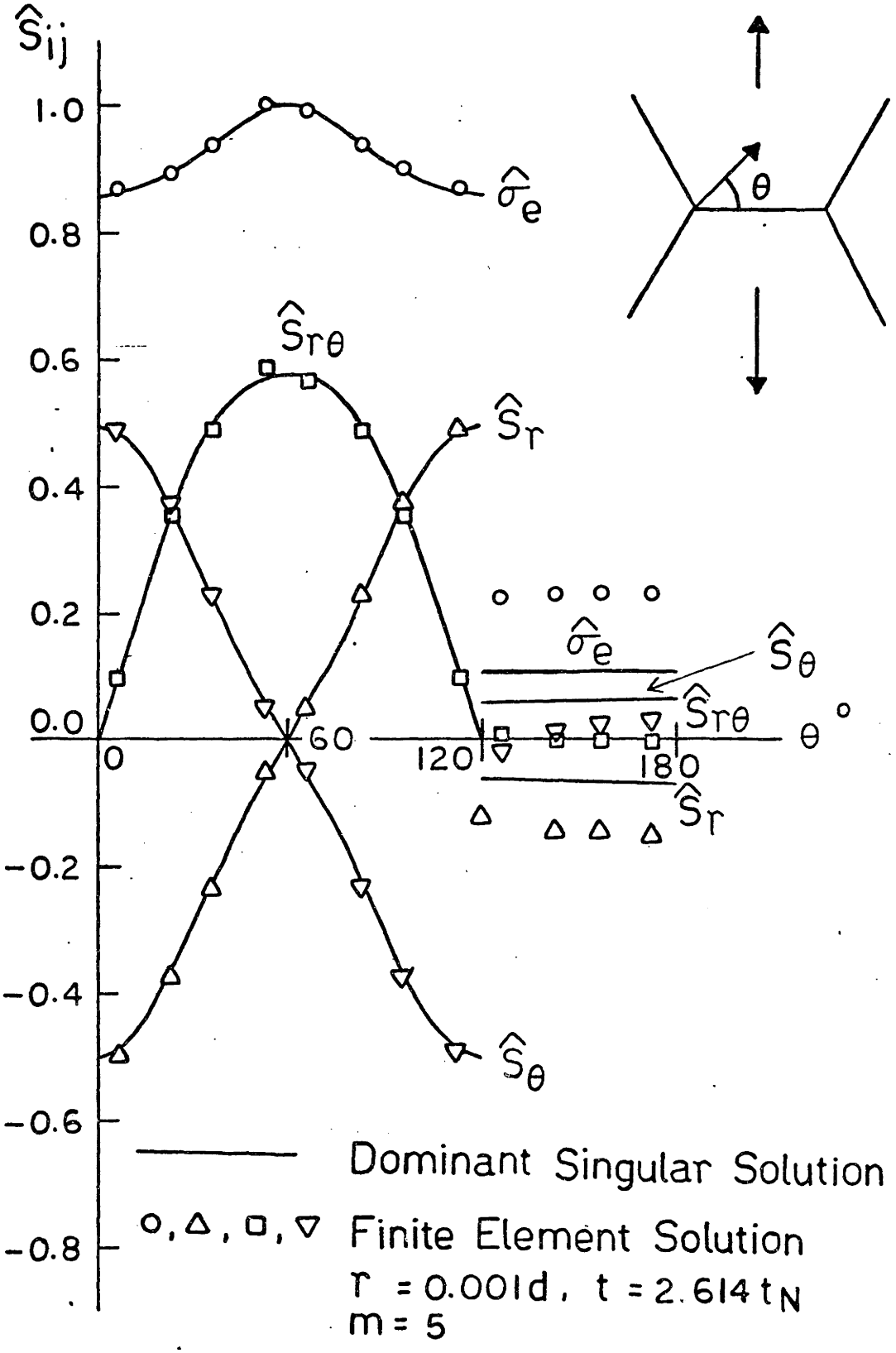

Figure 4.42 FEM Solution at Triple Grain Junction, m = 5, r = 0.001d, t = 2.614t_N.

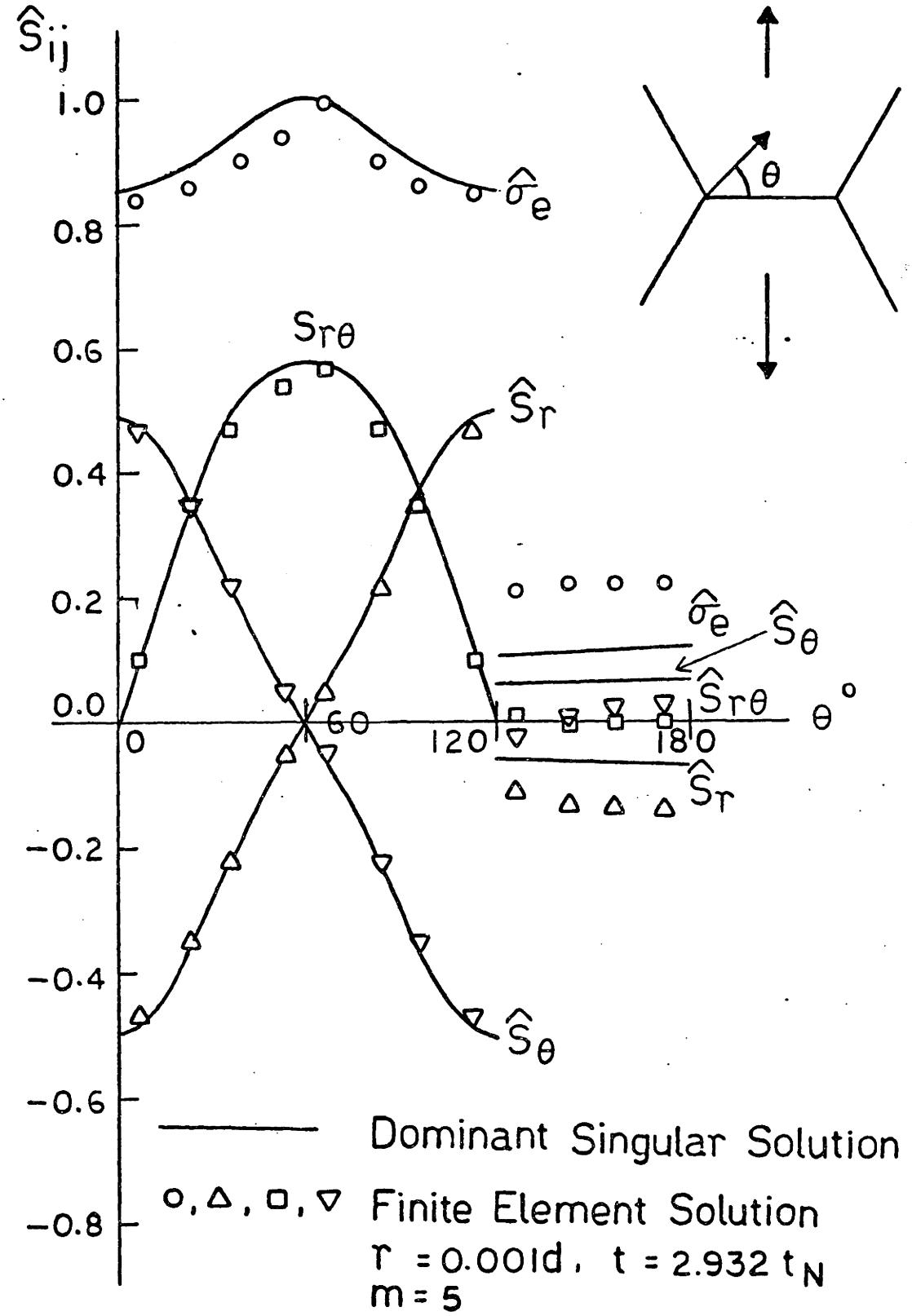

Figure 4.43 FEM Solution at Triple Grain Junction, m = 5, r = 0.001d, $t = 2.932t_N$.

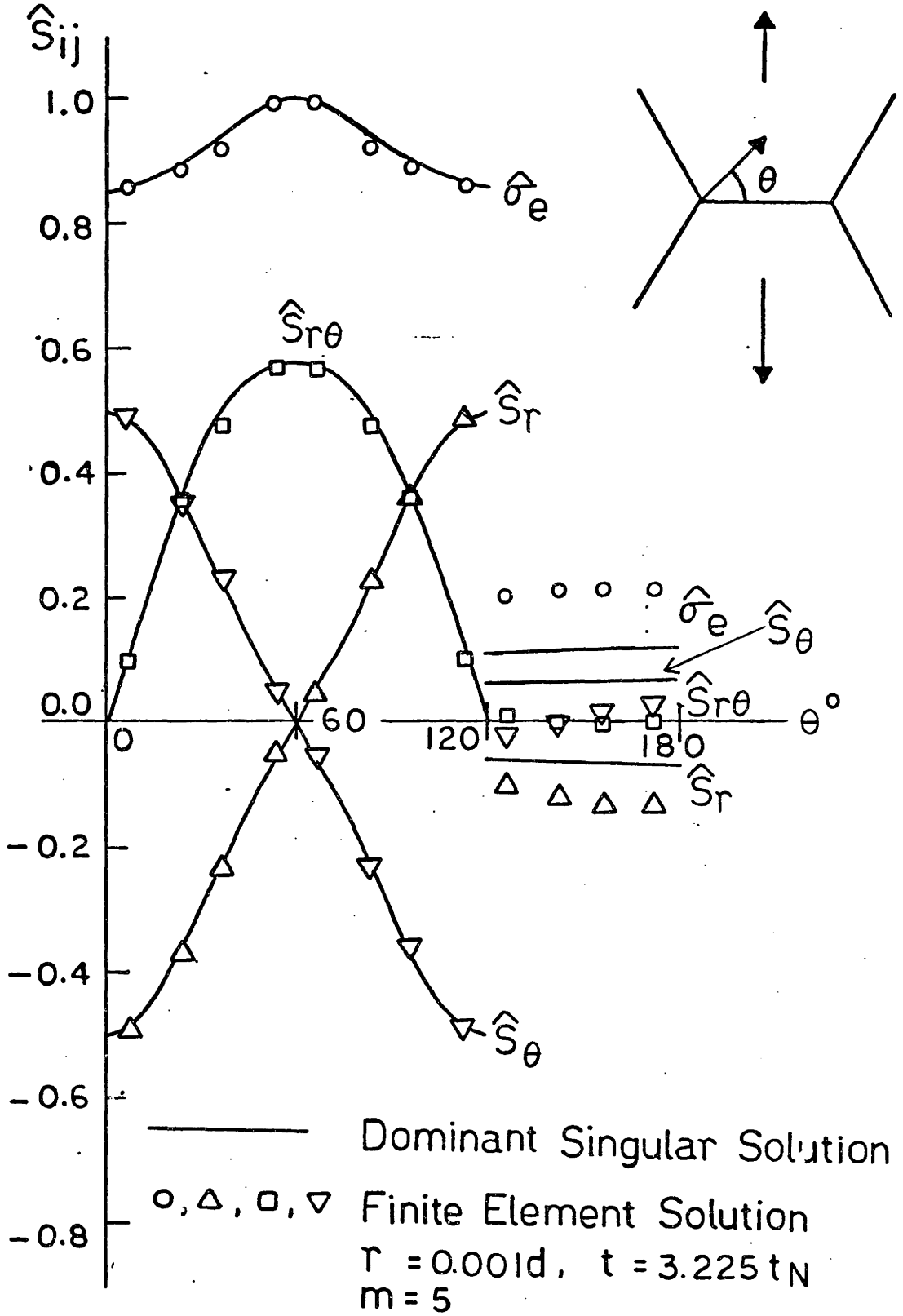

Figure 4.44 FEM Solution at Triple Grain Junction, m = 5, r = 0.001d, $t = 3.225t_N$.

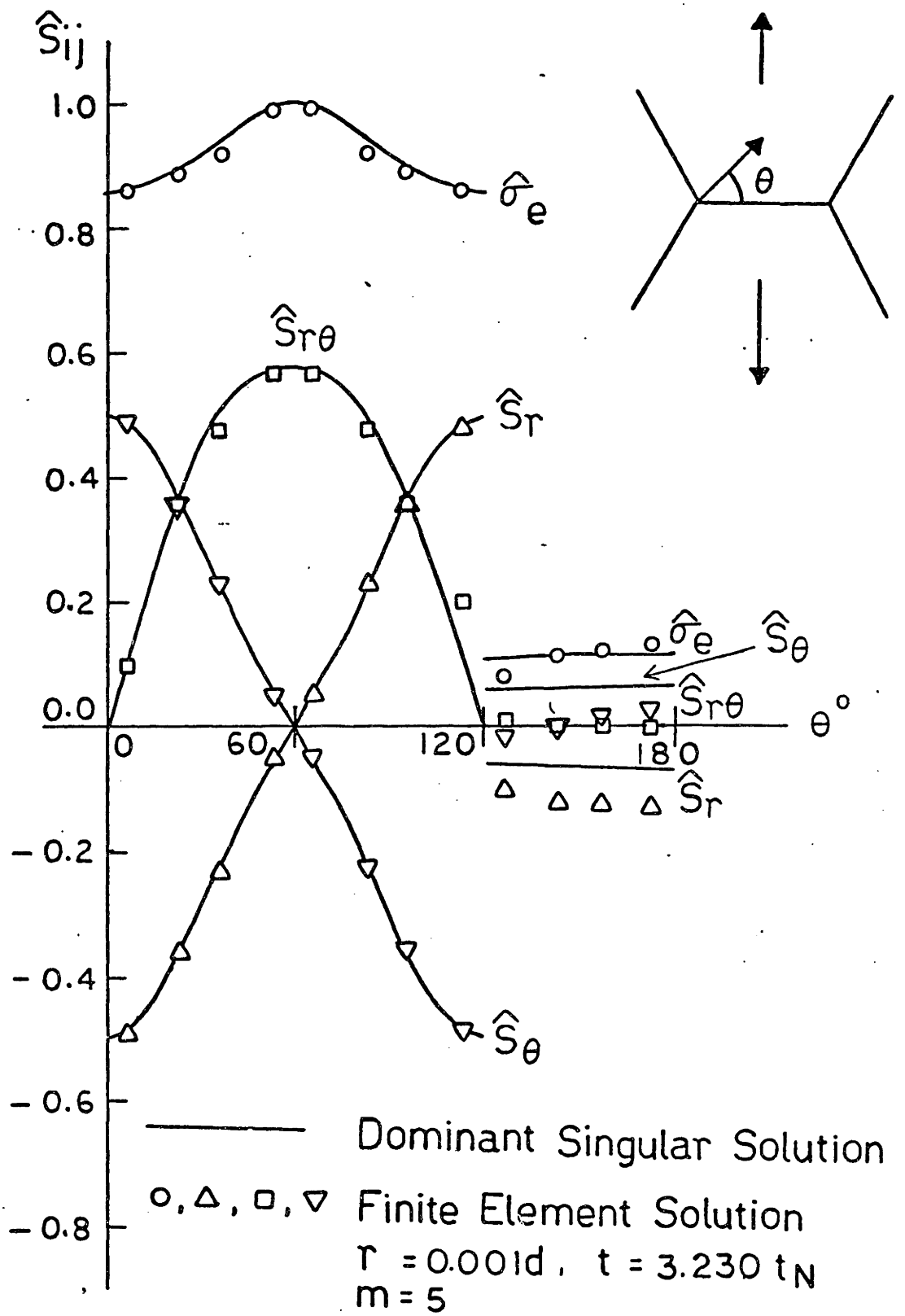

Figure 4.45 FEM Solution at Triple Grain Junction, m = 5, r = 0.001d, $t = 3.230t_N$.

Figure 4.46 shows the value of Kd^{λ}/σ_N determined from the data of Figs. 4.37 to 4.45. There is a mild, but stable fluctuation of Kd^{λ}/σ_N with t/t_N indicating that using smaller f values (Eq. 4.6) than the ones used (5,5,2,2,2,repeat) may give even better results.

Similar to the hard particle problem, an estimation of K can be obtained from overall equilibrium consideration by equating the integral of the singular stress distribution over a characteristic repeat distance to that of the far field tensile traction, giving

$$\frac{Kd^{\lambda}}{\sigma_N}\frac{2}{3} = \frac{(1+\lambda)(2\sqrt{3})^{\lambda}}{\hat{\sigma}_{\theta\theta}(0)} = I(m) \qquad (4.14)$$

Again, the singular stress distribution is not the only contribution to the stresses that balance the far field traction; hence, Eq. 4.14 is subject to a correction. We assume

$$\frac{Kd^{\lambda}}{\sigma_N}\cdot\frac{2}{3} = C(m)\cdot I(m) \qquad (4.15)$$

where C(m) is determined empirically. From Kd^{λ}/σ_N values for m=3 and 5, C(m) is found to be

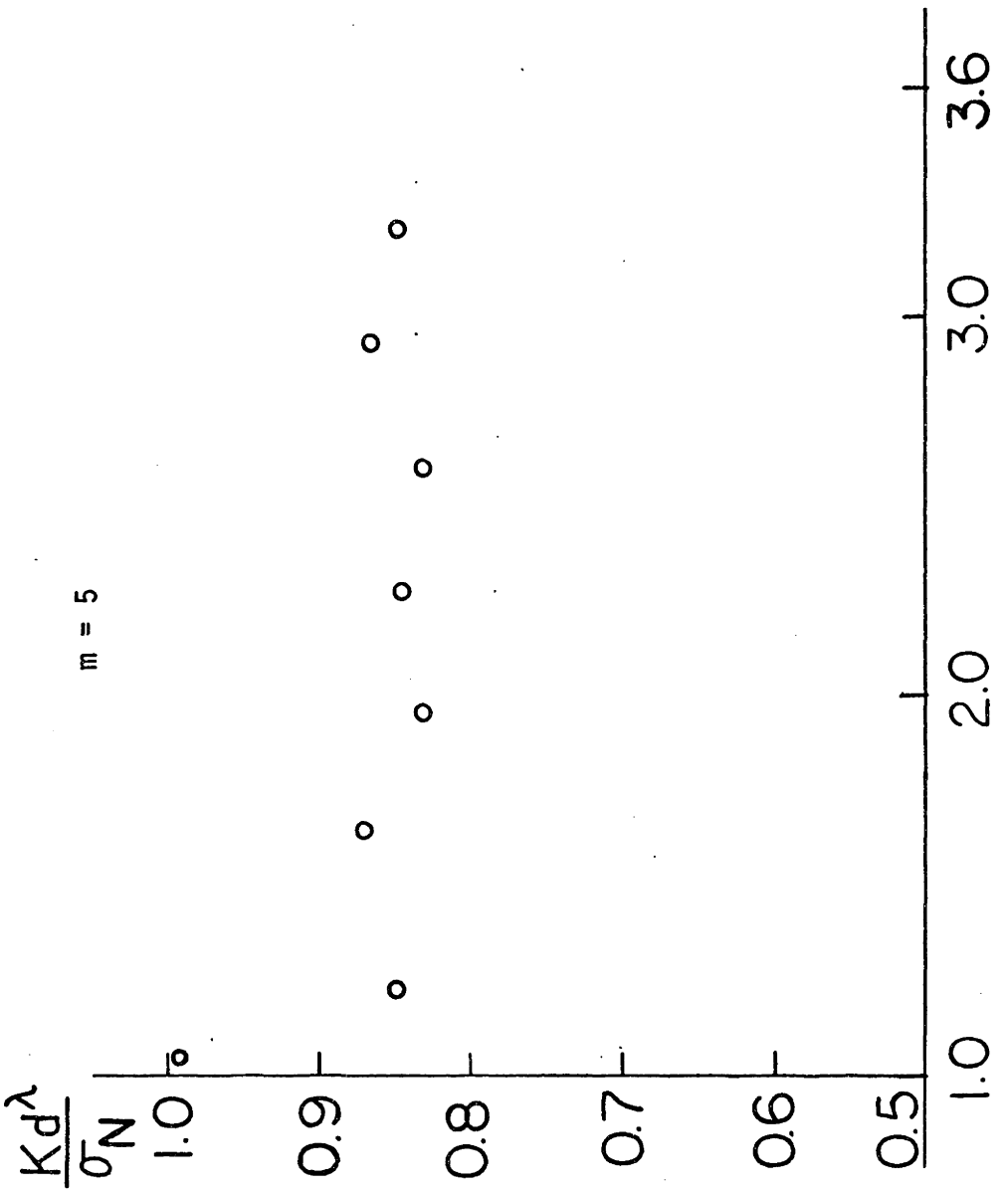

Figure 4.46 Variation of $(Kd^{\lambda})/\sigma_N$ with t/t_N, m = 5, r/d = 0.001.

$$C(m) = 0.613 - 0.010\,(m-3) \qquad (4.16)$$

Values of I(m) and $(Kd^{\lambda}/\sigma_N)\cdot(2/3)$ for m = 1 to 10 are shown in Fig. 4.47. Actual values of I(m), c(m) and $(Kd^{\lambda}/\sigma_N)\cdot(2/3)$ for m = 1 to 10 are listed in Table 4.2.

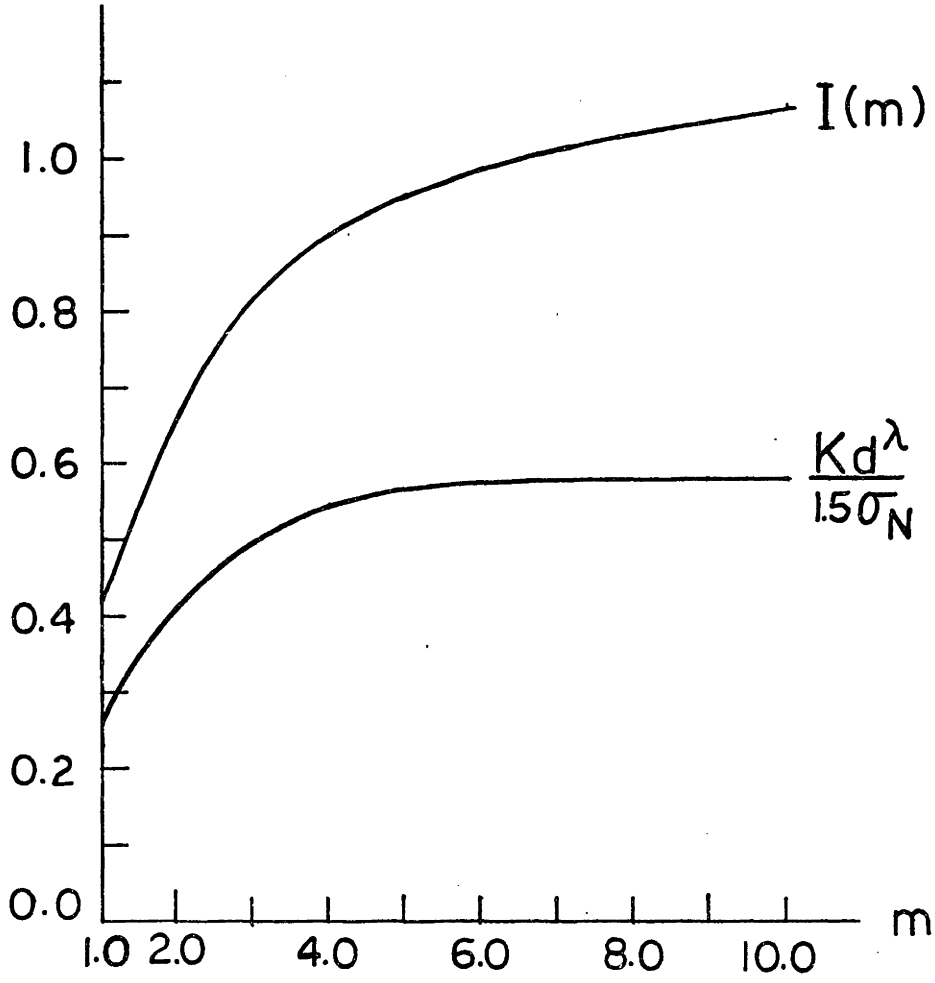

Figure 4.47 Variation of I(m) and $(Kd^{\lambda})/(1.5\sigma_N)$ with m at Triple Grain Junction.

TABLE 4.2

I(m), C(m) and $\frac{Kd^{\lambda}}{1.5\sigma_N}$ FOR THE TRIPLE GRAIN JUNCTION

m	$I(m) = \frac{(1+\lambda)(2\sqrt{3})^{\lambda}}{\hat{\sigma}_{\theta\theta}(0)}$	C(m)	$\frac{Kd^{\lambda}}{1.5\sigma_N}$
1	0.425	0.633	0.269
2	0.654	0.623	0.407
3	0.819	0.613	0.502
4	0.903	0.603	0.545
5	0.953	0.593	0.565
6	0.987	0.583	0.575
7	1.01	0.573	0.579
8	1.03	0.563	0.580
9	1.05	0.553	0.581
10	1.07	0.543	0.581

4.5 Summary

Using a specially developed finite element procedure which uses: (a) novel kinematic modelling of unconventional boundary conditions; (b) specially formulated power-type singular elements; (c) self-adapting explicit time marching; and (d) a matching technique for the angular variation of the deviatoric stresses, we have determined the creep stress intensity factors, K, at both the apexes of grain boundary hard particles and at the triple grain junctions. The values of K are obtained using this finite element procedure for creep exponents, m, of 3 and 5. These results are used, together with a condition of overall equilibrium based on the dominant singular stress distributions of Chapter 3, to develop formulae to estimate the creep stress intensity factors for other values of m. Results for m from 1 to 10 are presented.

CHAPTER FIVE

CONCLUDING REMARKS

The dominant singular stress distributions in power-law creep at both the apexes of grain boundary hard particles and the triple grain junctions, as are solved in Chapter 3 by extending Hutchinson's (1968) approach, show that the strain rates (and hence strains) are more localized and the stresses are more diffused than their corresponding counterparts in linear creep, as are solved in Chapter 1 by William's (1952, 1957) method. The angular variations of the stresses agree with and explain some important experimental observations in the creep fracture of engineering alloys.

The generalized creep stress intensity factors for m=3 and 5 -- as determined by our specially developed finite element procedure which incorporates specially formulated power-type singularity elements, kinematic modelling of unconventional boundary conditions, matching of angular variation of deviatoric stresses to bypass the effect of incompressibility, and self-adaptive explicit time integration with variable weights -- enables formulae to be generated to estimate the generalized creep stress intensity factors for other values of m without any further finite element computation.

The numerical and computational techniques developed in this thesis are readily applicable to other researches of nonlinear fracture mechanics. Researches currently in progress utilizing these techniques include the study of stress redistribution at the tip of a stationary creep crack under reversal of loading, and the micromechanical modelling of the propagation of a creep crack under monotonic loading. The special power-type singular element has also been used to analyze the stress distribution of cracks in bimaterial, the results of which will be reported in a separate communication.

The results of Chapter 3 are based on the deformation theory, but the finite element results of Chapter 4 are based on the flow theory. The fact that these two sets of results agree with each other serves as a numerical confirmation to Ilyushin's (1946) theory.

The detailed quantitative description of the dominant singular stresses at the apexes of grain boundary hard particles and at triple grain junctions enables one to estimate the rate of cavity nucleation in a creeping alloy with the theory developed by Argon, Chen and Lau (1980, 1981).

REFERENCES

ABEL, J. and SHEPHARD, M.S.	1979	Int. J. Num. Meth. Engrg., 14, 464.
ARGON, A.S., CHEN, I.W. and LAU, C. W.	1981	Three Dimensional Constitutive Equations and Ductile Fracture, edited by S. Nemat-Nasser and J. Zarka, North Holland Publishers, Amsterdam, p.21.
ARGON, A.S., CHEN, I.W. and LAU, C.W.	1980	Creep Fatigue and Environment Interactions, edited by R.M.N. Pelloux and N. Stoloff, AIME, Warrendale, Pa., p. 46.
ARGON, A.S. and IM, J.	1975	Met. Trans, 6A, 839.
ASHBY, M.F.	1972	Acta Met., 20, 887.
BARSOUM, R.S.	1977	Int. J. Num. Meth. Engrg., 11, 85.
BASSANI, J. L. and MC CLINTOCK, F.A.	1981	Int. J. Solids Structures, 17, 479.
BATHE, K. J.	1976	ADINA -- A Finite Element Program for Automatic Dynamic Incremental Nonlinear Analysis, Report 82448-1, Acoustics and Vibration Lab., Mech. Eng. Dept., M.I.T.
BATHE, K. J.	1981	Finite Element Procedures in Engineering Analysis, Prentice-Hall, Englewood Cliffs, New Jersey.
BATHE, K. J. and WILSON, E. L.	1976	Numerical Methods in Finite Element Analysis, Prentice-Hall, Englewood Cliffs, New Jersey.

REFERENCES (CONTINUED)

BATHE, K. J.	1981	Private Communication, research in progress at M.I.T., 1981.
BENZLEY, S.E. and PARKS, D. M.	1974	Structural Mechanics Computer Programs, edited by W. Pilkey et. al., University Press of Virginia, Charlottesville, Virginia, p. 81.
BERCOVIER, M. and ENGELMAN, M.	1979	J. Comp. Phys., 30, 181.
BIRD, J.E., MUKHORJEE, A.K. and DORN, J. E.	1969	Quantitative Relation Between Properties and Microstructure, edited by D. G. Brandon and A. Rosen. Israel University Press, Jerusalem, p. 255.
BRUNNER, B. and GRANT, N. J.	1956	Inst. Met., 85, 77.
BUDIANSKY, B.	1959	Trans. Am. Soc. Mech. Engrs, 81E, 250.
CHAN, S.K. TUBA, I.S. and WILSON, W. K.	1970	Engrg. Fracture Mech. 2, 1.
CHEN, I.W. and ARGON, A.S.	1979	Acta Met., 27, 749.
CHEN, I.W. and ARGON, A.S.	1979	Acta Met., 27, 785
CHEN, I.W. and ARGON, A.S.	1981	Acta Met., 29, 1321.
COBLE, R.L.	1963	J. Appl. Phys., 34, 1679.
COKER, E.G. and FILON, L.G.N.	1931	A Treatise on Photoelasticity, Cambridge University Press, Cambridge.

REFERENCES (CONTINUED)

CORMEAU, I.C.	1975	Int. J. Num. Meth. Engrg., 9, 109.
CROSSMAN, F.W. and ASHBY, M.F.	1975	Acta Met., 23, 425.
CURISKIS, J.I. and VALLIAPPAN, S.	1978	Computers and Structures, 8, 117.
FRIED, I.	1973	Int. J. Solids Structures, 9, 323.
GALLAGHER, R.H.	1972	Proceeding First International Conference on Structural Mechanics in Reactor Technology, Berlin, Vol. 6, Part L, p. 637.
GALLAGHER, R. H.	1978	Numerical Methods in Fracture Mechanics, edited by A.R. Luxmore and D.R.J. Owens, University College of Swansea, United Kingdom, p. 1.
GAROFALO, F.	1965	Fundamentals of Creep and Creep-Rupture in Metals, MacMillan, New York.
GEAR, C.W.	1971	Numerical Initial Value Problems in Ordinary Differential Equations, Prentice-Hall, Englewood Cliff, New Jersey.
GHAHREMANI, F.	1980	Int. J. Solids Structures, 16, 847.
GITTUS, J.H.	1974	Acta Met., 22, 789.
GRANT, N.J. and CHANDHRI, A.R.	1965	Deformation and Fracture at Elevated Temperatures edited by N.J. Grant and A.W. Mullendore, M.I.T. Press, Cambridge, MA p105.

REFERENCES (CONTINUED)

GRANT, N.J.	1971	Fracture, Vol. 3, edited by H. Liebowitz, Academic Press, New York, p. 484.
GREENBAUM, G. and RUBIUSTEIN, M.	1968	Nuc. Eng. Design, 7, 379.
HEALD, P.T. and WILLIAMS, J.A.	1970	Phil. Mag. 22, 1095.
HENSHAW, R.D. and SHAW, K.G.	1975	Int. J. Num. Meth. Engrg. 9, 495.
HERRING, C.	1950	J. Appl. Phys. 21, 437.
HERRMANN, L.R.	1965	AIAA J., 3, 1896.
HILDEBRAND, F.B.	1974	Introduction to Numerical Analysis, McGraw-Hill, New York.
HILTON, P. and HUTCHINSON, J.W.	1971	J. Engrg. Fracture Mech., 3, 435.
HOFF, N.J.	1954	Quart. Appl. Meths., 12, 49.
HUGHES, T.J.R.	1980	Int. J. Num. Meth. Engrg., 15, 1413.
HUGHES, T.J.R., LIU, W.K. and BROOKS, A.	1979	J. Comp. Phys., 30, 1.
HUTCHINSON, J.W.	1968	J. Mech. Phys. Solids, 16, 13.
ILYUSHIN, A.A.	1946	Priklandnaia Matematikai Mekhanika, 10, 347.
IRONS, B. and TREHARNE, G.	1971	Third Conf. Matrix Meth. Struct. Mech., Wright-Patterson, A.F.B., Ohio, p. 245.
JONES, R.B.	1966	J. Nucl. Mater. 19, 204.

REFERENCES (CONTINUED)

KELLER, H.B.	1968	Numerical Methods for Two-Point Boundary Value Problems, Blaidel Publishing Company, Waltham, MA.
KNOTT, J.F.	1973	Fundamentals of Fracture Mechanics, Halsted Press, New York.
KOBAYASHI, A., MAIDEN, D., SIMON, B. and IIDA, S.	1969	Paper 69, WA-PVP-12, ASME Winter Annual Meeting.
LAU, C.W. and ARGON, A.S.	1977	Fracture, 1977, Vol. 2 Edited by D.M.R. Taplin, University of Waterloo Press, Waterloo, Canada, p. 595.
LAMBERT, J.D.	1973	Computational Methods in Ordinary Differential Equations, Wiley, London.
LEVY, A. and PIFKO, A.B.	1981	Int. J. Num. Meth. Engrg., 17, 747.
MC CLINTOCK, F.A.	1971	Fracture, Vol. 3, edited by H. Liebowitz, Academic Press, New York, p. 47.
MC CLINTOCK, F.A.	1981	"Stress Redistribution in Creep," Research in progress at M.I.T., Private Communication.
MC CLINTOCK, F.A. and ARGON, A.S.	1966	Mechanical Behavior of Materials, Addison-Wesley, Reading, MA.
MORRIS, D.G.	1978	Metal Sci., 12, 19.
NABARRO, F.R.N.	1948	Report Conf. on Strength of Solids, London Physical Society, London, p. 75.

REFERENCES (CONTINUED)

NAGTEGAAL, J.C., PARKS, D.M. and RICE, J.R.	1974	Comp. Meth. Appl. Mech. Engrg., 4, 153.
NAYLOR, D. J.	1974	Int. J. Num. Meth. Engrg., 8, 443.
NEEDLEMAN, A. and SHIH, C.F.	1978	Comp. Meth. Appl. Mech. Engrg., 15, 223.
NORTON, F.H.	1929	The Creep of Steel at High Temperature, McGraw-Hill, New York.
ODEN, J.T.	1968	Aeron. Q., 19, 254.
ODEN, J.T.	1972	Finite Elements of Nonlinear Continua, McGraw-Hill, New York.
ODQVIST, F.K.G.	1974	Mathematical Theory of Creep and Creep Rupture, Oxford University Press, Oxford.
PERRY, A.J.	1974	J. Mat. Sci., 9, 1016.
PIAN, T.H.H.	1975	Proceedings of World Congress on Finite Element Methods in Structural Mechanics, Vol. 1, Bournemouth, England, p.F-1.
PIAN, T.H.H. and LEE, S.W.	1976	AIAA, J., 14, 824.
RALSON, A. and WILF, H.S.	1960	Mathematical Methods for Digital Computers, Wiley, New York.
RAJ, R.	1978	Acta Met., 26, 995.
RICE, J.R. and ROSENGREN, G.F.	1968	J. Mech. Phys. Solids, 16, 1.

REFERENCES (CONTINUED)

ROBERTS, S.M. and SHIPMAN, J.S.	1972	Two Point Boundary Value Problems, Shooting Methods, American Elsevier, New York.
SHERBY, O.D. and BURKE, P.M.	1967	Progress in Materials Science, Vol. 13, Pergamon Press, Oxford, p. 325.
SHIH, C.F.	1974	Fracture Analysis, ASTM, STP 560, American Society for Testing and Materials, Phil, pp. 187-219.
SHIH, C.F.	1973	"Elastic-Plastic Analysis of Combined Mode Crack Problems", PhD Thesis, Harvard University.
SMITH, E. and BARNBY, J.T.	1967	Met. Sci. 1, 1.
SNYDER, M.D.	1980	Ph.D. Thesis, Mechanical Engineering, M.I.T., Cambridge, MA.
SRITHERAN, T. and JONES, H.	1980	Acta Met., 28, 1633.
SWEDLOW, J.L.	1978a	Fracture Mechanics, edited by N. Perrone, H. Liebowitz, D. Mulville, and W. Pilkey, University Press of Virginia, Charlottesville, p. 529.
SWEDLOW, J.L.	1978b	Int. J. Num. Meth. Engrg., 12, 1979.
TAKENCHI, S. and ARGON, A.S.	1972	J. Met. Sci., 11, 1542.
TAKENCHI, S and ARGON, A.S.	1976	Acta Met., 24, 883.

REFERENCES (CONTINUED)

TONG, P.	1969	Int. J. Solids Structures, 5, 455.
TONG, P. and PIAN, T.H.H.	1972	Int. J. Solids Structures, 9, 313.
TONG, P., PIAN, T.H.H. and LASRY, S.	1973	Int. J. Num. Meth. Engrg., 7, 297.
TRACEY, D.M. and COOK, T.	1977	Int. J. Num. Meth. Engrg., 11, 1225.
TSACH, U.	1981	Int. J. Num. Meth. Engrg., 17, 633.
WILLIAMS, M.L.	1952	J. Appl. Mech., 19, 526.
WILLIAMS, M.L.	1957	J. Appl. Mech., 24, 109.
WILLIAMS, M.L.	1961	J. Appl. Mech., 78.
ZIENKIEWICZ, O.C.	1977	The Finite Element Method, McGraw-Hill, London.
ZIENKIEWICZ, O.C. and CORMEAU, I.C.	1974	Int. J. Num. Meth. Engrg., 8, 821.

APPENDIX A

GOVERNING EQUATION FOR DOMINANT SINGULARITY ANALYSIS

The detailed form of Eq. (3.7) is:

$$\hat{\phi}^{\cdots\cdot} = \frac{-1}{F^{\frac{m-1}{2}} - F^{\frac{m-3}{2}} \frac{3}{4}(m-1)\left[\hat{\phi}^{\cdot\cdot} - \lambda(\lambda+2)\hat{\phi}\right]^2}$$

$$\times \left\{ \begin{array}{l} F^{\frac{m-5}{2}} (F^{\cdot})^2 \frac{m-1}{2}\cdot\frac{m-3}{2}\left[\hat{\phi}^{\cdot\cdot} - \lambda(\lambda+2)\hat{\phi}\right] \\ + F^{\frac{m-3}{2}}(m-1)\left[\begin{array}{l} \frac{3}{4}\left[\hat{\phi}^{\cdot\cdot} - \lambda(\lambda+2)\hat{\phi}\right] \left\{ \begin{array}{l} (\hat{\phi}^{\cdot\cdot})^2 + (\hat{\phi}^{\cdot})^2\left[4(\lambda+1)^2 - \lambda(\lambda+2)\right] \\ + \hat{\phi}^{\cdot}\hat{\phi}^{\cdot\cdot}\left[4(\lambda+1)^2 - 2\lambda(\lambda+2)\right] \\ + \hat{\phi}\hat{\phi}^{\cdot\cdot}\lambda^2(\lambda+2)^2 \\ + (\hat{\phi}^{\cdot})^2\lambda^2(\lambda+2)^2 \end{array} \right. \\ + F^{\cdot}\left\{\hat{\phi}^{\cdots} + \hat{\phi}^{\cdot}\left[2(\lambda+1)(m\lambda+1) - \lambda(\lambda+2)\right]\right\} \end{array} \right] \\ + F^{\frac{m-1}{2}} \left[\begin{array}{l} \hat{\phi}^{\cdot\cdot}\left\{4(\lambda+1)(m\lambda+1) - \lambda(\lambda+2) - m\lambda(m\lambda+2)\right\} \\ + \hat{\phi}\, m\lambda^2(\lambda+2)(m\lambda+2) \end{array} \right] \end{array} \right\}$$

where

$$F = \frac{3}{4}\left[(\hat{\phi}^{\cdot\cdot})^2 - 2\lambda(\lambda+2)\hat{\phi}\hat{\phi}^{\cdot\cdot} + \lambda^2(\lambda+2)^2\hat{\phi}^2\right] + 3(\lambda+1)^2(\hat{\phi}^{\cdot})^2$$

and

$$F^{\cdot} = \frac{3}{2}\left[\hat{\phi}^{\cdot\cdot}\hat{\phi}^{\cdot\cdot\cdot} + \hat{\phi}^{\cdot}\hat{\phi}^{\cdot\cdot}\left(4(\lambda+1)^2 - \lambda(\lambda+2)\right) - \hat{\phi}\hat{\phi}^{\cdot\cdot\cdot}\lambda(\lambda+2) + \hat{\phi}\hat{\phi}^{\cdot}\lambda^2(\lambda+2)^2\right]$$

APPENDIX B

THE POWER-TYPE SINGULARITY ELEMENT

The aim of this appendix is to develop a two dimensional element that can accurately represent a $r^{(q-1)}$ singularity in strain; has all the usual necessary constant state representations and is compatible with the 8-node isoparametric element. For this purpose, we redeveloped Tracey and Cook's (1977) element which does not fulfill the second and third requirements mentioned above. Our new element has five nodes in the natural space (ξ,η) but two adjacent nodes are collapsed into one node in the physical space (x,y). (See Figs. 4.1b and 4.1a respectively). Hence, with the node numbers as defined in Figs. 4.1a and 4.1b, we will refer to this special element as a four node element. The mapping function that maps an element from the physical (x,y) space into a unit square in the natural space (ξ,η) is

$$\underline{X} = \sum H_i \, \underline{x}_i \tag{A2.1}$$

where $\underline{X}^T = \{x, y\}$

$$\begin{aligned} H_1 &= \xi(1-2\eta)(1-\eta) \\ H_2 &= \xi(-1+2\eta)\eta \\ H_3 &= 1-\xi \\ H_4 &= 4\xi(\eta-\eta^2) \end{aligned} \tag{A2.2}$$

Using a cylindrical coordinate system (r,θ) with its origin at the col-

lapsed node in the physical space (Fig. 4.1a), one can derive from Eqs. A2.1-A2.2, after some simple algebra, that

$$\xi \propto r \tag{A2.3}$$

If we then interpolate the displacements, $\underline{U}^T = \{U,V\}$, in the physical element in such a way that

$$\underline{u} \propto \xi \text{ and } \xi^q \tag{A2.4}$$

then

$$\underline{u} \propto r \text{ and } r^q$$

Hence, the gradient of $\underline{U}$ has a constant term and is proportional to r^{q-1}.

We use the displacement interpolation of

$$\underline{u} = \sum N_i \underline{u}_i \tag{A2.5}$$

where

$$\begin{aligned} N_1 &= \frac{\xi + \alpha \xi^q}{1+\alpha}(1-2\eta)(1-\eta) \\ N_2 &= \frac{\xi + \alpha \xi^q}{1+\alpha}(-1+2\eta)\eta \\ N_3 &= 1 - \frac{\xi + \alpha \xi^q}{1+\alpha} \\ N_4 &= 4\frac{\xi + \alpha \xi^q}{1+\alpha}(\eta - \eta^2) \end{aligned} \tag{A2.6}$$

α is a constant and $q < 1$.

With this interpolation, not only the strains have a $r^{(q-1)}$ singularity as well as the constant strain term, but the displacements at the element side 1-4-2 (Fig 4.1a) are also compatible with displacements of 8-node isoparametric elements.

This special element was coded into a version of the Adina (Bathe 1976) program. For the meshes used in our computations (Figs. 4.5 and 4.27), α was inputed as 99. For other computations where the singular element covers a proportionally larger area of the domain, a lower value should be inputed for α to emphasize the relative increase in importance of the constant strain term compared to the r^{q-1} strain term at finite r.

Studying in detail the functional forms of the stiffness matrix $\underline{K}$ (Eq. 4.4) and the creep force ${}^{\Delta t}\underline{F}^{c}$ (Eq. 4.5) by following step-by-step the usual finite element procedures, (Bathe 1981), one can find that using Eq. A2.6 as interpolation function will necessitate one to integrate terms of special forms: $\xi^{2q-1} f(\eta)$ and $\xi^{q} g(\eta)$; and of regular polynomial form, $\xi h(\eta)$ over ξ and η, where $f(\eta)$, $g(\eta)$ and $h(\eta)$ are polynomials of η. For the results reported in Chapter 4 the regular polynomial term, $\xi h(\eta)$, as well as the η portion, [$f(\eta)$ and $g(\eta)$] of the special terms have been integrated with 2-point Gauss-Legendre quadrature. The special terms of functional forms ξ^{2q-1} and ξ^{q} are integrated by the following one point numerical integration rule at the integration station ξ_i and with a weight of 1,

$$\int_0^1 \xi^t \, d\xi = \xi_i^t \tag{A2.7}$$

where

$$\xi_i = \left[\frac{1}{1+t}\right]^{\frac{1}{t}} \tag{A2.8}$$

This numerical integration is equivalent to exact integration since

$$\int_0^1 \xi^t \, d\xi = \frac{1}{1+t} \tag{A2.9}$$

During part of the investigation, we have studied the effect of using 1-point and 2-point Gauss-Legendre integration to integrate these special functional terms. Our results indicate that using the special one point integration rule (A2.7, A2.8), the computations consistently produce more accurate results of stresses and strain distributions in our bench-mark elastic-power-law creep analyses.